# ENHANCED PHOTOCATALYTIC $NO_x$ OXIDATION-STORAGE OVER TITANIA-METAL OXIDE PHYSICAL MIXTURES UNDER UV AND VISIBLE LIGHT

A THESIS SUBMITTED
THE GRADUATE SCHOOL OF ENGINEERING AND SCIENCE
OF BILKENT UNIVERSITY
IN PARTIAL FULFILLMENT OF THE REQUIREMENTS FOR
THE DEGREE OF
MASTER OF SCIENCE
IN
CHEMISTRY

By
Mustafa Çağlayan
June 2017

ENHANCED PHOTOCATALYTIC $NO_x$ OXIDATION-STORAGE OVER TITANIA-METAL OXIDE PHYSICAL MIXTURES UNDER UV AND VISIBLE LIGHT

By Mustafa Çağlayan

June 2017

We certify that we have read this thesis and that in our opinion it is fully adequate, in scope and in quality, as a thesis for the degree of Master of Science.

Emrah Özensoy (Advisor)

Burak Ülgüt

Deniz Üner

Approved for the Graduate School of Engineering and Science:

Ezhan Karaşan
Director of the Graduate School

# ABSTRACT

## Enhanced Photocatalytic $NO_x$ Oxidation-Storage over Titania-Metal Oxide Physical Mixtures under UV and Visible Light

MUSTAFA ÇAĞLAYAN

M.S. in Chemistry

Advisor: Emrah Özensoy

June 2017

Developing new technologies for the abatement of gaseous nitrogen oxides (NO, $NO_2$, etc.) will still be one of the popular research fields; because fossil fuels (mainly coal and natural gas) will remain as the main energy sources for many decades to come. Although various technologies have been developed and implemented for $DeNO_x$ processes, alternative approaches are still open to discussion. Among these; Photocatalytic $NO_x$ Oxidation-Storage (PhoNOS) can offer promising opportunities to overcome this environmental challenge, as it can be utilized under ambient conditions with the help of UV and visible light irradiation.

In this study; firstly, a new performance analysis method was developed other than the photonic efficiencies used in previous works. In this analysis method, a *"$DeNO_x$ Index"* was utilized. This index indicates the net change in total air pollution due to $NO_x$ species by comparing the relative contributions of NO and $NO_2$ along with NO conversion and solid state $NO_x$ storage selectivity. This new method was first applied on previously studied $TiO_2$-$Al_2O_3$ binary oxide samples (P2) synthesized by sol-gel co-precipitation method in comparison with commercially available Degussa P25 $TiO_2$. Furthermore, $TiO_2$-$Al_2O_3$ (P2) binary oxides were also physically/mechanically mixed with an alkaline earth oxide, CaO. Addition of CaO to P2 binary oxides decreased the NO conversion while enhancing the $NO_x$ storage. In order to alleviate the loss of NO conversion in CaO+P2 systems, physical mixtures of P25 $TiO_2$ with two different commercial metal oxides (CaO and γ-$Al_2O_3$) were prepared and investigated. While CaO provides "higher alkalinity" (*i.e.* a desirable property for the solid state storage of acidic gaseous $NO_x$ species) than γ-$Al_2O_3$, mesoporous γ-$Al_2O_3$ can provide a higher porosity and

specific surface area for the adsorption and storage of the oxidation products in the solid state. Considering these, binary or ternary mixtures with various compositions were prepared and catalytically tested under UV and Visible light irradiation. It was found out that the boosting effect of CaO on $NO_x$ storage is more significant than that of $\gamma$-$Al_2O_3$ for the binary oxides. On the other hand, it should be noted that ternary mixtures containing smaller amounts of titania with high performance can also be obtained by incorporating alumina into the mixture.

In addition to these, performances of selected samples were studied under different humidity conditions and experimental durations. These experiments yielded interesting implications regarding $NO_x$ adsorption-oxidation phenomena on the investigated mixed oxide surfaces. Current findings indicate that further experiments are required to fully understand the fundamental mechanisms of photocatalytic NO oxidation and storage at the molecular level.

*Keywords:* Photocatalytic $NO_x$ Oxidation-Storage, Titania, DeNOx Index, NO Conversion Activity

# ÖZET

## Titanya-Metal Oksit Fiziksel Karışımlarının UV ve Görünür Işık Altında Geliştirilmiş Fotokatalitik $NO_x$ Yükseltgeme-Depolama Performansları

MUSTAFA ÇAĞLAYAN

Kimya, Yüksek Lisans

Danışman: Emrah Özensoy

Haziran 2017

Önümüzdeki onlarca yıl boyunca fosil yakıtların (başta kömür ve doğal gaz olmak üzere) ana enerji kaynakları olarak kullanılacağı göz önüne alındığında, gaz halindeki azot oksitlerin (NO, $NO_2$, vb.) azaltılması için yeni teknolojilerin geliştirilmesi, popüler araştırma alanlarından biri olmaya devam edecektir. Bu doğrultuda birçok teknoloji geliştirilmiş ve uygulanıyor olsa da alternatif teknolojilerin geliştirilmesi hala tartışmaya açık bir konudur. Bu bağlamda, fotokatalitik metodlar bu çevre probleminin üstesinden gelmek için oldukça umut vadeden fırsatlar sunabilir; çünkü mor ötesi (UV) ve görünür ışık yardımıyla atmosferik koşullarda $NO_x$ dönüşümlerine imkan tanımaktadırlar.

Bu çalışmamızda, daha önceki çalışmalarda performans analizi için kullanılan fotonik verimliliğin yerine farklı bir analiz yöntemi önerilmiştir. Bu yöntemde, toplam NO dönüşümü ve $NO_x$ depolama seçiciliği ile birlikte "De$NO_x$ Endeksi" kullanılmıştır. Bu endeks, NO ve $NO_2$'nin zehirliliklerini göz önüne alarak toplam hava kirliliğine etkilerini göstermektedir. Bu yeni yöntem, öncelikli olarak "sol-jel birlikte çöktürme yöntemiyle" sentezlenmiş ve daha önce fotokatalitik testlerde çalışılmış $TiO_2$-$Al_2O_3$ (P2) malzemelerine uygulanmıştır. Bir sonraki aşamada ise bu P2 oksit karışımının içine toprak alkali oksidi olan CaO eklenmiş, $NO_x$ yükseltgeme/depolama üzerindeki etkileri incelenmiştir. CaO'ın P2 malzemesine eklenmesi her ne kadar $NO_x$ depolanmasını artırmışsa bile toplam NO dönüşümünü zayıflatmıştır. Bu yüzden, referans malzeme olarak kullanılan Degussa P25 $TiO_2$'in piyasada bulunan iki farklı oksit (CaO ve γ-$Al_2O_3$) ile fiziksel olarak karıştırılmasına karar verilmiştir. Bu metal oksitlerden, CaO γ-

$Al_2O_3$'e oranla $NO_x$ depolaması için "yüksek alkaliliğe" sahip olsa da γ-$Al_2O_3$'nın oksidasyon ürünlerini depolamak için yüksek yüzey alanına ve gözenekliliğe sahip olması da başka önemli bir unsurdur. Bunları göz önüne alarak, çeşitli oranlarda ikili veya üçlü karışımlar hazırlanmış, UV ve görünür ışık altında fotokatalitik testlere tabii tutulmuştur. Bu deneyler sonucunda, CaO'in γ-$Al_2O_3$'e oranla $NO_x$ depolamasını daha büyük ölçüde iyileştirdiği gözlenmiştir. Öte yandan, daha az miktarda titanya içeren yüksek performanslı üçlü karışımların alümina sayesinde elde edilebileceğini de belirtmek gerekir.

Bunlara ek olarak, bazı fiziksel karışımların farklı bağıl nem koşulları ve deney süreleri altında performansları incelenmiştir. Bu deneyler, incelenen malzemelerin yüzeylerinde gerçekleşen $NO_x$ adsorpsiyonu ve oksidasyonu ile ilgili ilginç sonuçlar sunmuştur. Fakat mevcut bulgular, moleküler düzeyde fotokatalitik NO oksidasyonu ve depolanmasının temel mekanizmalarını tamamen anlamak için yeterli olmadığından; daha detaylı çalışmaların gerekli olduğuna karar verilmiştir.

*Anahtar Sözcükler:* Fotokatalitik $NO_x$ Yükseltgenmesi-Depolanması, Titanya, DeNOx Endeksi, NO Dönüşümü Aktivitesi

# Acknowledgement

First of all, I would like to thank my advisor, Dr. Emrah Ozensoy, and Bilkent University for giving me the opportunity to work on interesting and challenging projects. This thesis would have not been completed without Dr. Ozensoy's guidance and support.

The Ozensoy Research Group has been a pleasant company. I would like to thank my groupmates Deniz Erdoğan, Kerem Emre Ercan, Merve Kurt, Mustafa Karatok, Sean McWhorther, Asad Ali Shah, Ali Vala Koç, Merve Tohumeken, Elif Perşembe, Damla Sürmeli, and Merve Balcı for making the labs great place to work in. In particular, I have really enjoyed collaborating with Aybegüm Samast on FTIR measurements.

I also would like to express my gratitude to all staff and faculty members of Chemistry Department. They have always provided friendly environment for graduate students. I wish them all continued success in their objectives.

The most importantly, I wish to announce my deepest gratitude to my huge family (Çağlayan – Poyraz - Meraki) for their continuous prayers, unconditional love and never-ending care. I also believe that my deceased mother and deceased grandmother are still with us and praying for us. My research was not going to succeed without this moral support.

And I am immeasurably indebted to Büşra Dereli who has always supported my decisions no matter how far away from her they have taken me. I wish that all the days of our lives we spend together.

Last but by no means least**,** I would like to express my deepest condolences to families who have lost loved ones in terror attacks and coup attempt. Especially; without the efforts of security forces in countering terrorism, probably there would have not been an environment to conduct a research project safely.

*"Türkiye ağır yüktür, bilmeyen ne bilesi"*

*Süleyman Çobanoğlu*

# Contents

# List of Figures

# List of Tables

# Chapter 1

# Introduction

## 1.1.$NO_x$ EMISSIONS

In today's world, air pollution is still one of the major issues mankind tries to overcome. Atmospheric pollutants (*e.g.* sulfur dioxide, carbon monoxide, volatile organic compounds, ground level ozone *etc.*), have a variety of detrimental effects on environment and living organisms. Along with severe health problems such as ischaemic heart disease, acute lower respiratory infections, lung cancer; acid rains, climate change, haze and eutrophication can be considered as some of the critical air pollution related problems [1].

Nitrogen oxides ($NO_x$) constitute a very imperative family of chemicals with several adverse effects. Due to their contribution to secondary particulate aerosols and tropospheric ozone ($O_3$) formation, $NO_x$ species can be linked both directly and indirectly to various environmental and health problems [2]. In general, $NO_x$ emission sources can be studied under two groups; anthropogenic sources and natural (biogenic) sources. While cement production, fossil-fuel combustion, iron mills and petroleum refineries are some examples for anthropogenic sources; forest fires, lightning and yeasts are examples for the latter one [3]. According to European Environmental Agency (Figure 1) [4], among other anthropogenic sources, road transport and energy production are the leading contributors to $NO_x$-related air pollution (40.5% and 22.5% contribution, respectively).

When the latest $NO_x$ emission rates (kg/capita) of OECD (Organisation for Economic Co-operation and Development) countries are compared, it is obvious that Turkey has one of the lowest rates (Figure 2) [5]. This result indicates that despite having a great potential for economic/industrial growth, Turkey has to leap a great gap in terms of industrialization and

energy production. Interestingly $NO_x$ emission rates in Turkey has also some correlation with the economic growth/industrialization as can be inferred indirectly from Figure 3. In addition to these, the emission inventories for Turkey from EMEP (European Monitoring and Evaluation Programme) are listed in Table 1 [2]. Based on this inventory; in 2010, the road transport and combustion in energy and transformation industry is responsible for the 2/3 of the total national $NO_x$ generation.

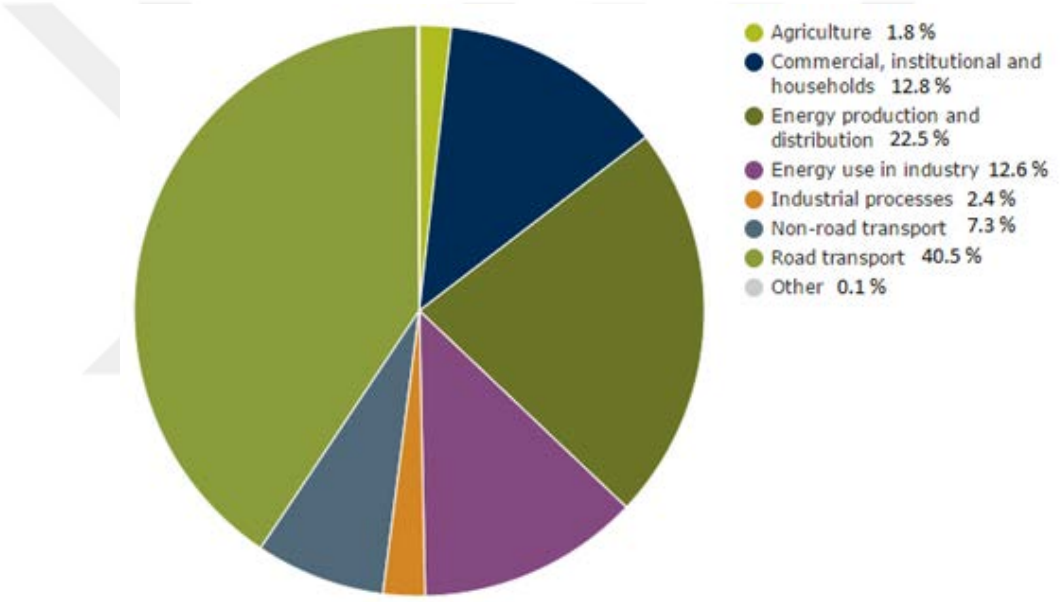


**Figure 1.** Sector share of $NO_x$ emissions in Europe 2011 (Copyright notice © European Environmental Agency, 2017 [4])

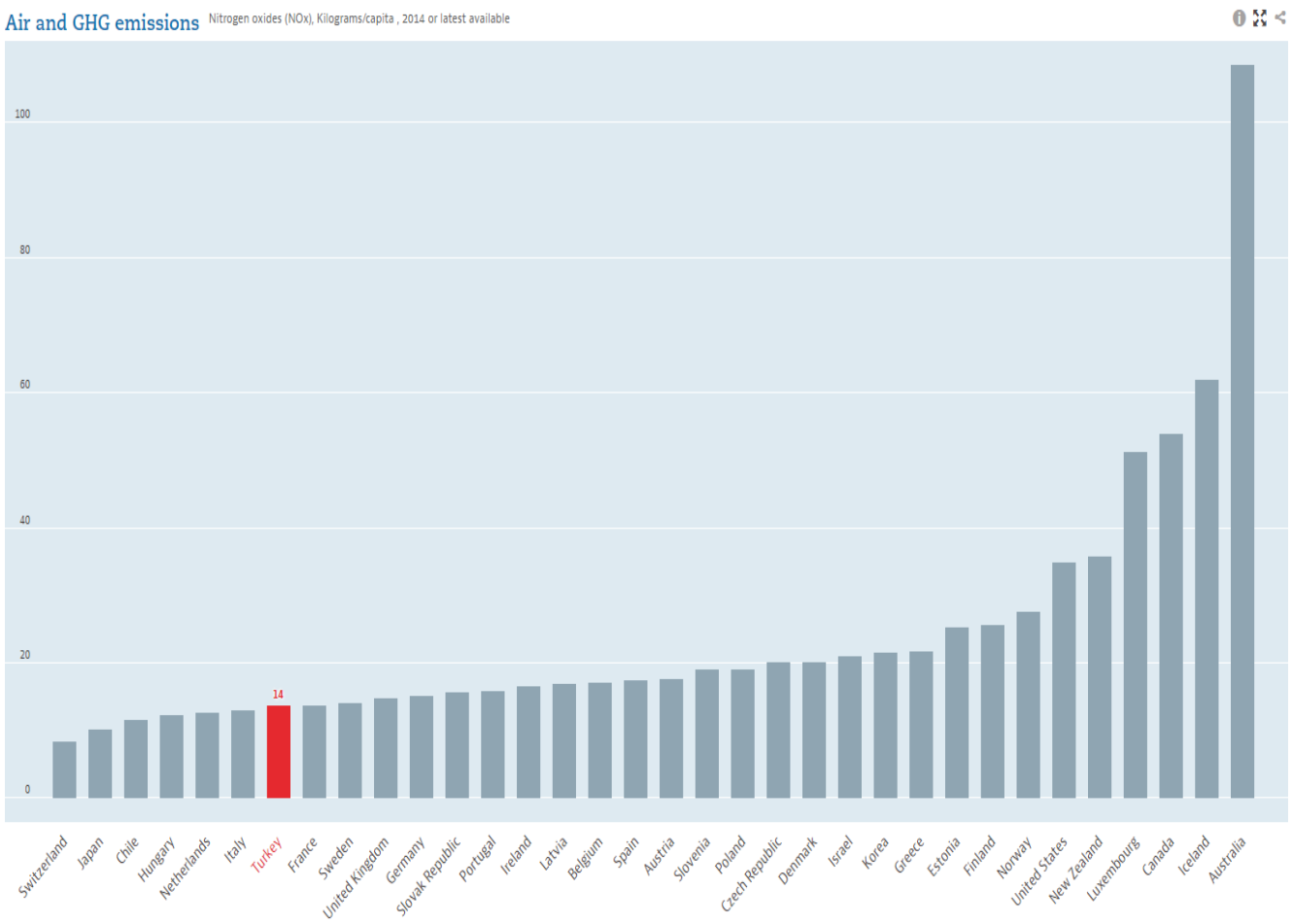


**Figure 2.** Latest $NO_x$ emission rates (kilograms/capita) of OECD countries (Copyright notice © OECD, 2017 [5])

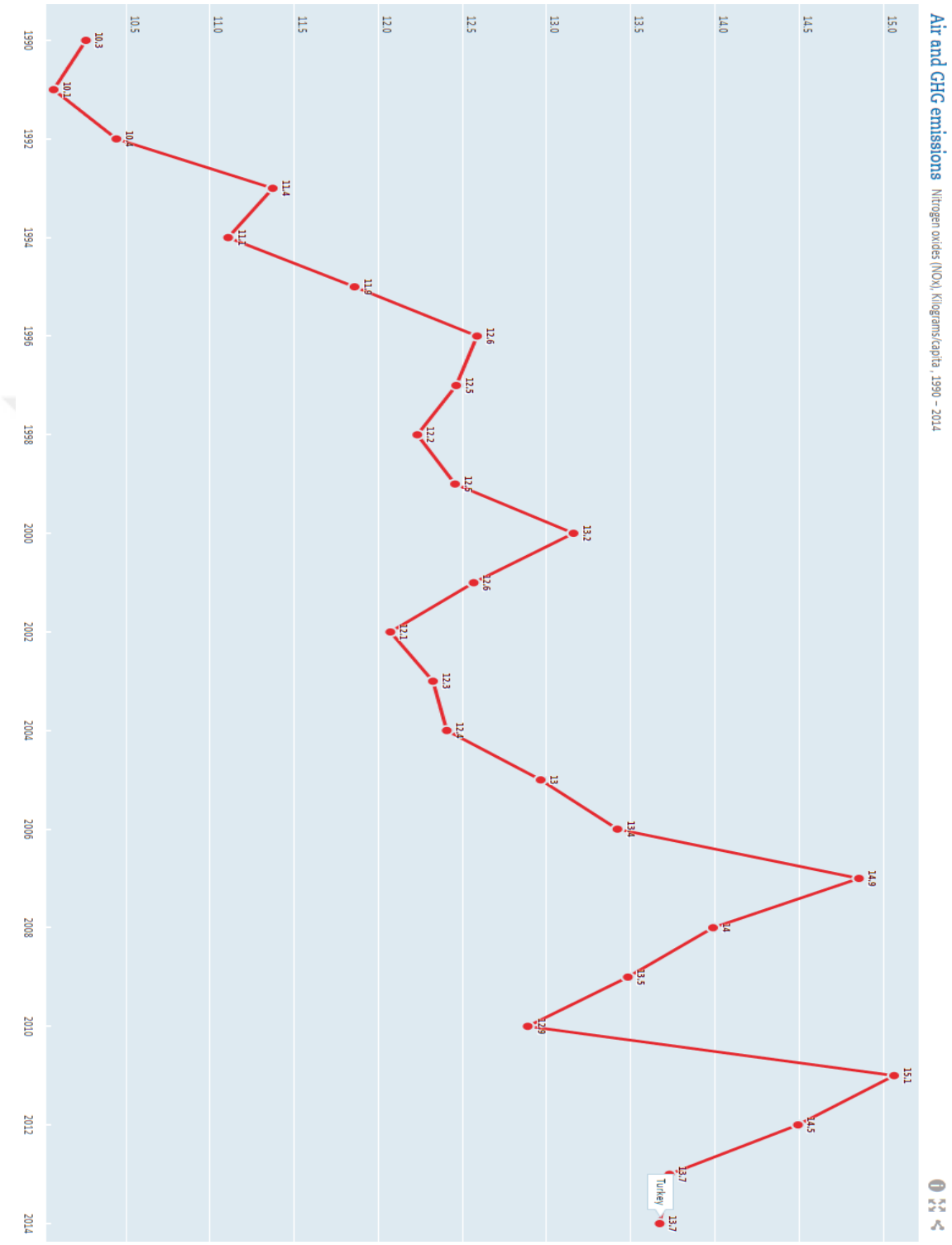


**Figure 3.** Turkey's $NO_x$ emission rates (kilograms/capita) between 1990 and 2014 (Copyright notice © OECD, 2017 [5])

**Table 1.** The $NO_x$ emission inventories of Turkey in 2009 and 2010 [2]

| Sources of Air Pollution | EMEP (thousand tonnes) | |
|---|---|---|
| | **2009** | **2010** |
| **S1- Combustion in energy and transformation industry** | 341,493 | 329,176 |
| **S2- Non-industrial combustion** | 76,369 | 73,230 |
| **S3- Combustion in manufacturing industry** | 87,295 | 100,765 |
| **S4- Production processes** | 6,797 | 8,073 |
| **S5- Extraction/distribution fossil/geothermal energy** | - | - |
| **S6- Solvent use and other product use** | - | - |
| **S7- Road transport** | 395,214 | 375,397 |
| **S8- Other mobile sources and machinery** | 53,216 | 57,290 |
| **S9- Waste treatment and disposal** | 616 | 439 |
| **S10- Agriculture** | 0 | 0 |
| **TOTAL** | 961,000 | 945,000 |

## 1.2.$NO_x$ GENERATING FUELS AND $NO_x$ GENERATION MECHANISMS

When the sector share of anthropogenic $NO_x$ emissions is analyzed, it is apparent that $NO_x$ generation is mainly related to combustion processes. In these processes; most of the produced $NO_x$ is in the form of nitric oxide (NO), while nitrogen dioxide ($NO_2$) concentration is relatively low [6]. Ratio of NO amount to total $NO_x$ amount for emissions of different combustion processes is represented in Table 2.

**Table 2.** $NO/NO_x$ generation ratios of different fossil fuel-based energy transformation systems [6]

| Source Type | $NO/NO_x$ Ratio |
|---|---|
| Industrial Boilers | |
| • Natural Gas | 0.90 |
| • Coal | 0.95 |
| • Fuel Oil | 0.96 |
| Motor Vehicles | |
| • Internal Combustion Engine | 0.99 |
| • Diesel Powered Car | 0.77 |
| Petroleum Refinery Heater: Natural Gas | 0.93 |
| Gas Turbine Electrical Generator: Fuel Oil | 0.55 |

During combustion, $NO_x$ molecules are formed via oxidation of $N_2$ in air or combustion nitrogen containing species in fossil fuels. Nitrogen in fuels is present predominantly as pyridine and/or pyrrole species (Figure 4) [6].


**Figure 4.** Pyridine and pyrrole [6]

Therefore; while the combustion of high purity methane leads to $NO_x$ via oxidation of $N_2$ in air; combustion of coal or heavy oils containing significant amounts of nitrogen derivatives contributes via both pathways. Chemical formation mechanisms of $NO_x$ can be categorized in two main groups; namely, thermal $NO_x$ formation and flame $NO_x$ formation [7].

### 1.2.1. THERMAL $NO_x$

The thermal route can be described as the oxidation of nitrogen molecules at high temperatures (T ≥1600-2000 $^oC$) [7]. In this route, the generation rate is mainly dependent on the gas residence time and the temperature in the combustion chambers. The consecutive elementary reactions (*Equation 1* and *2*) of this pathway were first proposed by Zeldovich in 1946 [8].

$$N_2 + O \leftrightarrow NO + N \quad (1)$$

$$O_2 + N \leftrightarrow NO + O \quad (2)$$

Among the reactions shown above, reaction (*1*) is the one determining the rate of formation of NO due to high activation energy to break the strong nitrogen triple bond [7]. In 1970, these reactions were extended with the reaction of atomic nitrogen and hydroxyl groups (*Equation* 3), which makes significant contribution to the thermal production [9].

$$N + OH \leftrightarrow NO + H \quad (3)$$

Later, it was supplemented by considering the effect of nitrous oxide as shown in *Equations 4*, *5* and *6* [10].

$$N_2O + M \leftrightarrow N_2 + O + M \quad (4)$$

$$N_2O + O \leftrightarrow 2NO \quad (5)$$

$$N_2O + O \leftrightarrow N_2 + O_2 \quad (6)$$

### 1.2.2. FLAME $NO_x$

In some cases, $NO_x$ formation can be achieved by mechanisms distinct from the thermal ones. One of these routes, named as “flame mechanism”, consists of the reactions having C, H, O

and N-containing compounds inside the flame zones. There are various chemical mechanisms involved, all linked to intermediates that may exist only in the reaction zone of the flame [7]. Among these, the first discovered (in 1971) and well-known one is Fenimore mechanism leading to what is termed as prompt $NO_x$ [11]. Although the actual formation consists of a complex series of reactions, Fenimore mechanism can be understood in general by considering the following reactions:

$$CH + N_2 \leftrightarrow HCN + N \quad (7)$$

$$N + O_2 \leftrightarrow NO + O \quad (8)$$

$$HCN + OH \leftrightarrow CN + H_2O \quad (9)$$

$$CN + O_2 \leftrightarrow NO + CO \quad (10)$$

In addition to the Fernimore mechanism, some of the other prominent flame reactions are:

- NNH mechanism, principal reaction: [12]

$$NNH + O \leftrightarrow NH + NO \quad (11)$$

- NO formation via nitrous oxide ($N_2O$), principal reaction: [13]

$$N_2O + CH_3 \leftrightarrow CH_2NH + NO \quad (12)$$

- Basic mechanism via NCN, key reaction: [14]

$$CH + N_2 \leftrightarrow NCN + H \quad (13)$$

## 1.3.TITANIA-BASED PHOTOCATALYSIS: PAST AND TODAY

The history of $TiO_2$ as a photoactive material can be started from 1930s. In 1938, C. F. Goodeve and J. A. Kitchener discovered that dyes can be bleached via active oxygen species formed on the titania surface [15]. At that time; instead of using the term *photocatalyst*, they called titania a *photosensitizier* as it was realized that titania did not change through the reaction. The first time that titania was referred to as a photocatalyst was in 1956 by S. Kato and F.

Mashio [16]. In their work entitled "Autooxidation by $TiO_2$ as a Photocatalyst", it was reported that titania dispersed in various organic solvents initiates autoxidation of organic compounds and formation of hydrogen peroxide ($H_2O_2$) under a mercury lamp. However; until the late 1960s, titania drew limited attention of researchers in the field of catalysis and photochemistry. For the first time in 1969, setup for photo-electrochemical water splitting was demonstrated and tested (as shown in Figure 5) [16]. And in 1972, this work published in Nature by A. Fujishima and K. Honda attracted great attention due to crude oil crisis in 1970s [17].

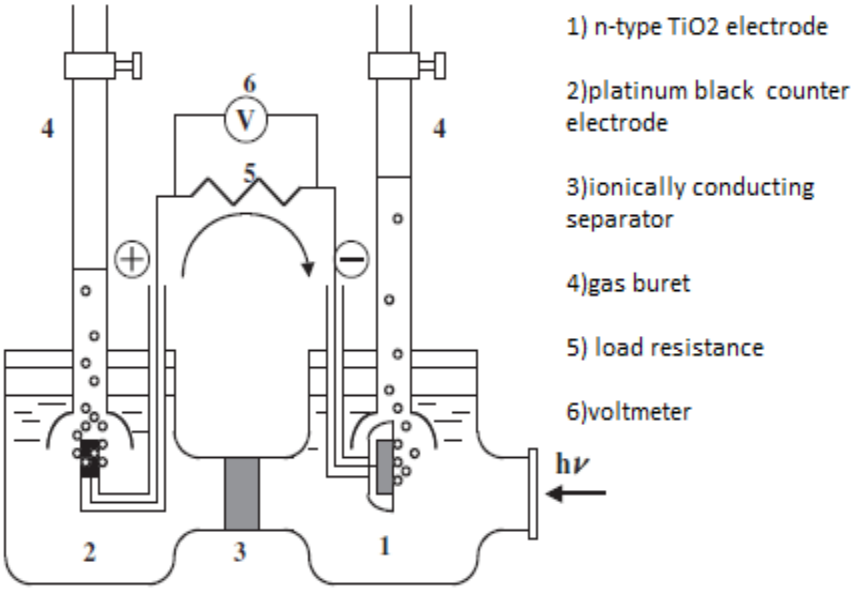


**Figure 5.** Schematic diagram of electrochemical photocell (Copyright notice © The Japan Society of Applied Physics, 2017 [16])

When this remarkable work done by A. Fujishima and K. Honda is studied, it could be seen that photons having shorter wavelengths than titania's bandgap, *ca.* 415 nm (*i.e.* 3.0 eV), generates current flowing from platinum electrode to the titania electrode. Thus, the direction of the photocurrent shows that oxidation reaction takes place on $TiO_2$ surface and the reduction occurs at the Pt counter electrode [16]. Whole process can be summarized based on the following reactions.

Light irradiation:

$$TiO_2 + h\nu \rightarrow e^- + h^+ \quad (14)$$

On titania surface:

$$2H_2O + 4h^+ \rightarrow O_2 + 4H^+ \quad (15)$$

On platinum surface:

$$2H^+ + 2e^- \rightarrow H_2 \quad (16)$$

Overall reaction:

$$2H_2O + 4h\nu \rightarrow O_2 + 2H_2 \quad (17)$$

As revealed in Figure 6, the increase in the number of publications related to titania-based photocatalysis started in 1970s-1980s. Especially since 1990s, this number has been growing tremendously due to the demand on renewable energy sources [18].


**Figure 6.** Annual number of publications related to titania-based photoactive materials research topics when survey is done in Web of Science (Copyright notice © The Royal Society of Chemistry, 2017 [18])

In today's world, main investigation on photocatalysts including titania has been concentrated on improving the solar energy conversion efficiency which focus on three main

topics. As titania is mainly an UV active material, shifting its bandgap into the visible-light region would allow more photons to be absorbed because solar photon flux consists of 5% UV (300-400 nm), 43% visible (400-700 nm) and 52% infrared (700-2500 nm) photons [19]. Thus, introducing assorted dopants (metal or nonmetal) into titania's lattice is one of the most common methods to improve the light absorption. In most of such cases, doping process ends with either the occurrence of isolated impurity states within the band gap or direct narrowing of the gap [20]. In Figure 7, it is shown that different metal dopants result in different scenarios depending on their position with respect to valence and conduction band of titania [21]. Former studies in the literature indicate that the activity of these doped materials depends on dopant concentration, distribution of dopants, electron donor density and incident light intensity [22].

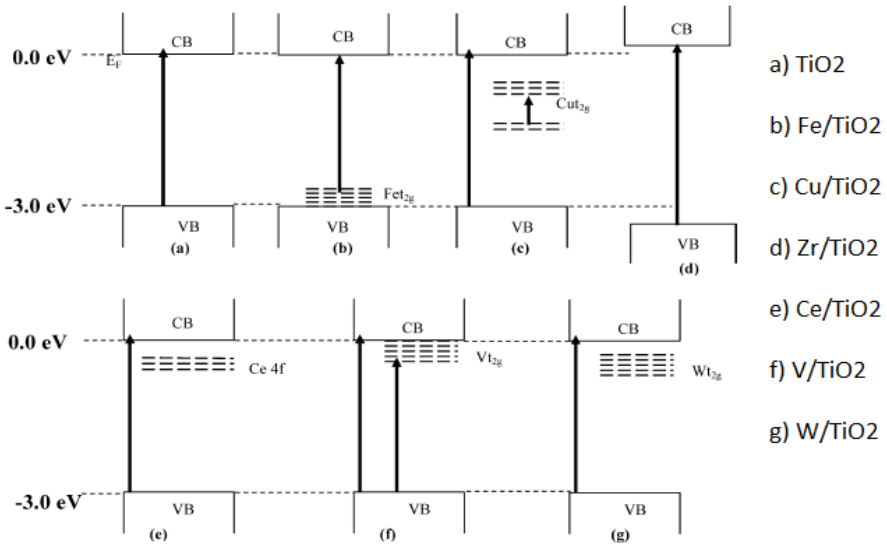


**Figure 7.** Schematic representation of energy levels of various metal dopants in $TiO_2$ (Copyright notice © American Chemical Society, 2017 [21])

Another focus of interest in titania photocatalysis is charge separation; because rapid electron-hole recombination limits the total activity of the material. To achieve a successful catalytic surface redox reaction on the photocatalytic material, electrons and holes formed after photon absorption are needed to migrate to the surface. Therefore, the pathway to the surface and lifetime of excitons are important parameters when the charge carriers recombine faster than the desired reactions. One of the possible ways to keep electron-hole pairs separated is the utilization of dopants. For instance; the metal ions may provide trap states for electrons or holes based on

the position of the generated electronic states with respect to the conduction and valence bands [22]. When charge separation properties of metal dopants are studied, it is typically observed that usually electron trapping is much faster than hole trapping as shown below [22].

$TiO_2 + h\nu \rightarrow e^- + h^+$ (t=$10^{-15}$ sec) (18)

$e^- \rightarrow e^-_{trapped}(M^{n+} or\ O_2)$ (t=30x$10^{-12}$ sec) (19)

$h^+ \rightarrow h^+_{trapped}(M^{n+1} or\ OH^-)$ (t=250x$10^{-12}$ sec) (20)

In addition to doping process, the creation of heterojunctions is another solution for charge recombination issue. In this method, excitons formed in one photocatalyst can be subsequently transferred to another material [23]. Heterojunction studies in the literate can be divided into five groups; conventional, p-n, surface, direct z-scheme, semiconductor/graphene heterojunctions [24]. Figures 8-12 depict simplified electron transfer routes for some of the most common heterojunction systems. Particular examples of such heterojunctions involving titania domains are also listed in Table 3.

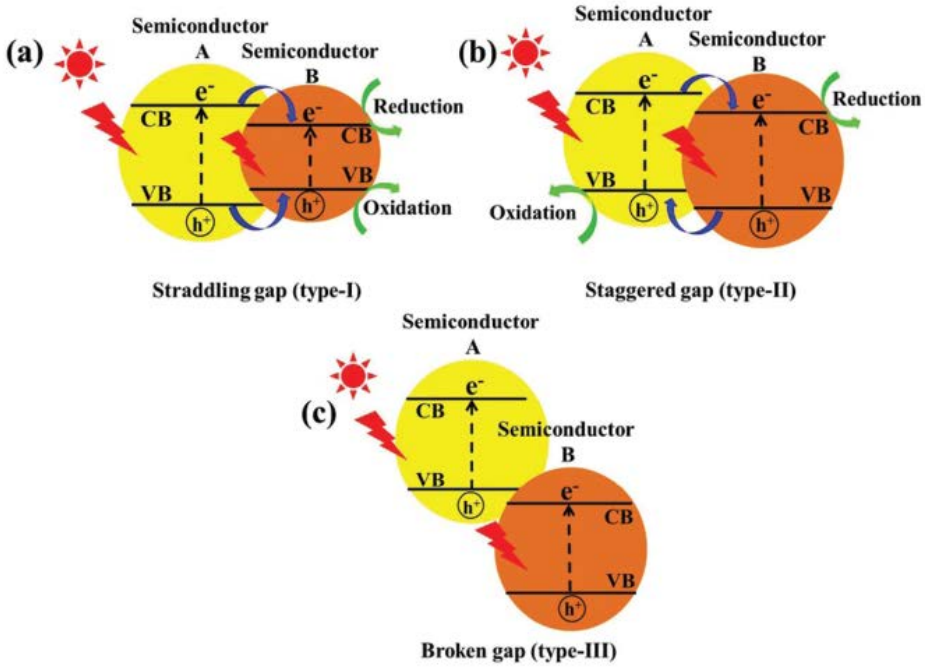


**Figure 8.** Illustration of three different types of conventional light-responsive heterojunction photocatalysts (Copyright notice © John Wiley and Sons, 2017 [24])

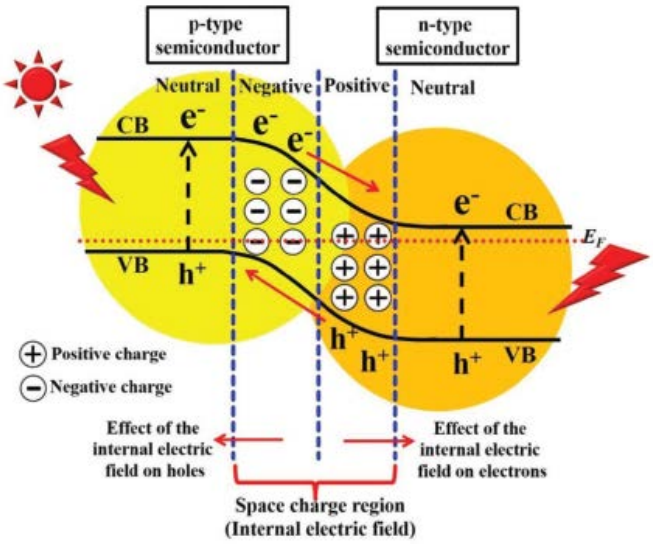


**Figure 9.** Illustration of the electron–hole separation under the effect of the internal electric field of a p–n heterojunction photocatalyst under light (Copyright notice © John Wiley and Sons 2017, [24])

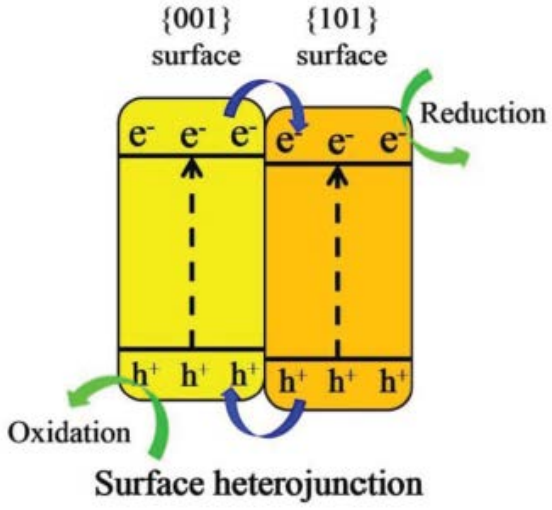


**Figure 10.** Illustration of the electron–hole separation on the surface of anatase titania with an optimal ratio of the exposed {001} and {101} facets (Copyright notice © John Wiley and Sons, 2017 [24])

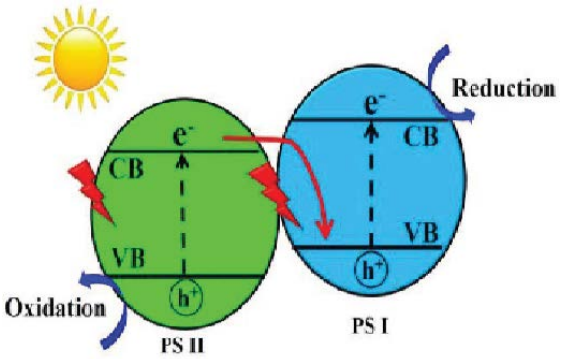


**Figure 11.** Illustration of a direct z-scheme heterojunction photocatalyst under light (Copyright notice © John Wiley and Sons, 2017 [24])

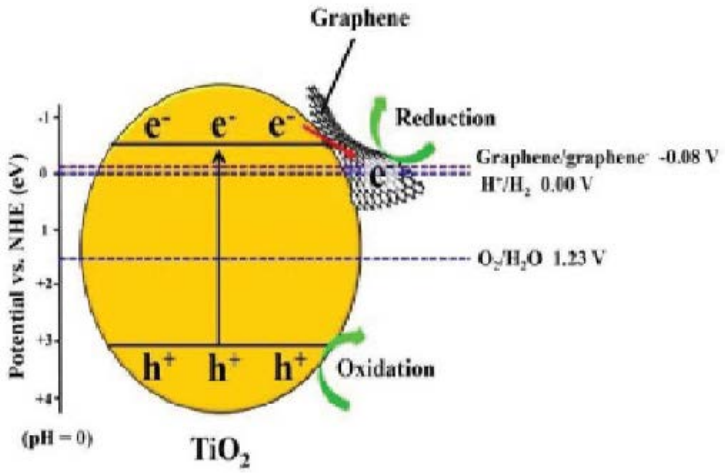


**Figure 12.** Illustration of the photocatalytic mechanism on Graphene/$TiO_2$ nanosheets (Copyright notice © John Wiley and Sons, 2017 [24])

**Table 3.** Titania based heterojunction examples in recent years

| **Heterojunction Sample** | **Heterojunction Type** | **Photocatalytic Application** | **Year** | **Reference** |
|---|---|---|---|---|
| SnO – $TiO_2$ | Conventional Type II | Rhodomine B Degradation | 2008 | [25] |
| NiO – $TiO_2$ | p-n Type | p-Chlorophenol Degradation | 2010 | [26] |
| {001} - {101} $TiO_2$ | Surface Type | $CO_2$ Reduction | 2014 | [27] |
| g-$C_3N_4$ - $TiO_2$ | Direct Z-Scheme Type | Formaldehyde Decomposition | 2013 | [28] |

| | | | | |
|---|---|---|---|---|
| Graphene - $TiO_2$ nanosheets | Semiconductor-Graphene Type | Hydrogen Production | 2011 | [29] |

Finally; as redox reactions occur on the material surface, the surface reactivity of titania is another important topic to investigate. Surface atomic arrangement and coordination has a great influence on the adsorption of reactants, surface charge transfer to reactants, and the desorption of products [30]. Therefore, the heterogeneous catalysis applications (gas-solid or liquid-solid interfaces) are sensitive to surface atomic structure which can be modified by controlling the surface morphology. Thanks to the recent developments in nanoscience and nanotechnology, nature and relative abundance of the surface crystal facets of photocatalysts can be fine-tuned to optimize the activity (Figure 10). It should be noted that utilization of doping and heterojunctions has also strong influence on the surface reaction mechanisms [31]. For instance, it was found out that introducing of noble metals on semiconductor surfaces can enhance the yield of a desired product and change the reaction mechanism.

## 1.4.CRYSTAL STRUCTURE OF TITANIA: ANATASE vs RUTILE

Since the photocatalytic activity is closely related to the crystal structure of titanium dioxide, it is essential to investigate the properties of different crystal structures of titania in a comparative manner. In the literature, it is reported that rutile and anatase are the most common crystal phases under atmospheric pressures [32]. Besides brookite phase is also another observable phase under atmospheric pressure, which is relatively more difficult to be synthesized [32]. In addition to all of these, there are also high-pressure phases of titania reported in the literature (*e.g.* $TiO_2$-II [Srilankite], cubic fluorite-type, pyrite-type, monoclinic baddeleyite-type, cottunnite-type polymorphs *etc*.), however, they have little activity in photocatalytic applications [32].

When the bulk stability was studied in terms of thermodynamics, it was predicted that rutile phase is the most stable one at all temperatures and pressures up to sixty thousand bar (Figure 13) [33]. On the other hand; relatively small stability differences between three phases

(*i.e.* rutile, anatase and brookite) in terms of Gibbs free energy (4-20 kJ/mol) indicate that anatase and brookite may be considered as metastable phases which can also be observed along with rutile under atmospheric conditions. Furthermore, the transformation from anatase to rutile at room temperature is kinetically hindered, rendering anatase a metastable state that can exist under atmospheric conditions for long durations of time. The transformation speed reaches measurable levels at temperatures typically higher than 600 $^{o}$C [33]. Moreover; in numerous titania synthesis protocols, the crystalline phase that is formed at low temperatures is usually anatase. This observation can be attributed to the lower surface free energy of anatase as compared to that of rutile favoring the crystallization of anatase polymorph instead of rutile [32].

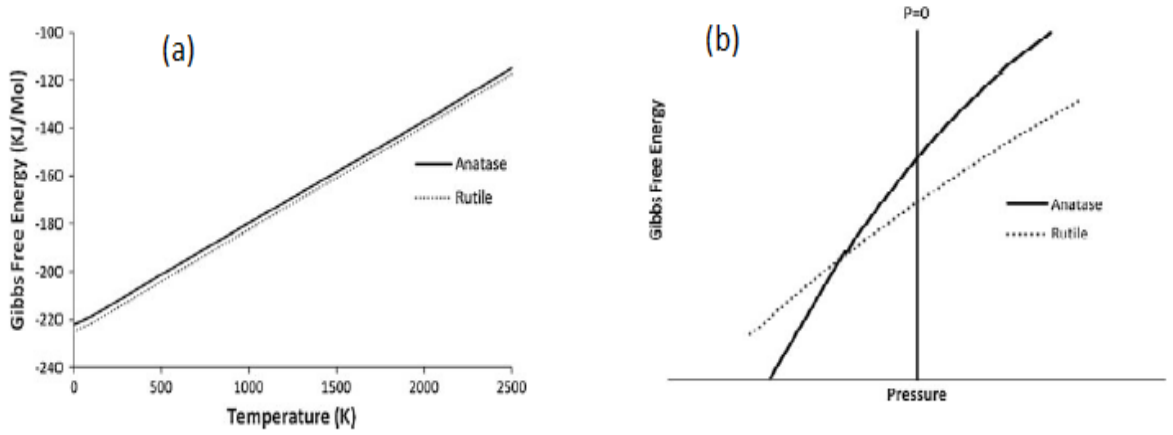


**Figure 13.** For anatase and rutile polymorphs, (a) Gibbs Free Energy vs. Temperature - (b) Gibbs Free Energy vs. Pressure (Copyright notice © Springer, 2017 [32])

While doing analysis in nanoscale, it should be remembered that the relative stability of titania polymorphs may change [34]. Under atmospheric conditions; anatase is the most thermodynamically stable polymorph for particles smaller than 11 nm, while for the particle sizes ranging from 11 nm to 35 nm, brookite appears to be the most stable one. For particles bigger than 35 nm, rutile is the most stable phase [35].

Crystal structures of the prevalent polymorphs of titania (*i.e.* anatase, rutile and brookite) are commonly represented using octahedra ($TiO_6^{2-}$) [33]. As depicted in Figure 14, the major differences between these crystal structures originate from the various distortions of octahedra

and the changes in the assembly patterns of the octahedral chains. While octahedra are connected by their vertices in the anatase phase; rutile phase is constructed by the connections of octahedra at the edges. On the other hand, in brookite, octahedra are connected through both edges and vertices [33].

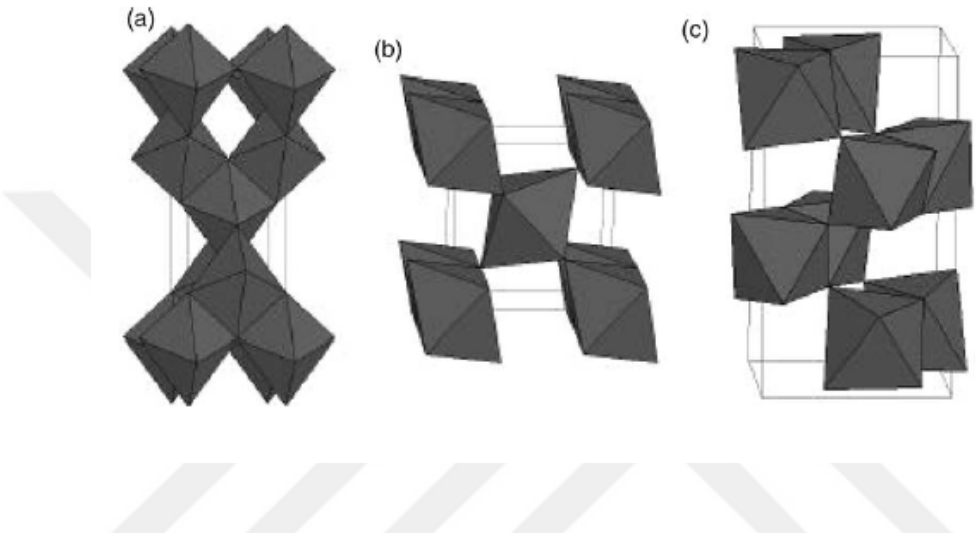


**Figure 14.** Illustration of octahedra in three crystal phases (a) anatase, (b) rutile, (c) brookite (Copyright notice © Elsevier, 2017 [33])

Anatase polymorph typically comprises of two particular low-energy surfaces namely, {001} (minority facets) and {101} (majority facets) [35]–[37]. Although {101} facet is the dominant one (more than 94 %, according to the Wulff construction which involves a methodology for estimating the shape of an equilibrium crystal considering the Gibbs thermodynamic principle, by minimizing the total surface free energy associated to the crystal-medium interface), {001} is the most reactive facet [36]. Additionally, less common {100} facet can be observed readily on rod-like anatase grown hydrothermally in basic environments [35]. Based on Wulff construction, although the calculated surface energy of {010} facet, 0.53 J/m$^2$, is between {001}-0.90 J/m$^2$ and {101}-0.44 J/m$^2$, there is no {010} in equilibrium shape [30]. On the other hand, rutile crystal phase has three primary facets. Among these, {100} and {110} are quite low in Gibbs free energy, thus they are practically relevant for polycrystalline and powder materials. While the latter one is the most thermally stable; the third, {001}, is less stable one due to having the highest surface energy [30], [35]. In the literature; it has been reported that

{011} of rutile and {001} of anatase provide favorable sites for oxidation, whereas {110} of rutile and {101} of anatase serve sites for reduction [38]. The equilibrium shapes of anatase and rutile based on Wulff construction are shown in Figure 15.

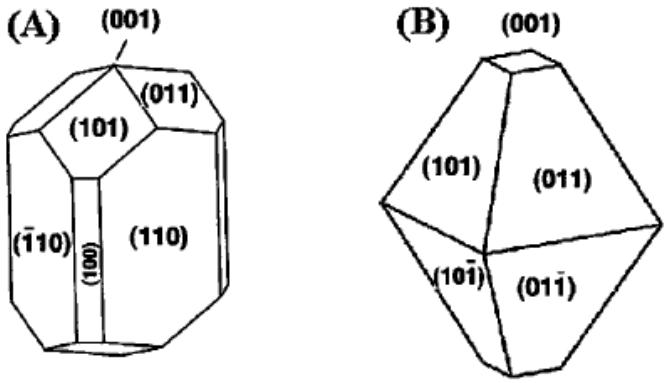


**Figure 15.** The equilibrium shapes of (a) rutile and (b) anatase based on Wulff construction calculated via surface Gibbs energies (Copyright notice © The Royal Society of Chemistry, 2017 [37])

Titania is classified as an n-type semiconductor due to the presence of a small amount of oxygen vacancies [38]. The molecular-orbital bonding structure for anatase titanium dioxide is shown in Figure 16, with representation of atomic levels, crystal-field split levels and final interaction states. While the nonbonding O $p_{\pi}$ orbital is at the top of the valence bands, the nonbonding $d_{xy}$ states are located at the bottom of the conduction bands [39]. Due to having smaller metal-metal distance and denser phase, in rutile polymorph the bottom of the conduction band lies lower than the one in anatase [38], [39]. In Figure 17, a comparison of the calculated electronic density of states for bulk rutile and anatase polymorphs is given.

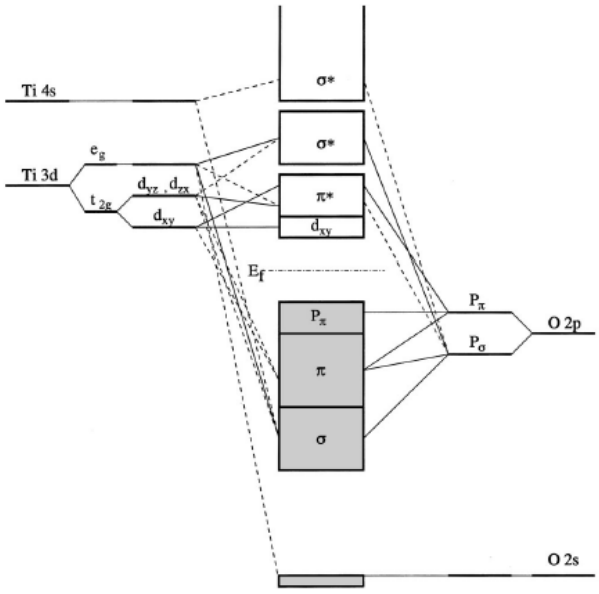


**Figure 16.** Molecular-orbital bonding structure for anatase phase (Copyright notice © American Physical Society, 2017 [39])

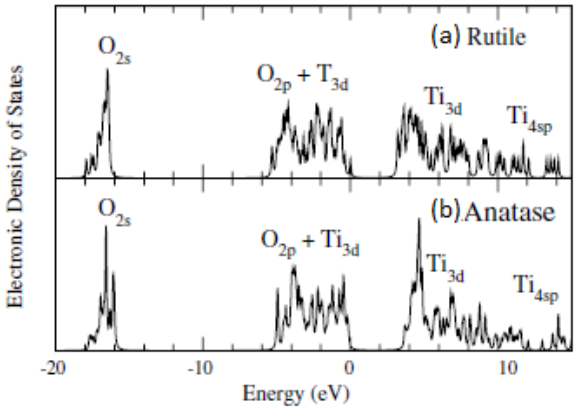


**Figure 17.** Electronic density of states for bulk (a) rutile and (b) anatase. the valence band maximum is taken as 0 eV (Copyright notice © IOP Publishing, 2017 [40])

In most of the applications, anatase gives better photocatalytic performance than rutile although it has larger band gap as mentioned before. The reason is considered to lie in the facts that there are higher density of localized states due to surface-absorbed hydroxyl radicals, and slower charge carrier recombination rate in anatase relative to rutile [32]. The high

recombination rate of rutile polymorphs is generally attributed to the larger grain size and its lower capacity to absorb species [32].

Some of the fundamental properties of anatase and rutile are also summarized in Table 4.

**Table 4.** Properties of anatase and rutile crystal phases of titania [32]

| **Property** | **Anatase** | **Rutile** |
|---|---|---|
| Crystal Structure | Tetragonal | Tetragonal |
| Atoms per Unit Cell | 4 | 2 |
| Unit Cell Volume ($nm^3$) | 0.1363 | 0.0624 |
| Density ($kg/m^3$) | 3894 | 4250 |
| Calculated Indirect Band Gap<br>(eV)<br>(nm) | <br>3.23-3.59<br>345.4-383.9 | <br>3.02-3.24<br>382.7-410.1 |
| Experimental Band Gap<br>(eV)<br>(nm) | <br>~3.2<br>~387 | <br>~3.0<br>~413 |
| Refractive Index | 2.54, 2.49 | 2.79, 2.903 |
| Solubility in HF | Soluble | Insoluble |
| Solubility in $H_2O$ | Insoluble | Insoluble |
| Hardness (Mohs) | 5.5-6 | 6-6.5 |
| Bulk Modulus (GPa) | 183 | 206 |

### 1.4.1. DEGUSSA P25 $TiO_2$: THE BENCHMARK PHOTOCATALYST

Degussa P25 is a widely used commercial photocatalyst due to its relatively high activity in various photocatalytic reactions. It is mainly composed of anatase and rutile crystalline phases of titania with reported anatase/rutile ratios ranging from typically 85/15 to 70/30 [41]. However, exact phase composition of Degussa P25 is still debatable due to the lack of a statistically precise/accurate methodology to determine crystalline contents at the nanoscale. Ohtani *et al.* who developed a technique to separate crystalline phases by using a mixed solution of hydrogen

peroxide and ammonia reported that there are discrepancies in the phase composition of commercial Degussa P25 samples obtained from the same material batch which are synthesized by identical procedure [41]. As shown in Table 5, they also reported that P25 also contains a certain extent of amorphous titania.

**Table 5.** Crystal phase composition of P25 collected from the same package [41]

| **Entry** | **Composition %** | | |
|---|---|---|---|
| | **Anatase** | **Rutile** | **Amorphous** |
| **1** | 78 | 14 | 8 |
| **2** | 73 | 14 | 13 |
| **3** | 82 | 16 | 2 |
| **4** | 83 | 17 | 0 |
| **5** | 84 | 16 | 0 |
| **6** | 85 | 15 | 0 |

In the same study, Ohtani and his colleagues argued that phases of titania behaved independently when working as a photocatalyst; in spite of the former reports suggesting that co-presence of different titania phases caused the high-level activity of P25. In these earlier reports emphasizing the superiority of anatase-rutile heterojunctions, transfer of electrons and holes between interconnecting anatase and rutile particles was argued to reduce the charge recombination and hence improve the efficiency of the utilization of electron–hole pairs [41].

Some of the physical properties of P25 reported in the literature and also provided by the manufacturer are summarized in Table 6.

**Table 6.** Some physical properties reported in literature [42]–[45]

| | |
|---|---|
| **Surface Area (BET)** | 35-65 $m^2/g$ |
| **Primary Particle Size (TEM)** | 21 nm |
| **Pore Volume** | 0.177-0.25 $cm^3/g$ |
| **Pore Size** | 7.57-17.5 nm |

## 1.5.PHOTOCATALYTIC $NO_x$ REMOVAL

Due to the harmful effects on environment and health, various methods for $NO_x$ removal have been developed. These methods can be classified into two groups, primary and secondary procedures [46]. The primary methods mainly consist of $NO_x$ removal techniques applied before or inside a combustion zone, whereas the secondary methods are post-combustion processes usually including additional equipment [7]. Some main primary and secondary methods are shown in Figure 18.

Semiconductor based photocatalysts provide environmentally friendly and sustainable opportunities for air pollution control. Thus, their exploitation in the removal of volatile organic compounds and nitrogen oxides is becoming increasingly popular worldwide. There are three main methods for $NO_x$ removal by photocatalysis; photo-selective catalytic reduction (photo-SCR), photo-oxidation and photo-decomposition [7]. Each of these methods have certain advantages and disadvantages as discussed in following sub-sections.

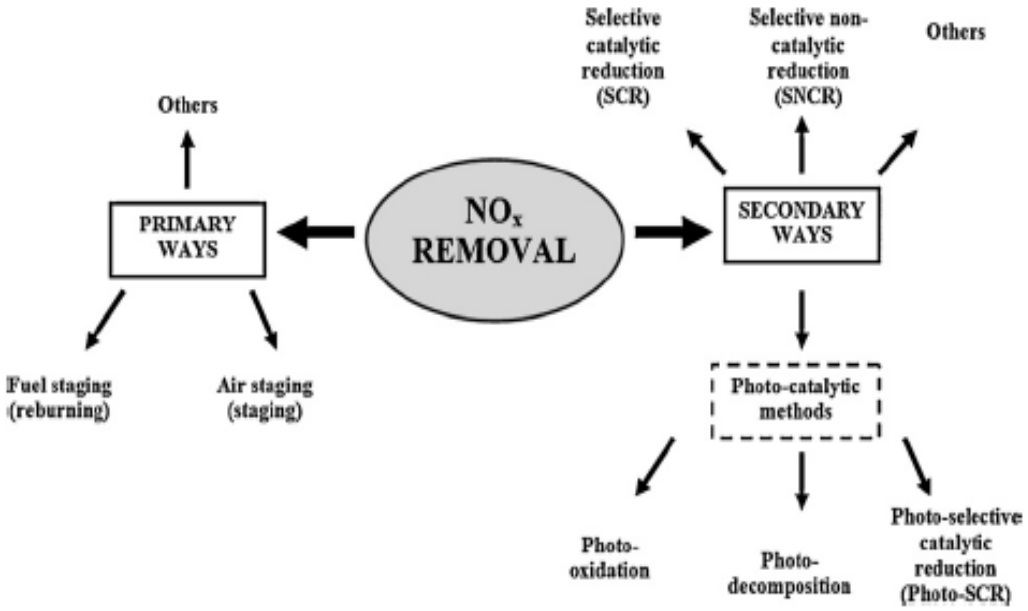


**Figure 18.** Some of the main methods for $NO_x$ removal (Copyright notice © Elsevier, 2017 [7])

### 1.5.1. PHOTO-DECOMPOSITION

In the photo-decomposition process, the aim is to decompose $NO_x$ molecules into $N_2$ and $O_2$. In literature, most of the studies focused on increasing the decomposition activity and enhancing the selectivity towards $N_2$ [7]. Possible mechanisms for photo-decomposition of NO proposed by Bowering *et al.* are [47]:

$$TiO_2 + h\nu \rightarrow e^- + h^+ \quad (28)$$

$$NO_{(ads)} + e^- + h^+ \rightarrow N_{(ads)} + O_{(ads)} \quad (29)$$

$$NO_{(ads)} + N_{(ads)} \rightarrow N_2O_{(ads)} \quad (30)$$

$$NO_{(ads)} + O_{(ads)} \rightarrow NO_{2(ads)} \quad (31)$$

$$2O_{(ads)} \rightarrow O_{2(ads)} \quad (32)$$

$$2N_{(ads)} \rightarrow N_{2(g)} \quad (33)$$

$$2NO_{(ads)} \rightarrow N_{2(g)} + O_{2(g)} \quad (34)$$

$$2N_2O_{(ads)} \rightarrow N_{2(g)} + O_{2(ads)} \quad (35)$$

In addition to the above mechanism, there is also an alternative mechanism as shown below [48]:

$$TiO_2 + h\nu \rightarrow e^- + h^+ \quad (36)$$

$$O^{2-}{}_{(cus)} + h^+ \rightarrow O^-{}_{(cus)} \quad (37)$$

$$NO_{(ads)} + e^- \rightarrow NO^-{}_{(ads)} \quad (38)$$

$$NO^-{}_{(ads)} + O^-{}_{(cus)} \rightarrow N_{(ads)} + O_{(ads)} + O^{2-}{}_{(ads)} \quad (39)$$

The abbreviation "*cus*" stands for "coordinatively unsaturated". The above reactions are followed by following ones:

$$N_{(ads)} + N_{(ads)} \rightarrow N_{2(ads)} \rightarrow N_{2(g)} \quad (40)$$

$$N_{(ads)} + NO_{(ads)} \rightarrow N_2O_{(ads)} \rightarrow N_2O_{(g)} \quad (41)$$

$$O_{(ads)} + O_{(ads)} \rightarrow O_{2(ads)} \rightarrow O_{2(g)} \quad (42)$$

In this process, the major product is nitrous oxide [7]. However; in the presence of high amount of gaseous oxidizers (*e.g.* oxygen, water), formation rates of nitrogen dioxide and nitrates increase. Thus, it can be stated that the product distribution of photo-decomposition of NO strongly depends on the reaction conditions. In addition to the reaction conditions, it was also observed that there is a strong relation between the coordination number of the $Ti^{4+}$ species and selectivity towards $N_2$ [49], [50]. As shown in Figure 19, the lower the coordination number becomes; the higher efficiency and selectivity can be obtained for Ti-oxide species. Moreover, the lifetime of excitons on isolated tetrahedral $Ti^{4+}$ species are longer than that on the octahedrally-coordinated $Ti^{4+}$ species for bulk titania [7]. Therefore, the formation of $N_2O$ and $NO_2$ can be inhibited.

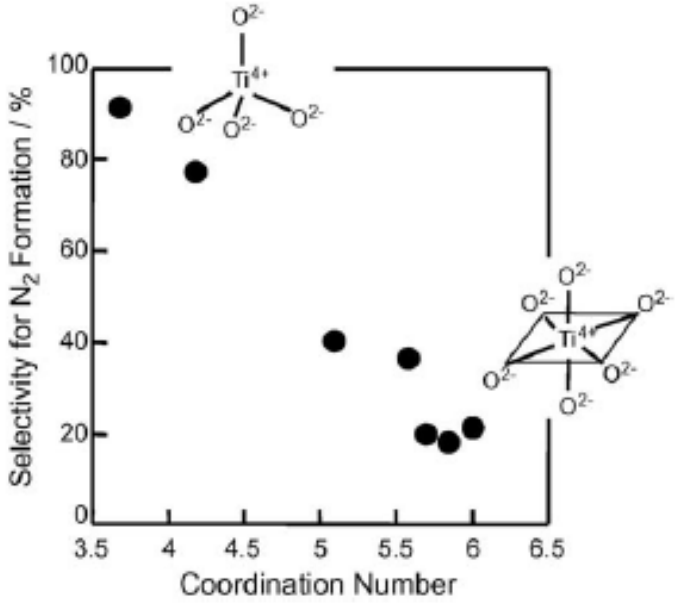


**Figure 19.** Relationship between the coordination number of $Ti^{4+}$ species and the selectivity for $N_2$ formation in the photocatalytic decomposition of NO on various titania photocatalysts (Copyright notice © Elsevier, 2017 [49])

### 1.5.2. PHOTO-SELECTIVE CATALYTIC REDUCTION

Photo-SCR which does not require high temperatures to operate is a very attractive approach for $NO_x$ abatement. In this process, the reduction of $NO_x$ occurs in the presence of a reducing agent, such as $NH_3$ or hydrocarbons, under light irradiation. In most of the cases, hydrocarbons or carbon monoxide is chosen as the reducing agents, because excess $NH_3$ release can lead to unwanted secondary emissions. However, utilization of photo-SCR with hydrocarbons or CO is not straightforward either. For instance, oxidation of hydrocarbons into $CO_2$ is one of the major challenges which must be considered. Also, undesired $N_2O$ may appear as a by-product (tough its photocatalytic reduction could be possible) [7].

The mechanisms of photo-SCR are still unclear and under investigation. In the presence of CO, the photocatalytic mechanism proposed mainly consists of photocatalytic decomposition of NO which is discussed in the previous section. Therefore, the main product of the decomposition mechanism, $N_2O$, can be transformed into $N_2$ and $CO_2$ in the presence of CO [47]. The main reactions occurring on commercial titania, Degussa P25, are [47]:

$$O_{(ads)} + CO_{(ads)} \rightarrow CO_{2_{(g)}} \quad (43)$$

$$2NO_{(ads)} + CO_{(ads)} \rightarrow N_2O_{(ads)} + CO_{2_{(ads)}} \quad (44)$$

$$N_2O_{(ads)} + CO_{(ads)} \rightarrow N_{2_{(g)}} + CO_{2_{(ads)}} \quad (45)$$

$$N_{(ads)} + CO \rightarrow NCO_{(ads)} \quad (46)$$

In the presence of propane, Su and Wu tested photo-SCR of NO on Pd-loaded $TiO_2$ [51]. It was found that Pd improved the adsorption of propane molecules which led to an increase in NO conversion and $N_2O$ was not observed in the effluent. Stoichiometric mass balance reactions proposed for this process are [51]:

$$10NO + C_3H_8 \rightarrow 5N_2 + 3CO_2 + 4H_2O \quad (47)$$

$$12NO + C_3H_8 \rightarrow 2N_2O + 3CO_2 + 4H_2O + 4N_2 \quad (48)$$

In addition to these overall reactions, other side products and reaction mechanisms were also reported. For instance, Matsuoka *et al.* observed acetaldehyde ($CH_3CHO$) formation on vanadium silicate-1 surface in the presence of propane and under light irradiation [52]. In a similar system studied by Anpo *et al.*, acetone ($CH_3COCH_3$) was detected as a by-product under UV irradiation [49]. Moreover, photo-reactions carried out on the $C_4H_8$-$NO_2$-Air system revealed that the side products of this process contained cyano products (*e.g.* HCN and $CH_3CN$) [7]. In the reaction mechanisms summarized in equations (*43-48*), one of the major shortcomings is the disregarding the water and oxygen presence. Therefore, the influence of such oxidizing compounds needs to be investigated in depth.

When ammonia ($NH_3$) is introduced as a reducing agent, the overall reaction of photo-SCR resemble that of the thermal SCR shown in equation (*49*) [7]. The mechanism of photo-SCR in the presence of ammonia over titania surface is presented in Figure 20 [53].

$$4NO + 4NH_3 + O_2 \rightarrow 6H_2O + 4N_2 \qquad (49)$$

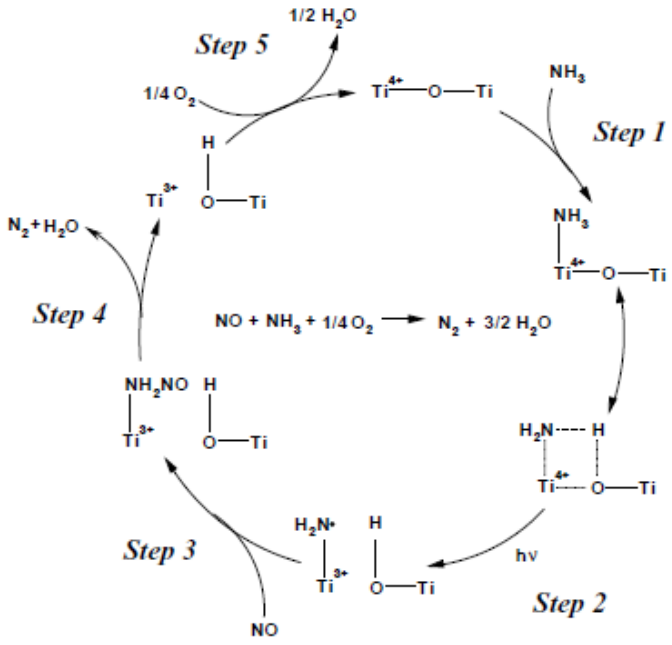


**Figure 20.** Schematic representation of the Photo-SCR reaction mechanism on the titania surface in the presence of $NH_3$ (Copyright notice © Elsevier, 2017 [53])

### 1.5.3. PHOTO-OXIDATION

In photo-oxidation systems, the aim is converting $NO_x$ molecules into surface nitrates or nitrites. This transformation is possible in the presence of oxidizing agents such as $H_2O$ and $O_2$. During photo-oxidation, the photocatalyst surface eventually gets saturated with $HNO_3$ and requires frequent catalyst regeneration. The NO photo-oxidation mechanism on titania-based photocatalysts can be summarized via the following reactions [7], [54], [55]:

Charge carrier generation and electron-hole trapping:

$$TiO_2 + h\nu \rightarrow e^- + h^+ \quad (50)$$

$$h^+ + H_2O_{(ads)} \rightarrow HO^\bullet_{(ads)} + H^+ \quad (51)$$

$$h^+ + HO^-_{(ads)} \rightarrow HO^\bullet_{(ads)} \quad (52)$$

$$e^- + O_{2(ads)} \rightarrow {O_2}^-_{(ads)} \quad (53)$$

Oxidation reactions via hydroxyl radicals and oxygen radicals:

$$NO + HO^\bullet_{(ads)} \rightarrow HNO_2 \quad (54)$$

$$HNO_2 + HO^\bullet_{(ads)} \rightarrow NO_2 + H_2O \quad (55)$$

$$NO_2 + HO^\bullet_{(ads)} \rightarrow HNO_3 \quad (56)$$

$$NO + {O_2}^-_{(ads)} \rightarrow {NO_3}^- \quad (57)$$

Reaction of $NO_2$ with surface hydroxyl groups:

$$3NO_2 + 2OH^- \rightarrow 2{NO_3}^- + NO + H_2O \quad (58)$$

As it is seen from equations (*51*) and (*52*), hydroxyl radicals can be formed via oxidation of surface hydroxide groups or water molecules. When oxygen is present in the reaction environment, produced electrons are rapidly quenched by oxygen [55]. Superoxide anions are less effective than hydroxyl radicals in initiating oxidation reactions [54]. Thus, the photo-oxidation of NO depends mainly on the presence of water molecules. The reaction mechanisms

above also indicate the surface saturation with nitrate formation. Therefore, as Dalton *et al*. suggested, $DeNO_x$ cycle should be closed by $HNO_3$ removal *via* water treatment [56].

Wu and Cheng discussed NO adsorption and photo-oxidation on titania surface using *in-situ* FTIR spectroscopy [57]. Based on adsorption mechanism they proposed (Figure 21), NO initially attacks on free surface hydroxyl groups and is subsequently oxidized to monodentate nitrite by surface active oxygen. Then oxygen vacancies and surface peroxo species transforms monodentate nitrite into bidentate nitrite and hydroperoxo. Based on their photo-oxidation mechanism (Figure 22), holes generated due to irradiation are trapped by surface peroxo species, which in turn are transformed to superoxo species. These superoxo species are extremely reactive with very short lifetime. If they do not react with bidentate nitrite to form monodentate/bidentate nitrate, they are photo-oxidized to oxygen molecules, leaving oxygen vacancies [57].

To achieve photo-oxidation of NO effectively, the maintenance of process parameters at optimum levels is important. Some of these parameters are light intensity, light wavelength, residence time of $NO_x$ in the reactor, humidity and catalyst type. If these parameters are not optimized, $NO_2$ formed in the oxidation steps can easily be released from the surface [7]. For instance; as $NO_2$ adsorption depends on surface acidity, lower surface acidity can enhance $NO_2$ adsorption and conversion [55].

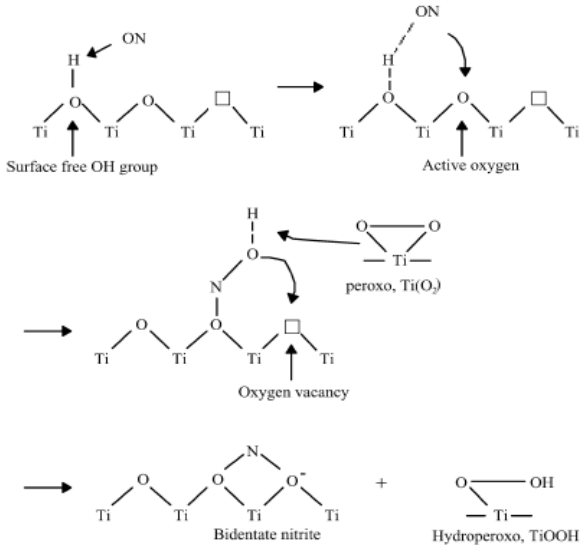


**Figure 21.** A possible mechanism of NO adsorption on titania (Copyright notice © Elsevier, 2017 [57])

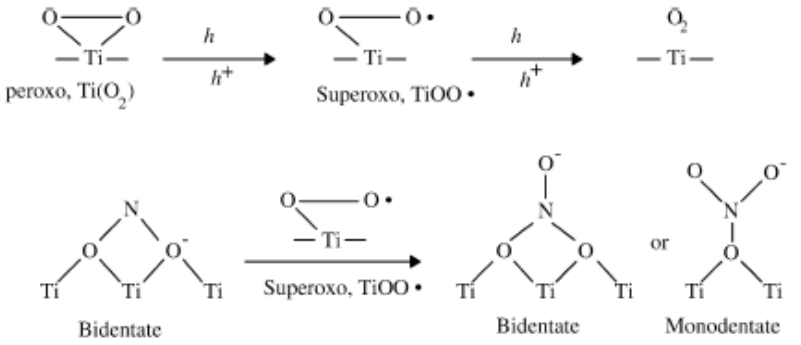


**Figure 22.** A possible mechanism of NO oxidation on titania (Copyright notice © Elsevier, 2017 [57])

## 1.6.AIM OF THE CURRENT STUDY

The starting point of this study was previous research conducted by former member of Ozensoy Research Group, Asli Melike Soylu [34], [58], [59]. In this work, (P2) titania-alumina based binary mixed oxides were synthesized by a sol-gel co-precipitation method at different titania/alumina mole ratios and at various calcination temperatures. These materials were tested for photocatalytic $NO_x$ oxidation-storage under UV light irradiation. The results obtained were compared with benchmark $TiO_2$ photocatalyst, Degussa P25. To analyze the performance of materials, two photonic efficiency parameters (equations 59 and 60) were used. In this process, the presence of oxygen, water and UV light induce photocatalytic oxidation of NO molecules on the surface of the material and some of the gaseous oxidation products can be captured by the adsorption-sites as solid nitrates, while some can be released back into the atmosphere as $NO_2$. Thus; in this approach, the aim is to have high storage of $NO_x$ while releasing small amounts of $NO_2$ which is more toxic than NO. As shown in Figure 23; the best performance was obtained with (P2) 0.5 Ti/Al mixed oxide calcined at 900 $^oC$ with the parameters used thereof [58].

$$NO_x\ Storage\ Efficiency\ \% = \frac{n(NO_x\ stored)}{n(available\ photons)} \times 100 \qquad (59)$$

$$NO_2\ Generation\ Efficiency\ \% = \frac{n(NO_2\ generated)}{n(available\ photons)} \times 100 \qquad (60)$$

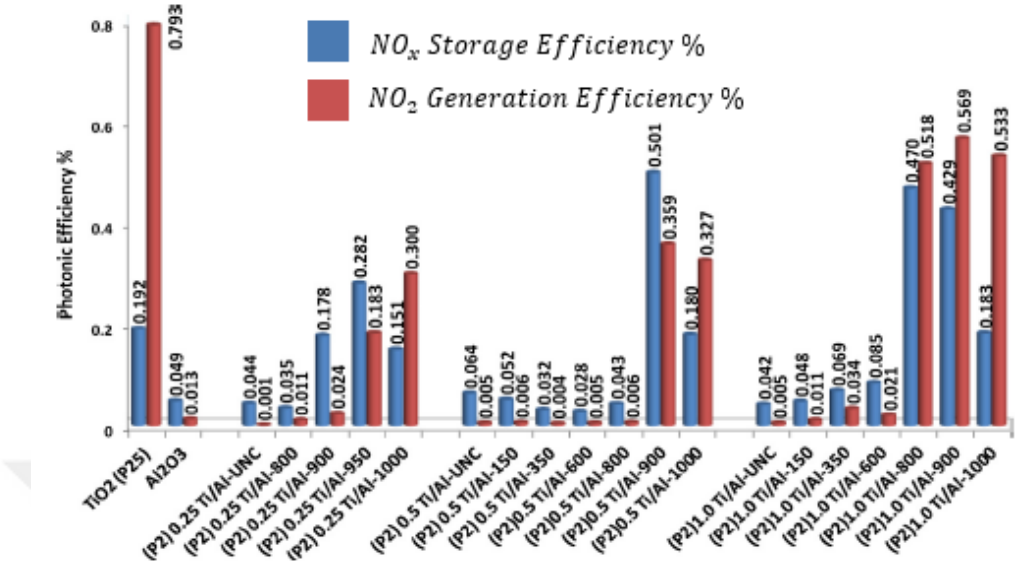


**Figure 23.** Photocatalytic $DeNO_x$ performance results for the $TiO_2/Al_2O$ binary oxide samples under UV irradiation with different molar compositions that were calcined at various temperatures in air (Copyright notice © Elsevier, 2017 [58])

In the current work, it was realized that during the performance tests there were some unstable parameters (*e.g.* humidity level, sample preparation etc.) which can affect the results significantly. Additionally, the previously used conventional performance parameters used were not clear enough to make precise conclusions. Considering these issues, in the current work, it was decided to optimize the experimental setup and the performance analysis methodology, and redo the performance tests for (P2) 0.5 Ti/Al at 800 $^oC$/900 $^oC$/1000 $^oC$. Furthermore; to increase the $NO_x$ adsorption capacity, an alkaline oxide storage component, CaO, was decided to be mixed with P2 mixed oxides physically. Moreover, Degussa P25 having superior photocatalytic activity compared to P2 samples was also mixed with commercially available γ-$Al_2O_3$ and CaO to obtain cheap and highly active materials for photo-oxidation and storage of $NO_x$.

Furthermore, prepared binary and ternary mixtures were treated under various conditions to analyze their influence on the performance results. The following parameters were investigated in the current work:

- Light Irradiation Type/wavelength (*i.e.* UV or VIS)
- Relative Humidity (*i.e.* 20%, 50%, 80%)

- Experimental Duration (*i.e.* 1 h, 5 h, 12 h)

### 1.6.1. WHY CaO AND γ-$Al_2O_3$?

$TiO_2$-based building materials are being utilized for removal of poisonous compounds in recent years. For instance, one of the most famous applications is Misericordia Church in Rome, Italy shown in Figure 24. During the construction of Misericordia Church, outside surface was coated by cement containing titania [7]. Since cement is the widely-used construction material in various applications, mixing titania with cement could be one of the best solutions to remove $NO_x$ from the atmosphere.

**Figure 24.** Misericordia Church, Rome, Italy; surface coated with cement including titania [60]

When various cements are investigated, it can be seen that the most common combination of ingredients is limestone coupled with much smaller quantities of clay as a source of silica, alumina and iron oxides. If iron and aluminum are not present in sufficient quantities in clay, bauxite and iron ore can be added. Limestone, the source of calcium carbonate is the predominant one among all raw materials. Therefore, for various cements, the most dominant component is CaO as shown in Table 7. When photocatalytic $NO_x$ oxidation-storage applications are studied, CaO usage with photocatalyst can be advantageous due to its high alkalinity and

abundance. As $NO_2$ adsorption gets better on less acidic surfaces (*i.e.* more basic surfaces), alkalinity of calcium oxide can enhance $NO_2$ adsorption (Figure 25).

**Table 7.** Typical composition of binders used in construction industry [61], [62]

| | **British White Cement** | **Tiel White Cement** | **Ordinary Portland Cement** |
|---|---|---|---|
| **CaO** | 67.70 | 67.43 | 64.1 |
| **$SiO_2$** | 22.13 | 21.56 | 22.0 |
| **$Al_2O_3$** | 4.07 | 0.77 | 5.5 |
| **$Fe_2O_3$** | 0.46 | 0.53 | 3.0 |
| **MgO** | 0.46 | 1.72 | 1.4 |
| **$Na_2O$** | 0.11 | - | - |
| **$K_2O$** | 0.12 | - | - |
| **$SO_3$** | 2.39 | 0.89 | 2.1 |
| **Loss on Ignition** | 2.64 | 6.48 | - |

Among the different transitional alumina phases, γ-$Al_2O_3$ is the most widely used support material due to its superior chemical and thermal stability, high surface area and textural acid/base properties [63], [64]. In automotive industry, γ-$Al_2O_3$ is frequently used as a support material in three-way catalytic converter systems (TWC) and $NO_x$ storage reduction systems (NSR) [64]–[68]. Although it is universally accepted that most of the $NO_2$ is stored on the basic oxides (commonly BaO or $K_2O$) supported on alumina, it is also proven that γ-$Al_2O_3$ can contribute to the total $NO_x$ storage capacity of the catalytic systems [64]–[68]. Therefore, Puralox SBa200 γ-$Al_2O_3$ provided by SASOL GmbH is chosen due to its high catalytic activity, high surface area, low attrition loss, purity and non-toxicity [69]. Some of its properties are listed in Table 8.

**Table 8.** Typical chemical and physical properties of Puralox SBa200 (SASOL GmbH) [69]

| $\gamma$-$Al_2O_3$ Amount in the Package | Pore Size Distribution | Specific Surface Area (BET) | Pore Volume |
|---|---|---|---|
| 98% | 4-10 nm | 200 $m^2/g$ | 0.35-0.50 ml/g |

Based on these facts, although it may seem that CaO is preferable in photocatalytic $NO_x$ oxidation-storage systems due to its high alkalinity, it is chemically less stable than $\gamma$-$Al_2O_3$. CaO can easily react with $H_2O$ and $CO_2$ and form $CaCO_3$ and $Ca(OH)_2$, which may change $NO_2$ adsorption mechanism [70]. Furthermore; while $Ca(NO_3)_2$ formed during absorption of $NO_2$ is water soluble, $NO_2$ absorbed on $Al_2O_3$ does not form any soluble nitrate salt. Thus, in regeneration treatments with water, there can be loss of calcium component.

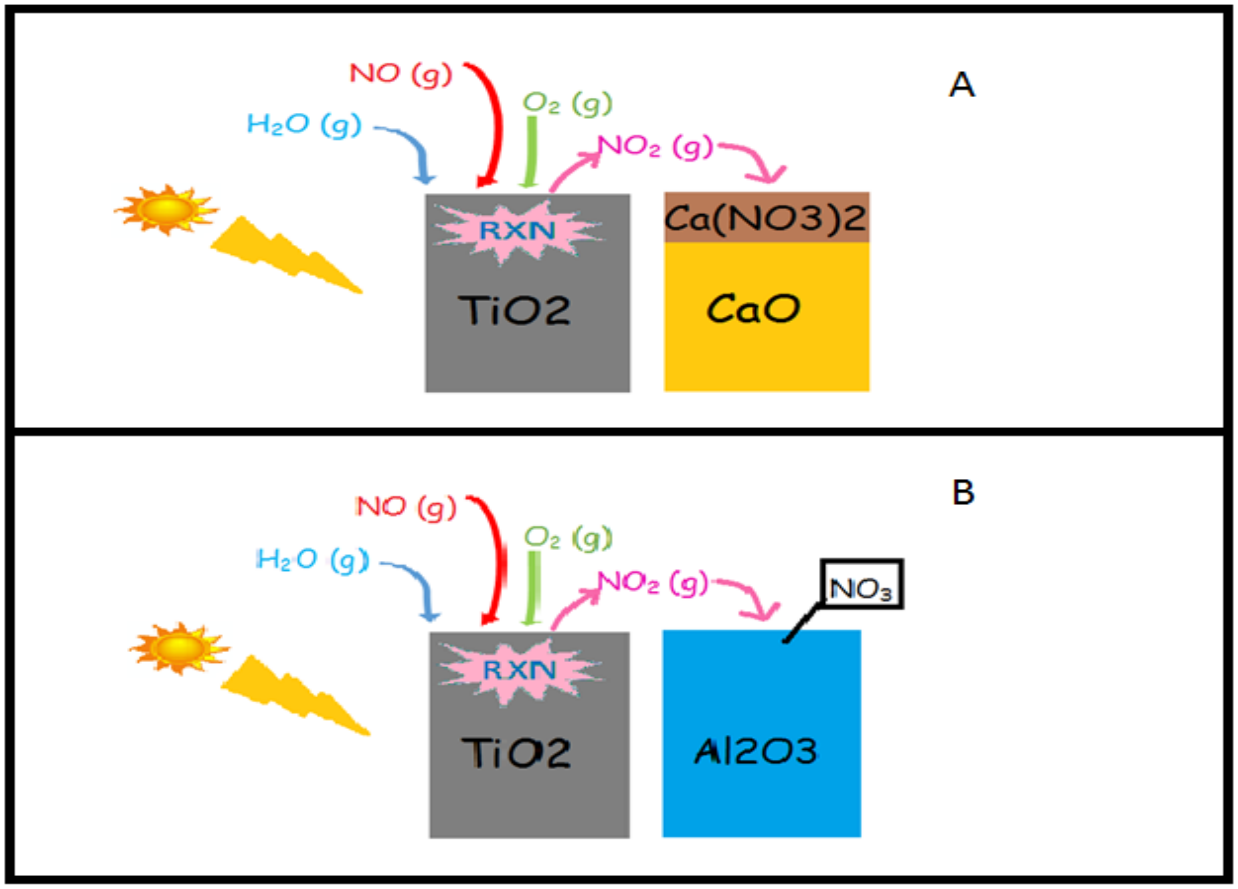


**Figure 25.** Illustration of photocatalytic $NO_x$ oxidation – storage process on titania containing (a) calcium oxide (b) aluminum oxide systems.

# Chapter 2

# Experimental Method

## 2.1.SAMPLE PREPARATION

### 2.1.1. PREPARATION OF SOL-GEL $TiO_2/Al_2O_3$ BINARY OXIDES (P2 0.5 Ti/Al) [58]

To prepare titania-alumina binary oxides having 0.5 $TiO_2/Al_2O_3$ mol ratio, 55 ml propan-2-ol (99.5 +%, Sigma Aldrich) and 1.6 ml acetylacetone (99.3 %, Fluka) were mixed with 12.4 g of aluminum sec-butoxide (97%, Sigma Aldrich) for half an hour. Then, 4 ml titanium(IV) isopropoxide (97 %, Sigma Aldrich) was added dropwise to the mixing solution for thirty minutes. All of these steps were carried out at room temperature and atmospheric pressure under continuous stirring. Next, 5 ml of 0.5 M nitric acid was added to the mixture gradually to precipitate the corresponding hydroxides. Obtained yellow slurry was left for aging under ambient conditions for 2 days. Then, the dried sample was ground for calcination steps (2 h in air at chosen temperatures).

**Table 9.** Calcination temperatures of the synthesized P2 0.5 Ti/Al

| Calcination Temperature | Sample Name |
|---|---|
| 800 $^oC$ | (P2) 0.5 Ti/Al 800 |
| 900 $^oC$ | (P2) 0.5 Ti/Al 900 |
| 1000 $^oC$ | (P2) 0.5 Ti/Al 1000 |

### 2.1.2. PREPARATION OF CaO CONTAINING P2 0.5 Ti/Al MIXED OXIDES AS A PHYSICAL MIXTURE

These samples were composed of $TiO_2/Al_2O_3$ binary oxides (P2 0.5 Ti/Al) synthesized by sol-gel method and commercially available CaO (Sigma Aldrich, Reagent Grade). P2 0.5 Ti/Al samples obtained after calcination step were ground with CaO *via* a mortar and a pestle. The obtained samples were used without further process.

**Table 10.** Compositions and calcination temperatures of CaO + P2 0.5 Ti/Al mixed oxides via physical mixing

| Calcination Temperature of P2 0.5 Ti/Al | CaO Amount in the Mixture (weight %) | Sample Name |
|---|---|---|
| 800 ºC | 1 | (P2) 0.5 Ti/Al 800 + 1 Ca 800 |
| 800 ºC | 5 | (P2) 0.5 Ti/Al 800 + 5 Ca 800 |
| 800 ºC | 10 | (P2) 0.5 Ti/Al 800 + 10 Ca 800 |
| 800 ºC | 25 | (P2) 0.5 Ti/Al 800 + 25 Ca 800 |
| 900 ºC | 1 | (P2) 0.5 Ti/Al 800 + 1 Ca 900 |
| 900 ºC | 5 | (P2) 0.5 Ti/Al 800 + 5 Ca 900 |
| 900 ºC | 10 | (P2) 0.5 Ti/Al 800 + 10 Ca 900 |
| 900 ºC | 25 | (P2) 0.5 Ti/Al 800 + 25 Ca 900 |
| 1000 ºC | 1 | (P2) 0.5 Ti/Al 800 + 1 Ca 1000 |
| 1000 ºC | 5 | (P2) 0.5 Ti/Al 800 + 5 Ca 1000 |
| 1000 ºC | 10 | (P2) 0.5 Ti/Al 800 + 10 Ca 1000 |
| 1000 ºC | 25 | (P2) 0.5 Ti/Al 800 + 25 Ca 1000 |

### 2.1.3. PREPARATION OF $CaO/TiO_2$ BINARY OXIDES AS A PHYSICAL MIXTURE (WITH DEGUSSA P25)

Commercially available benchmark photocatalyst, Degussa P25 was mixed with commercially available CaO (Sigma Aldrich, Reagent Grade) by using a mortar and a pestle. Compositions of these materials are listed in Table 10.

**Table 11.** Compositions of CaO containing Degussa P25 titania

| CaO Amount in the Mixture (weight %) | Sample Name |
|---|---|
| 1 | 0.01 CaO/P25 |
| 5 | 0.05 CaO/P25 |
| 10 | 0.10 CaO/P25 |
| 25 | 0.25 CaO/P25 |

### 2.1.4. PREPARATION OF $\gamma$-$Al_2O_3/TiO_2$ BINARY OXIDES AS A PHYSICAL MIXTURE (WITH DEGUSSA P25)

Commercially available benchmark photocatalyst, Degussa P25 was mixed with commercially available $\gamma$-$Al_2O_3$ (PURALOX, 200 $m^2/g$, SASOL GmbH) by using a mortar and a pestle. Compositions of these materials are listed in Table 12.

**Table 12.** Compositions of $\gamma$-$Al_2O_3$ containing Degussa P25 titania

| $\gamma$-$Al_2O_3$ Amount in the Mixture (weight %) | $TiO_2/Al_2O_3$ Mol Ratio | Sample Name |
|---|---|---|
| 10 | 11.49 | 0.10 $\gamma$-$Al_2O_3$/P25 |
| 30 | 2.98 | 0.30 $\gamma$-$Al_2O_3$/P25 |
| 50 | 1.28 | 0.50 $\gamma$-$Al_2O_3$/P25 |
| 70 | 0.55 | 0.70 $\gamma$-$Al_2O_3$/P25 |
| 90 | 0.14 | 0.90 $\gamma$-$Al_2O_3$/P25 |

### 2.1.5. PREPARATION OF CaO CONTAINING γ-$Al_2O_3$/$TiO_2$ TERNARY MIXED OXIDES AS A PHYSICAL MIXTURE (WITH DEGUSSA P25)

70% γ-$Al_2O_3$ (PURALOX, 200 $m^2$/g, SASOL GmbH) containing Degussa P25 $TiO_2$ was mixed with CaO (Sigma Aldrich) by using a mortar and a pestle. Compositions of these materials are listed in Table 13.

**Table 13.** Compositions of CaO containing γ-$Al_2O_3$/$TiO_2$ mixed oxides

| **γ-$Al_2O_3$/$TiO_2$ Binary Oxides** | **CaO Amount in the Mixture (weight %)** | **γ-$Al_2O_3$ Amount in the Mixture (weight %)** | **$TiO_2$ Amount in the Mixture (weight %)** | **Sample Name** |
|---|---|---|---|---|
| 0.70 Al/Ti | 1 | 69.3 | 29.7 | 0.70 γ-$Al_2O_3$/P25 + 1 CaO |
| 0.70 Al/Ti | 5 | 66.5 | 28.5 | 0.70 γ-$Al_2O_3$/P25 + 5 CaO |
| 0.70 Al/Ti | 10 | 63.0 | 27.0 | 0.70 γ-$Al_2O_3$/P25 + 10 CaO |
| 0.70 Al/Ti | 25 | 52.5 | 22.5 | 0.70 γ-$Al_2O_3$/P25 + 25 CaO |

### 2.1.6. HIGH PURITY RUTILE SYNTHESIS

Commercially available anatase dominant titanium dioxide (Sigma, ≥ 99%) was also tested in photocatalytic performance experiments. To obtain rutile dominant titania, this anatase dominant one was placed in a crucible with lid and then heated in muffle furnace at 1000 °C for 8 h.

## 2.2.PHOTOCATALYTIC PERFORMANCE TESTS

### 2.2.1. PHOTOCATALYTIC FLOW REACTOR SETUP

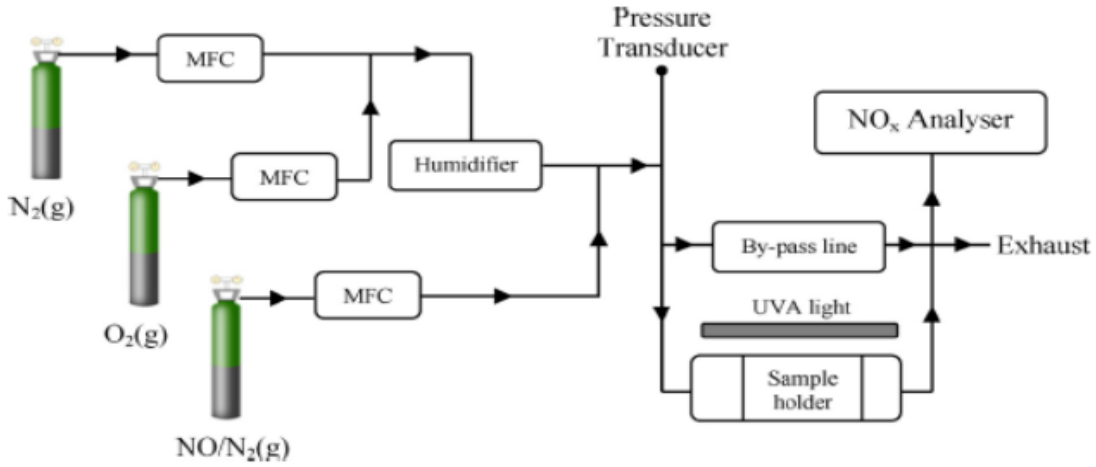


**Figure 26.** Illustration of photocatalytic $NO_x$ oxidation-storage performance test setup (Copyright notice © Elsevier, 2017 [58])

The experimental setup for photocatalytic performance test is illustrated in Figure 26. By mixing three different gases ($N_2$ -99.99%, $O_2$ -99.00%, NO - 100 ppm balanced with $N_2$) via mass flow controllers, 1 L/min gas flow with *ca.* 1 ppm NO concentration is obtained. This gas mixture is fed through the reactor where the sample holder is placed. The sample holders used in this study are designed to hold 950 mg powder material (Figure 27). At the top of the reactor, the light source is placed for irradiation during the experiments. In this study, two different light sources were used; UV irradiation: 8W UVA lamp (F8W/T5/BL350, Sylvania/Germany) – Visible irradiation: Osram 35 W high intensity discharge lamp (metal halide lamp with ceramic burner, HCI-TC 35 W/942 NDL PB 400–700 nm range) with UV filter. The outlet of the reactor is connected to the chemiluminescence ambient $NO_x$ analyzer, Horiba Apna-370, where the online concentration data can be monitored and recorded as shown in Figure 28. To humidify the gas mixture, nitrogen-oxygen gas mixture is fed through the tube side of the hollow membrane shown in Figure 29. Through the shell side of the hollow membrane, water with controlled temperature was circulating by using a pump-chiller system. Therefore, adjusting the

temperature of water in the shell side allowed controlling the humidity level of the gas mixture. Humidity level of the gas mixture was measured before/after experiments with a Hanna HI 9565 humidity analyzer at the sample position in the photocatalytic flow reactor. Additionally, the photon flux (µmol/($m^2$sec)) or the photon power density were measured with a photo-radiometer (DeltaOhm HD2302.0) at the sample position after performance tests. Parameters for the performance tests are listed in Table 14.

**Table 14.** Experimental parameters and their corresponding values used in the current photocatalytic tests

| | |
|---|---|
| **$N_2$ Flow (SLM) Set Value on MFC** | 0.782 SLM |
| **$O_2$ Flow (SLM) Set Value on MFC** | 0.208 SLM |
| **100 ppm NO (balanced with $N_2$) Flow (SLM) Set Value on MFC** | 0.010 SLM |
| **Relative Humidity of the Gas Mixture in the Reactor** | ~50 % |
| **Temperature of the Gas Mixture in the Reactor** | 21-25 $^oC$ |
| **Visible Light Photon Flux (400-700 nm)** | 450-500 µmol/($m^2$sec) |
| **UV Light Photon Power Density (315-400 nm)** | 7.75-8.25 W/$m^2$ |
| **Experimental Duration (Light Irradiation)** | 1 hour |
| **UV Irradiation Treatment Before Experiment** | 18 hours |

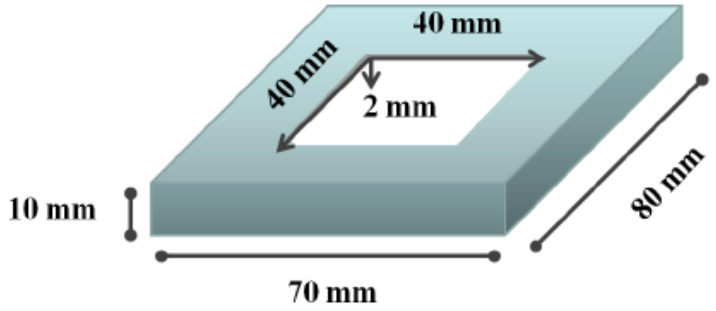


**Figure 27.** Illustration of the sample holders designed for photocatalytic performance tests [34]

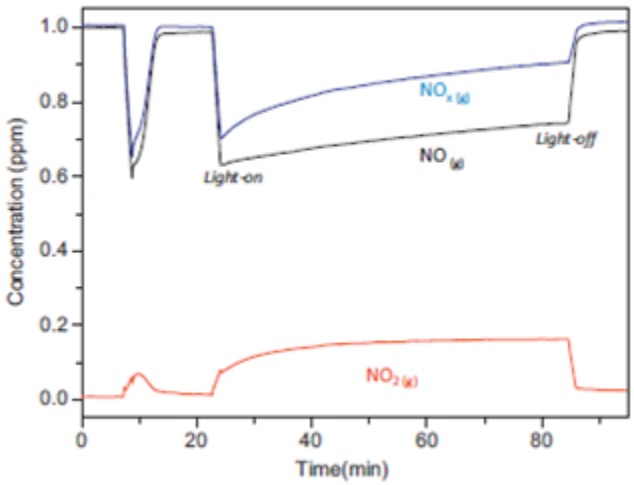


**Figure 28.** Example of a typical recorded data during the photocatalytic performance test (Copyright notice © Elsevier, 2017 [58])


**Figure 29.** PermSelect silicone fiber membrane module used in the humidifier unit [71]

### 2.2.2. PERFORMANCE ANALYSIS PARAMETERS

To analyze and compare the performances of the materials, three parameters were defined. The first one is "NO CONVERSION%" as shown in equation (*61*). In the current photocatalytic tests, there are two main outcomes, $NO_2$ release and surface nitrate-nitrite storage; thus, NO CONVERSION% shows the total oxidation activity of the material. Therefore; achieving high NO conversion values is one of the desirable outcomes for photocatalytic oxidation processes.

$$\text{NO CONVERSION\%} = \frac{\int([NO]_{in}-[NO]_{out})dt}{\int[NO]_{in}dt}\times 100 \qquad (61)$$

The second term used is "SELECTIVITY%" as shown in equation (*62)*. This term represents the percent of NO oxidation products converted into $NO_x$ species (*i.e.* NO and $NO_2$) stored on the surface of the catalyst in solid state. Therefore; achieving high value of selectivity is essential in this study, because $NO_2$ is a much more toxic pollutant than NO.

$$\text{SELECTIVITY\%} = \frac{\int([NO_x]_{in}-[NO_x]_{out})dt}{\int([NO]_{in}-[NO]_{out})dt}\times 100 \qquad (62)$$

The last performance parameter used in the current work is "DeNOx INDEX". As it is mentioned earlier, $NO_2$ is much more toxic than NO. According to OSHA (Occupational Safety and Health Administration), ACGIH (American Conference of Governmental Industrial Hygienists) and NIOSH (National Institute for Occupational Safety and Health); short term exposure limit value of NO is 25 ppm while the corresponding limit value of $NO_2$ varies from 1 to 3 ppm [72]. The photolysis of $NO_2$ ensued by reaction with $O_2$ may result in ozone ($O_3$), which is even more toxic with a limit value of 0.1 ppm [72]. Therefore, J. Z. Bloh and his colleagues developed DeNOx INDEX parameter to understand if the photocatalytic material is worth to be utilized by considering abovementioned facts. Their main assumption was that $NO_2$ contributes three times more than NO to the total toxicity of atmospheric $NO_x$. Based on these facts; if DeNOx Index has a positive value, it is good to use that material for photocatalytic $NO_x$ oxidation-storage; otherwise it should not be used. The parameter defined in equation (*63*) is a modified version of one proposed by Bloh *et al.*

$$\text{DeNOx INDEX} = \frac{\int([NO]_{in}-[NO]_{out})dt-3\int([NO_2]_{out}-[NO_2]_{in})dt}{\int[NO]_{in}dt} \quad (63)$$

## 2.3.XRD MEASUREMENTS

Crystal structures of commercially available anatase dominant titania, P25 and synthesized rutile were investigated with Rigaku Miniflex X-Ray Diffractometer, equipped with Cu Kα radiation operated at 30 kV, 15 mA and 1.54 Å. The materials pressed onto a standard-sized glass slides and scanned in the 2θ range of 10-80$^o$ with a step width 0.01$^o$ $s^{-1}$.

## 2.4.FTIR MEASUREMENTS AFTER PHOTOCATALYTIC TEST

To analyze the functional groups on the surface of the material; from each selected material, two samples were prepared. While one of them was treated under UV light for 18 hours, the other one was placed in the photocatalytic $NO_x$ oxidation-storage reactor under UV irradiation for 18 hours. From the UV activated fresh sample 50 mg material was removed and mixed with 600 mg KBr to prepare a pellet. Same procedure was followed for the one tested in photocatalytic reactor. While the pellet prepared from fresh sample was used as background in IR measurements, the one contaminated with $NO_x$ was analyzed for $NO_x$ adsorption by using the background measurement mentioned. In all measurements, a liquid nitrogen cooled MCT (Hg-Cd-Te) mid-IR detector with a resolution of 4 $cm^{-1}$ was used (Bruker Tensor 27).

# Chapter 3

# Results and Discussion

### 3.1.XRD EXPERIMENTS

### 3.1.1. DEGUSSA P25, ANATASE AND RUTILE

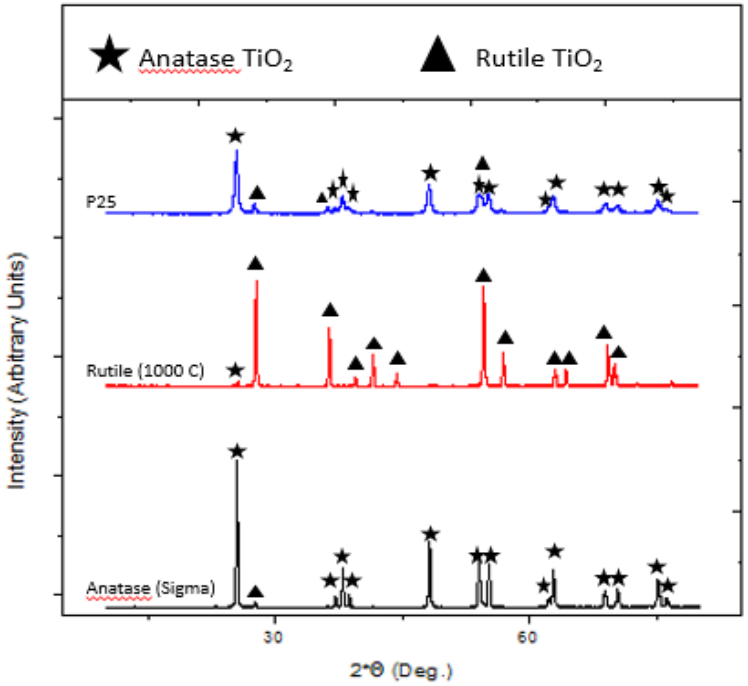


**Figure 30.** XRD patterns of Degussa P25, anatase (Sigma) and rutile (prepared by calcination of anatase)

Figure 30 presents the XRD patterns of P25, anatase, rutile used in photocatalytic performance tests. It can be interpreted from the graph that commercially available anatase and rutile obtained from this anatase are not completely pure. They contain other phases in relatively

small amounts. To calculate the mass fraction of anatase and rutile phases in these titania samples, the method developed by Spurr and Myers was utilized. Based on their method, one can calculate the mass fractions by using the intensity of the anatase {101} diffraction line at 25.18° ($I_A$) and the intensity of the rutile {110} diffraction line at 27.35° ($I_R$) as follows [73].

$$Anatase\ Mass\ Percentage = \left(\frac{I_A}{I_A + 1.26 I_R}\right) \times 100 \quad (64)$$

$$Rutile\ Mass\ Percentage = \left(\frac{1.26 I_R}{I_A + 1.26 I_R}\right) \times 100 \quad (65)$$

The obtained results are tabulated in Table 15. For P25, the calculated values are similar to the ones in the literature [41].

**Table 15.** Composition of titania samples used in photocatalytic performance tests

| Sample Name | Anatase Mass Percentage | Rutile Mass Percentage |
|---|---|---|
| Anatase (Sigma) | 94.4% | 5.6% |
| Rutile (1000 C) | 5.0% | 95.0% |
| P25 | 79.5% | 20.5% |

### 3.1.2. PURALOX SBa200 γ-$Al_2O_3$ AND CaO

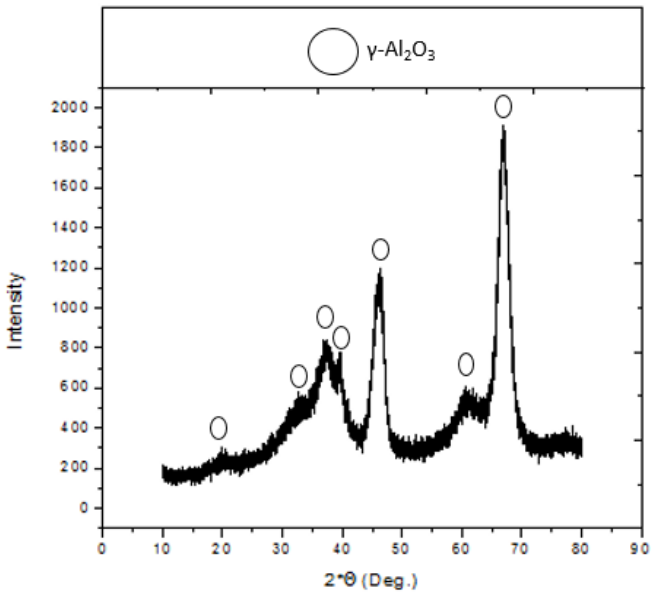


**Figure 31.** XRD pattern of Puralox SBa200 γ-$Al_2O_3$ provided by SASOL GmbH

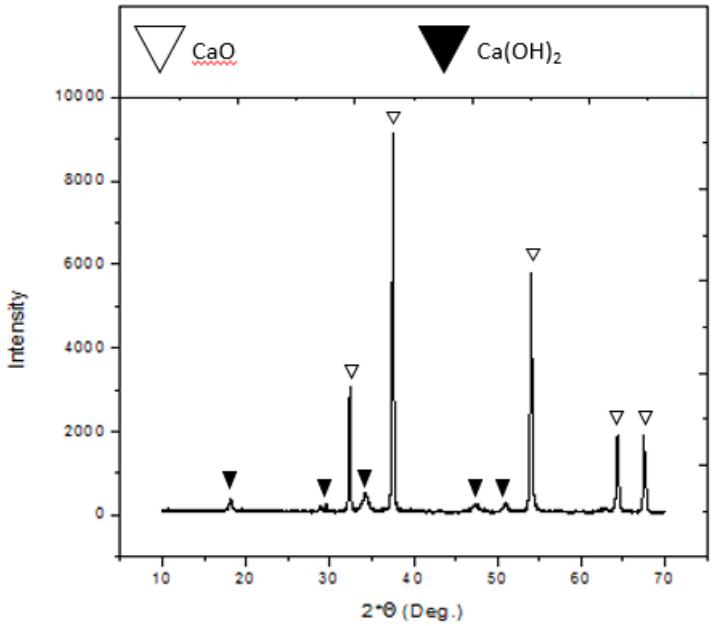


**Figure 32.** XRD pattern of CaO (Sigma Aldrich, Reagent Grade)

XRD pattern obtained for SBa200 shows the typical characteristics of γ-$Al_2O_3$. It is same with the XRD data provided by manufacturer [69]. On the other hand, XRD pattern of commercial CaO is more complex. As it is shown in the Figure 32, calcium hydroxide (slaked lime) peaks are observable. This is because of the fact that CaO can react with atmospheric moisture spontaneously [70]. Therefore, to avoid this transformation, CaO must be kept in a desiccant or a sealed box.

### 3.1.3. SOL-GEL $TiO_2/Al_2O_3$ BINARY OXIDES (P2 0.5 Ti/Al)

The XRD patterns for $TiO_2/Al_2O_3$ binary oxides prepared via sol-gel co-precipitation were compared with previous work done by Asli Melike Soylu [34], [58]. The patterns obtained are comparable with the ones obtained in the past. In Figure 33, it is seen that $TiO_2$ starts crystallizing as rutile at 900 $^oC$. As discussed by Wang *et al.*, addition of alumina can inhibit the transformation of amorphous titania into anatase polymorph by increasing the nucleation

temperature to higher point where rutile forms spontaneously [74]. At 1000 ºC, titania particles becomes fully crystalline in the form of rutile, while γ-$Al_2O_3$ is transformed into α-$Al_2O_3$ (corundum phase).

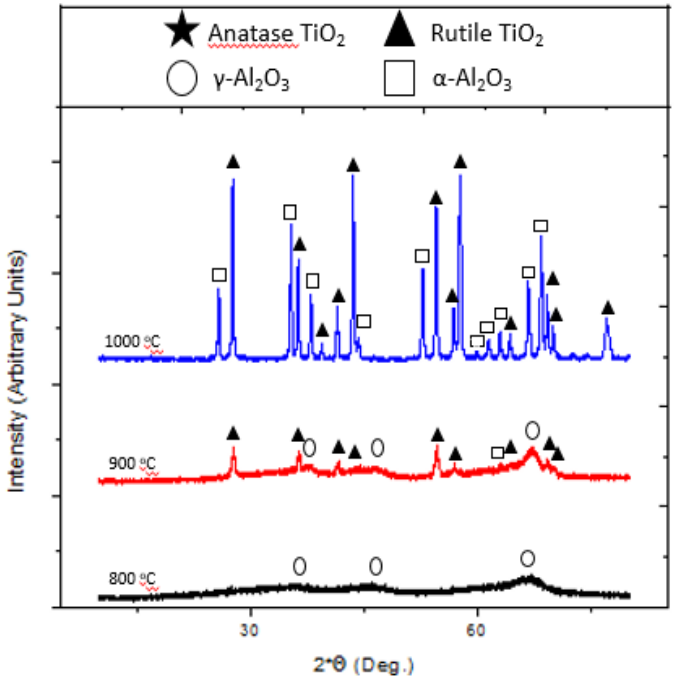


**Figure 33.** XRD patterns of $TiO_2/Al_2O_3$ binary oxides (P2 0.5 Ti/Al) prepared via sol-gel method

## 3.2.PHOTOCATALYTIC PERFORMANCE TESTS

### 3.2.1. CaO CONTAINING P2 0.5 Ti/Al MIXED OXIDES (UV IRRADIATION)

Photocatalytic $NO_x$ oxidation-storage performances of the thermally treated Ti/Al binary oxides and their mixtures with CaO were compared against Degussa P25 $TiO_2$. The analysis was made by considering “NO Conversion %” and “Selectivity %”.

As can be seen in Figure 34, P2 0.5 Ti/Al-800 ºC sample has almost negligible photocatalytic activity although it has high selectivity towards storage. At 900 ºC and 1000 ºC, where XRD patterns show rutile bands, significant NO oxidation can be observable. The

corresponding $NO_x$ conversion values are close to the activity of Degussa P25, 33%. When their selectivity values are analyzed, it can be seen that storage capacity of this binary oxide at 900 ºC becomes higher than that of the one at 1000 ºC and also that of Degussa P25. As it is shown in previous part; alumina at 900 ºC is mainly in gamma phase, while at 1000 ºC it turns into corundum polymorph. Therefore, high storage at 900 ºC can be explained with the high surface area and porosity of $\gamma$-$Al_2O_3$ compared to $\alpha$-$Al_2O_3$.

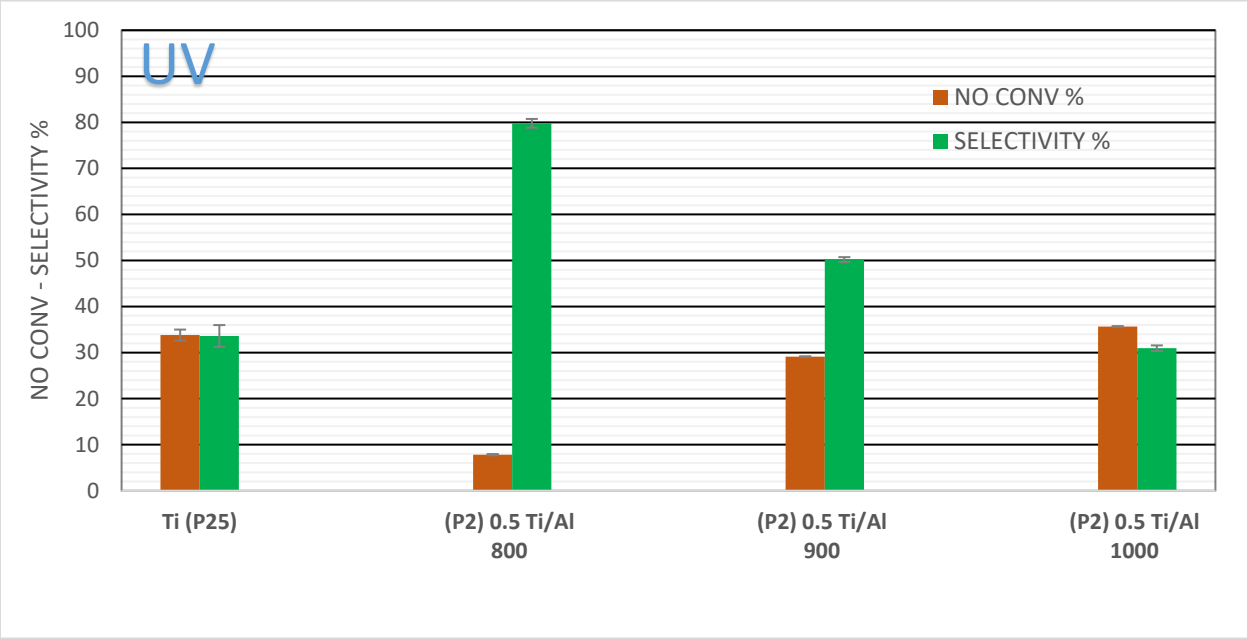


**Figure 34.** Performance plots of thermally treated P2 0.5 Ti/Al in comparison with P25 titania (UV Irradiation)

DeNOx Index values were also calculated for these set of catalysts as shown in Figure 35. As seen from the graph, positive value was obtained only for (P2) 0.5 Ti/Al-800 ºC sample. However, it should be noted that binary oxides at 800 ºC has negligible activity in terms of NO conversion. Thus, positive DeNOx Index value for this sample does not correspond to a worthwhile catalytic material. Considering these results, it was decided to mix these binary oxides synthesized via sol-gel method with CaO to improve $NO_x$ storage.

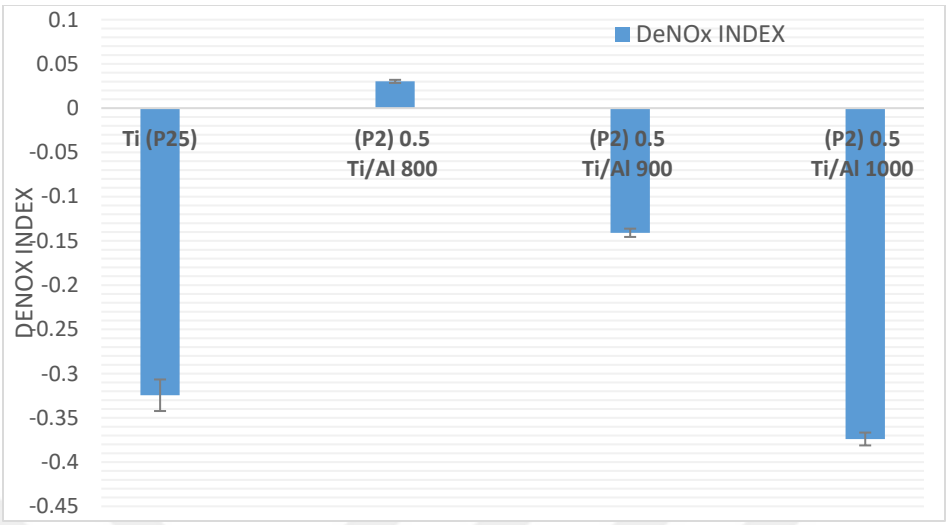


**Figure 35.** DeNOx Index Values of Thermally Treated P2 0.5 Ti/Al in Comparison with P25 titania (UV irradiation)

Figure 36 shows the enhancement in $NO_x$ storage even after 1% (wt) CaO addition to P2 0.5 Ti/Al samples, especially for the ones calcined at 900 ºC and 1000 ºC. This result is reasonable since alkaline earth oxides (*e.g.* BaO) improves $NO_x$ uptake in NSR ($NO_x$ Storage Reduction) systems of automotive emission control systems [67], [75], [76]. As CaO amount in the mixture increases, selectivity becomes higher; but between 10% and 25% there is no significant improvement in terms of storage. 2.5 times higher CaO loading in the mixture leads to only 2% increase in selectivity for 0.5 Ti/Al 900 samples and 3% for 0.5 Ti/Al 1000 samples. On the other hand; with calcium oxide addition, an unwanted decrease in oxidation activity was observed. It can be argued that the added CaO blocks the active titania surface sites which leads to a decrease in the photocatalytic oxidative capacity. Therefore, it can be argued the addition of CaO to the P2 0.5 Ti/Al 900 and P2 0.5 Ti/Al 1000 samples is not advantageous. However; for the P2 0.5 Ti/Al 900 samples, it can be seen that 5-10 wt% CaO addition leads to a reasonable sacrifice in %NO conversion while significantly improving the % selectivity and DeNOx Index. Increasing CaO loading for the P2 0.5 Ti/Al 1000 presents a more monotonic trend in terms of selectivity, where selectivity increases with increasing CaO loading. This is consistent with the sintering of the alumina support during the calcination step occurring at 1000°C where $\gamma$-$Al_2O_3$ transforms into $\alpha$-$Al_2O_3$ losing its specific surface area and porosity. In other words, on the P2 0.5 Ti/Al 900, high surface area $\gamma$-$Al_2O_3$ phase is already available for $NO_x$ storage and addition

of only 5 wt% CaO is sufficient to maximize the $NO_x$ storage selectivity. On the other hand, for the P2 0.5 Ti/Al 1000 sample, low-surface area α-$Al_2O_3$ phase reveals limited $NO_x$ storage capability and the $NO_x$ storage selectivity increases rather monotonically with the increasing amount of CaO incorporation to the system.

In conclusion, utilization of the synthesized binary oxides *directly* (*i.e.* without incorporating them with other additives) is not an effective way for photocatalytic $NO_x$ abatement. Although CaO addition improves $NO_x$ storage selectivity and $DeNO_x$ index of P2 binary oxides with respect to the commercial benchmark (Degussa P25), decrease in conversion is an important disadvantage. Thus; as the next step, Degussa P25 mixtures with CaO were investigated in an attempt to alleviate some of these disadvantages.

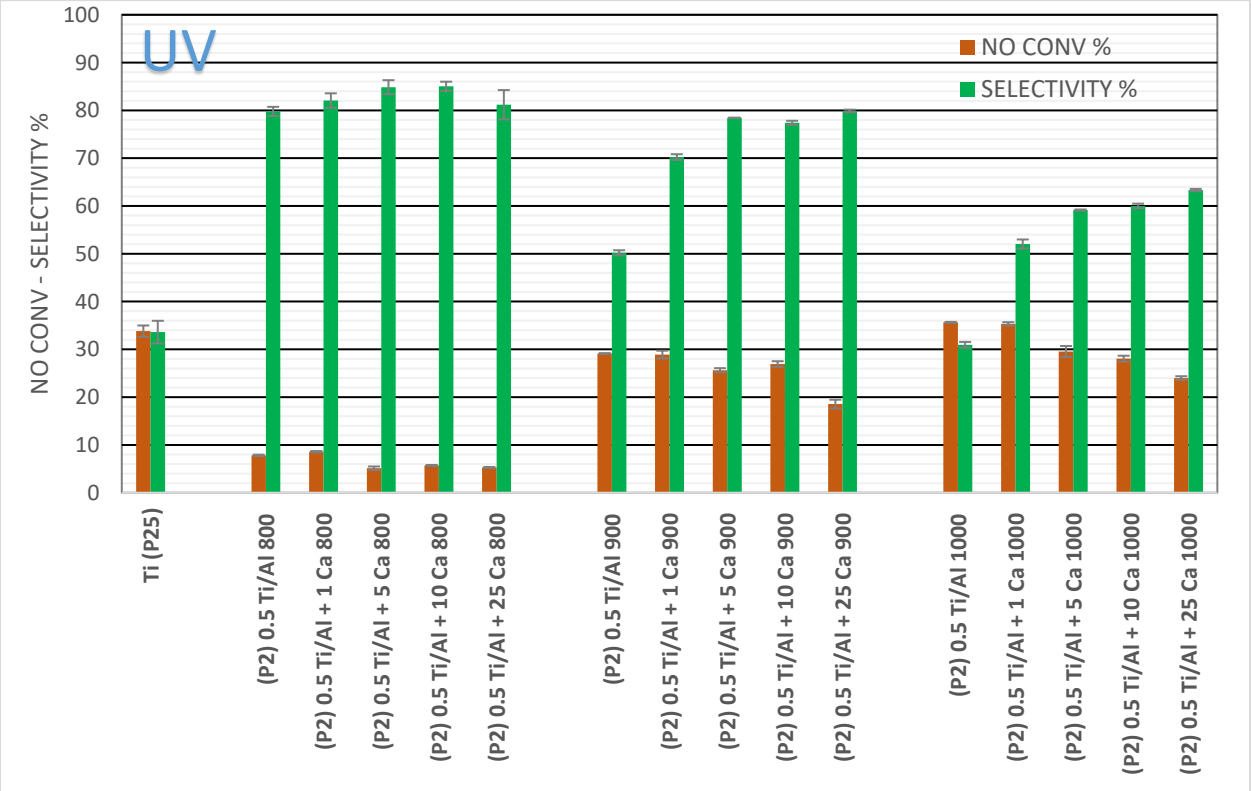


**Figure 36.** Performance plots of thermally treated 0.5 Ti/Al and their CaO containing mixtures in comparison with P25 titania (UV irradiation)

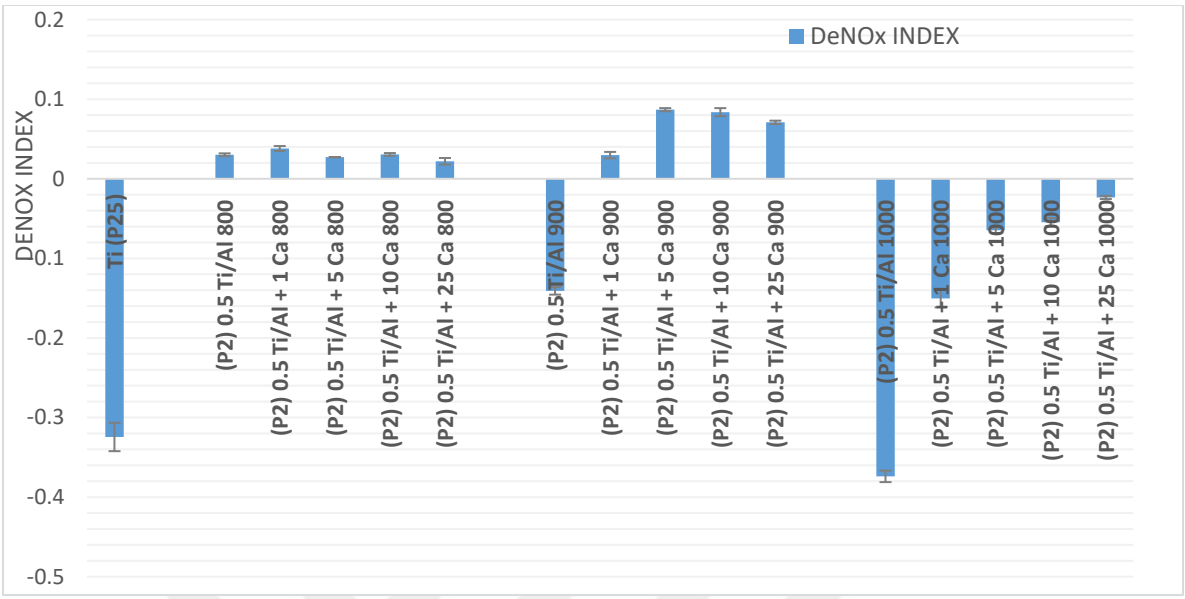


**Figure 37.** DeNOx index values of thermally treated 0.5 Ti/Al and their CaO containing mixtures in comparison with P25 titania (UV irradiation)

### 3.2.2. CaO/P25 BINARY OXIDES AS A PHYSICAL MIXTURE (UV AND VIS IRRADIATION)

Degussa P25 was mixed with CaO in various ratios and tested in the photocatalytic flow reactor. Their performances under UV irradiation are given in Figure 38. As observed for the previous case, CaO addition certainly improves the storage process. Similarly; as CaO loading increases, selectivity converges to a limit, approximately 75-80%. However, in this case CaO addition to P25 does not hinder the NO conversion activity. This can be attributed to the higher titania wt% in the CaO/P25 samples as compared to CaO + 0.5 Ti/Al samples. In other words, CaO amount is not high enough to block sufficient extent of the titania active sites that operate under UV irradiation in the case of CaO/P25 samples. Contrary to CaO + 0.5 Ti/Al samples, oxidation activity gets even better upon incorporation of CaO to P25. Further, *in-situ* spectroscopic experiments need to be carried out under photocatalytic conditions in order to shed light on this observation. However, one can speculate that increase in the conversion upon CaO addition could be attributed to the facilitated diffusion (surface transport) of $NO_x$ oxidation products from the active sites of titania towards the CaO domains, preventing the

saturation/poisoning of the active sites with the reaction products. This seems not to be the case for CaO+0.5 Ti/Al samples, where the presence of alumina domains may be hindering the facile/direct transport of $NO_x$ oxidation products from the titania active sites to CaO domains and hence leading to the saturation/poisoning of the titania active sites by the $NO_x$ oxidation products.

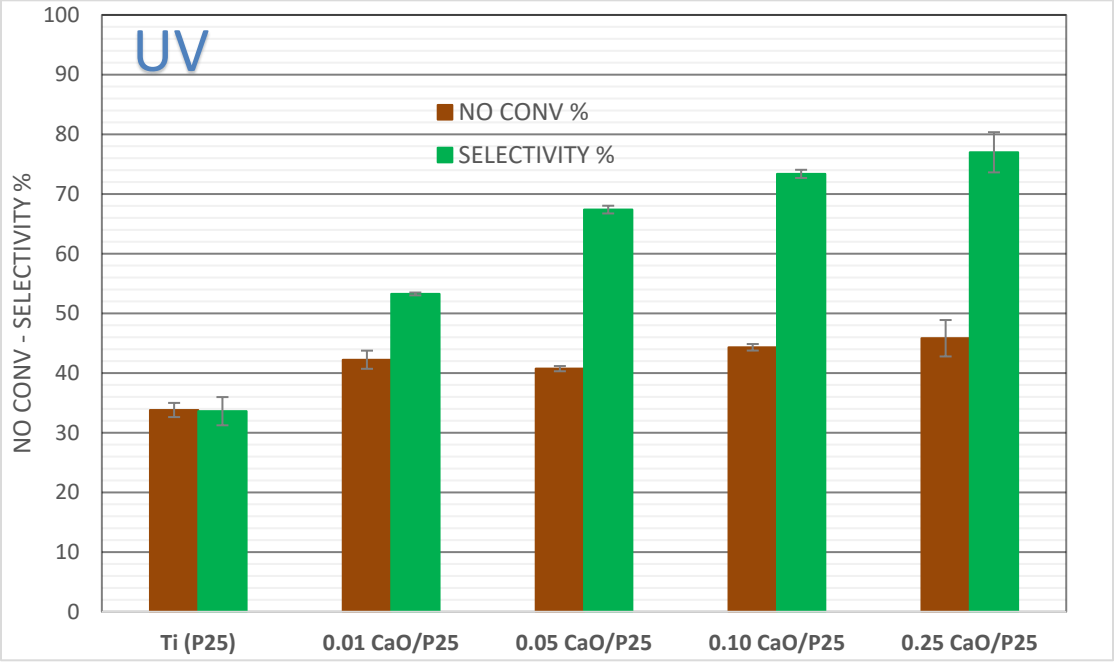


**Figure 38.** Performance plots of CaO/P25 binary oxides as a physical mixture (UV irradiation)

Moreover, CaO/P25 binary oxides samples were also tested for photocatalytic $NO_x$ storage under visible light irradiation. As revealed in Figure 39, the conversion values are close to the values obtained under UV. However, the selectivity values under visible light are significantly higher than the ones under UV irradiation. It may reach up to 90% depending on the CaO amount. This makes utilization of these materials under sun irradiation favorable since sun light has a greater VIS photon flux than that of UV photons. Another striking observation can be realized by comparing the UV *vs.* VIS performance/selectivity of P25 sample (Figure 38-39). It is apparent that although NO conversion is comparable for both cases, NO*x* storage selectivity is different. Thus, it can be argued that although initial photocatalytic NO oxidation steps may be similar for under UV and VIS irradiation (yielding similar %NO conversion), further mechanistic steps transforming this initial oxidation product into adsorbed nitrate/nitrite species

vary with the irradiation wavelength. This interesting observation may also suggest that the nature of the photocatalytic active sites on titania as well as their corresponding surface concentrations on P25 could be dissimilar for UV and VIS irradiation cases. Since the UV photon flux used in the experiments are significantly lower than that of the VIS photon flux, it can be speculated that titania active sites for UV irradiation are either greater in surface concentration with lesser "*per-site*" activity to that of VIS active sites, or they are fewer in surface concentration revealing higher "per-site" activity than that of VIS sites. Unfortunately, t*urn over frequency* (TOF) values cannot be calculated in the current work due to the lack of information regarding the nature and the surface coverage of the active sites.

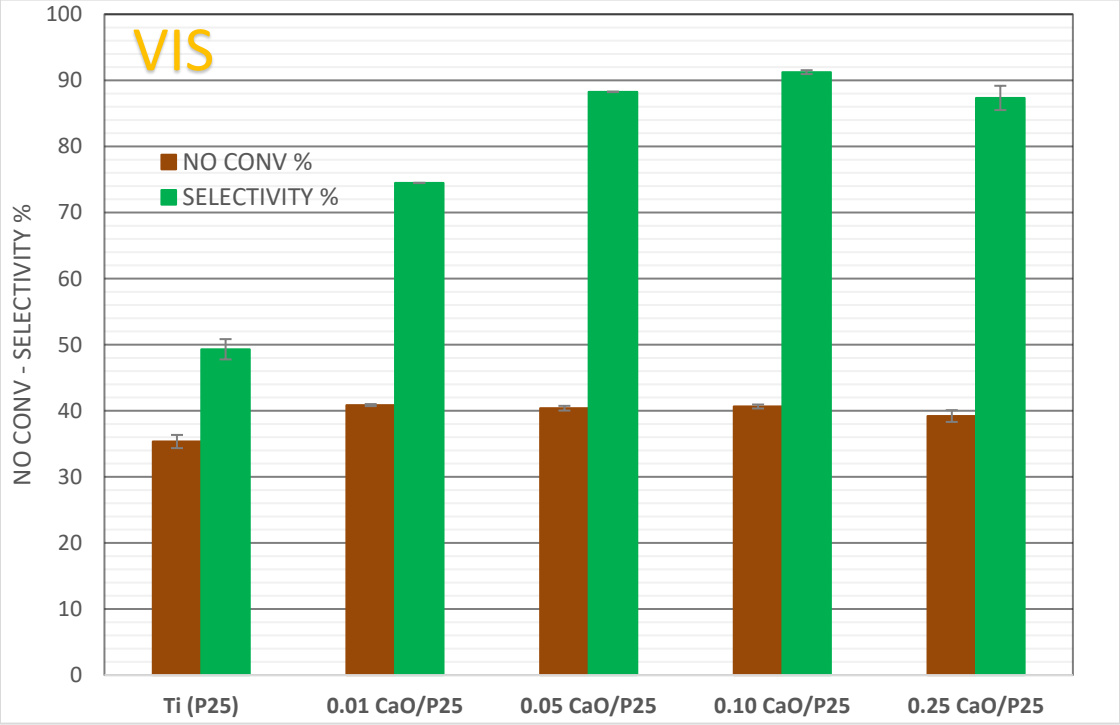


**Figure 39.** Performance plots of CaO/P25 binary oxides as a physical mixture (Visible irradiation)

Finally, DeNO*x* Index values of CaO/P25 samples were calculated for UV and VIS irradiation and presented in Figure 40. DeNOx Index values are higher under visible light, due to low $NO_2$ emissions.

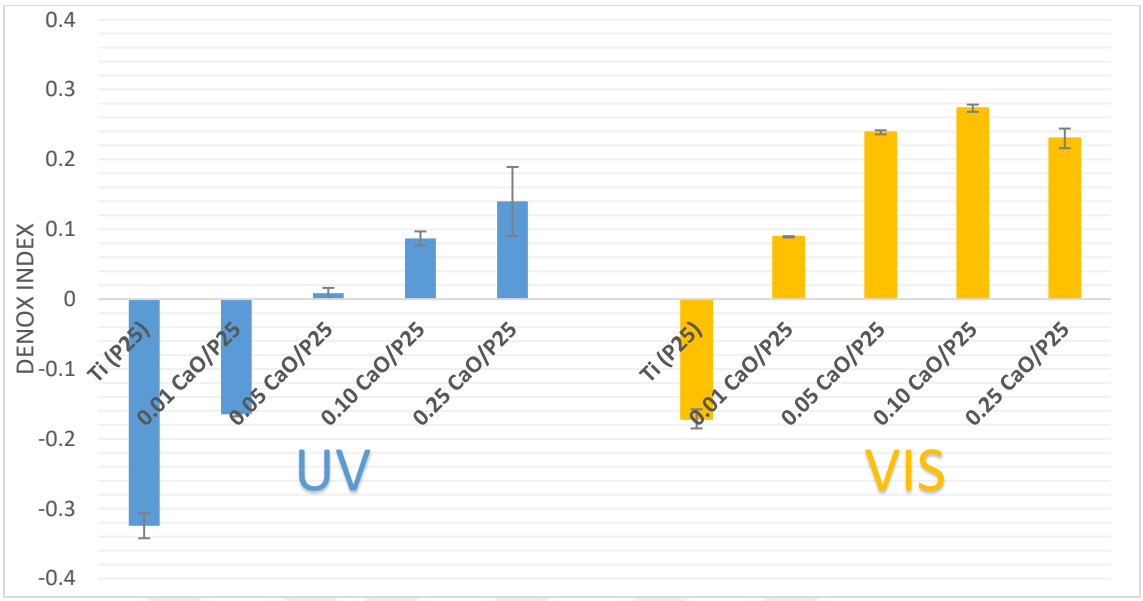


**Figure 40.** DeNOx index values of CaO/P25 binary oxides as a physical mixture

### 3.2.3. $\gamma$-$Al_2O_3$/P25 BINARY OXIDES AS A PHYSICAL MIXTURE (UV AND VIS IRRADIATION)

Apart from the sol-gel synthesized P2 Ti/Al samples, Degussa P25 was also mixed with commercially available $\gamma$-$Al_2O_3$ (SASOL Puralox SBa200) using different weight percentiles. This preparation route was chosen in order to provide a physical interface between alumina and titania domains, so that NO oxidized on titania surface can subsequently be stored on the nearby $\gamma$-$Al_2O_3$ sites.

First of all, $\gamma$-$Al_2O_3$/P25 physical mixtures were tested under UV light. Their corresponding conversion and selectivity values are shown in Figure 41. As displayed in the graph, addition of $\gamma$-$Al_2O_3$ (SBa200) certainly improves the storage capacity while enhancing the conversion slightly. The optimum composition was achieved at 70 wt% $\gamma$-$Al_2O_3$ (*i.e.* $TiO_2/Al_2O_3$ mole ratio of 0.55). Even though pure alumina gave high selectivity towards storage, it had negligible photocatalytic activity. Compared to CaO/P25 binary mixtures, $\gamma$-$Al_2O_3$/P25 samples have lower storage selectivity. While it is probable to achieve 75% selectivity on CaO/P25, the

maximum selectivity is around 65% for γ-$Al_2O_3$/P25. This shows that higher basicity of CaO is a more critical characteristic than the higher surface area of γ-$Al_2O_3$ in the P25 binary mixtures.

When the UV performances of γ-$Al_2O_3$/P25 samples (Figure 41) are compared with sol-gel synthesized P2 Ti/Al samples (Figure 34), γ-$Al_2O_3$/P25 physical mixtures are found to be superior. Note that even the γ-$Al_2O_3$/P25 physical mixture containing 90 wt% alumina (with a $TiO_2/Al_2O_3$ mole ratio of 0.14) gave far better performance than P2 0.5 Ti/Al-900 (with a $TiO_2/Al_2O_3$ mole ratio of 0.55). This shows that titania domains in P25 are intrinsically much more active than titania domains in the sol-gel catalysts. This situation can be explained with the fact that anatase is generally a better photocatalyst than rutile, and P25 has a higher amount of anatase polymorph while P2 samples mainly consist of the rutile phase.

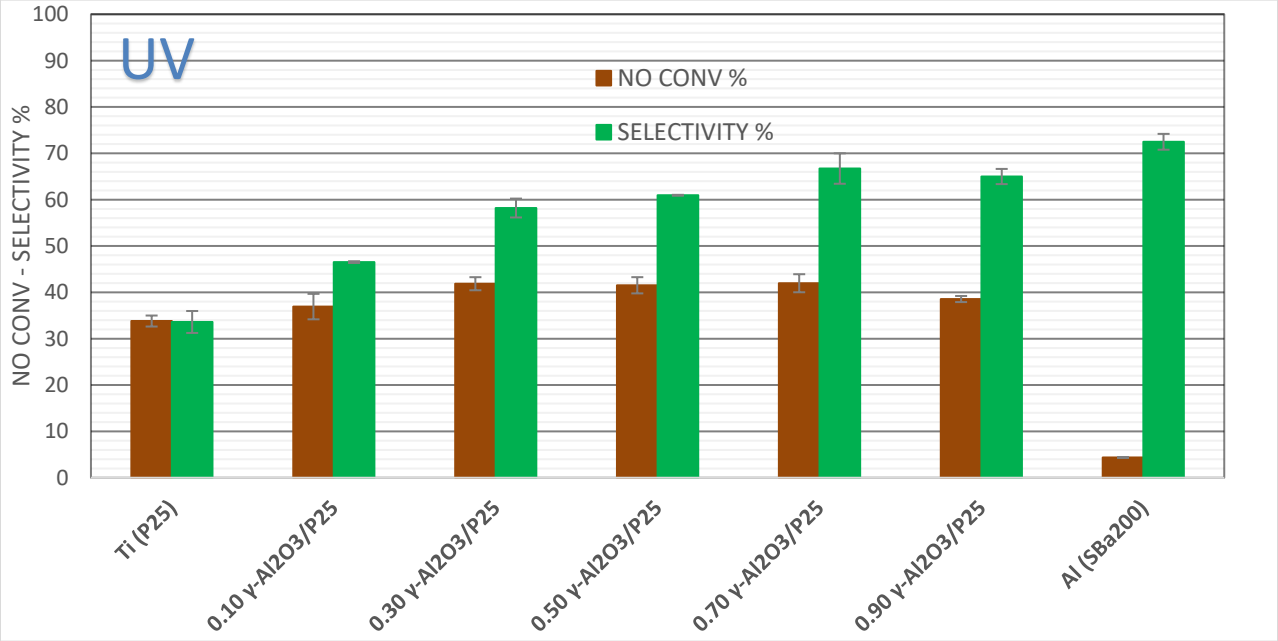


**Figure 41.** Performance plots of γ-$Al_2O_3$/P25 binary oxides as a physical mixture (UV irradiation)

In addition to UV experiments, γ-$Al_2O_3$/P25 physical mixtures were tested under visible irradiation. Their performances are shown Figure 42. Conversion values (~39%) under VIS irradiation of γ-$Al_2O_3$/P25 are very close to that of obtained in UV experiments (~41%). When selectivity trends are examined, similar trends to that of CaO/P25 samples can be observed. Particularly for the γ-$Al_2O_3$/P25 sample with an alumina loading of 70 wt%, NO*x* storage selectivity under visible irradiation may reach up to 90%, while exhibiting an NO conversion

superior to that of pure Degussa P25. This high selectivity value shows that only *ca.* 10% of oxidation products are released as $NO_2$. Thus, it can be stated that 70 wt% alumina loading yields the is the optimum $\gamma$-$Al_2O_3$/P25 composition.

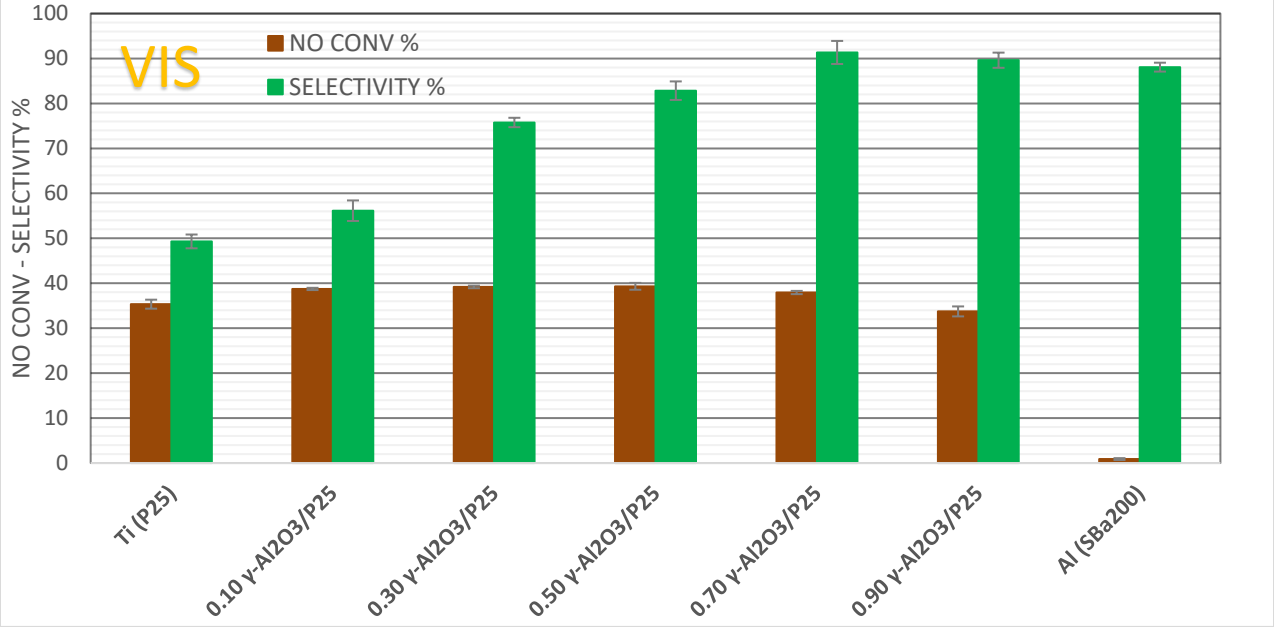


**Figure 42.** Performance plots of $\gamma$-$Al_2O_3$/P25 binary oxides as a physical mixture (Visible irradiation)

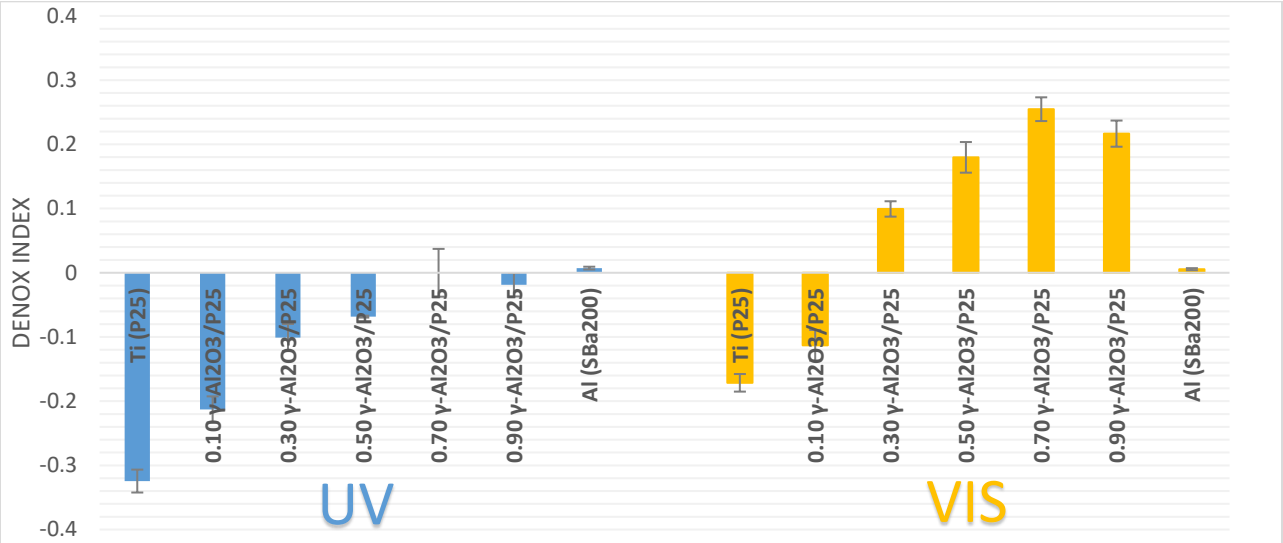


**Figure 43.** DeNOx index values of $\gamma$-$Al_2O_3$/P25 binary oxides as a physical mixture

Finally, the $DeNO_x$ Index values for γ-$Al_2O_3$/P25 were calculated and presented in Figure 43. For both types of irradiation (*i.e.* UV and VIS), the highest $DeNO_x$ index values were obtained with 70 wt% γ-$Al_2O_3$/P25 sample. Probably one of most important outcomes of the current experiments on γ-$Al_2O_3$/P25 system is the fact that extremely affordable photocatalysts can be designed for mass production to be used in construction/civil engineering sector utilizing very limited amounts of titania (which typically dictates the overall cost of the catalyst) and large quantities of financially less demanding alumina.

### 3.2.4. CaO/γ-$Al_2O_3$/P25 TERNARY MIXED OXIDES AS A PHYSICAL MIXTURE (UV and VIS IRRADIATION)

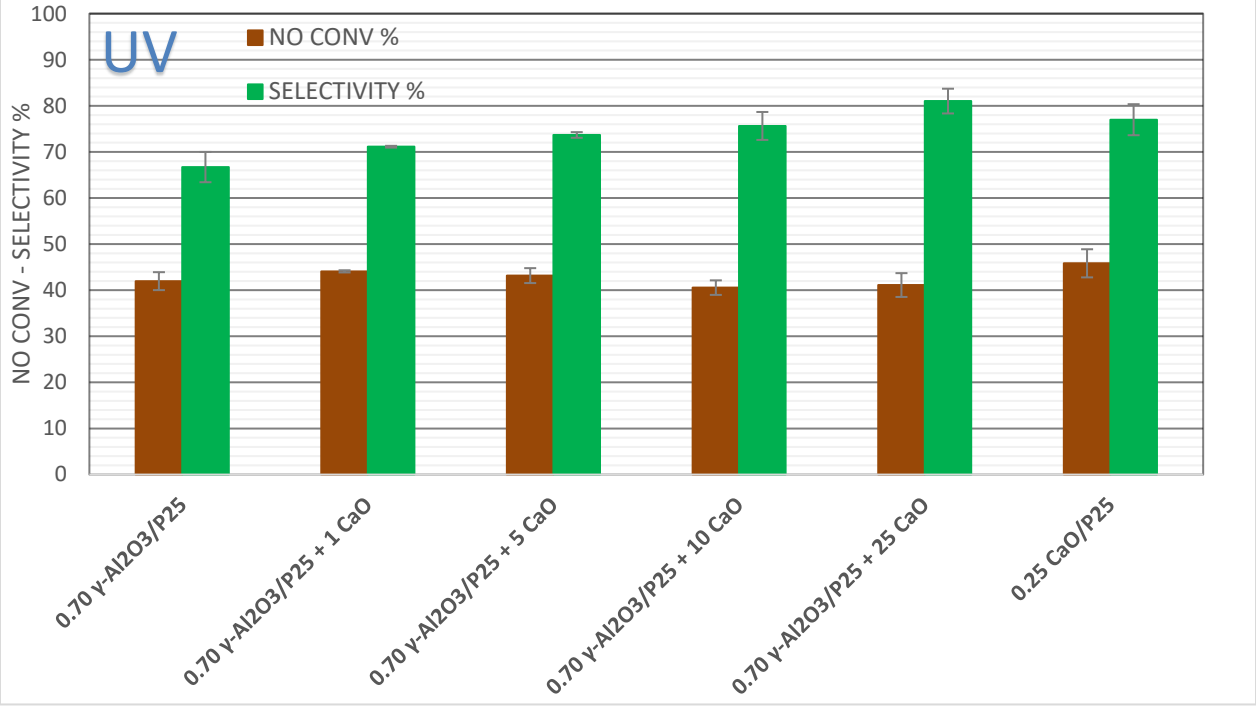


**Figure 44.** Performance plots of CaO/(70 wt% γ-$Al_2O_3$/P25) ternary mixed oxides as a physical mixture (UV irradiation)

In previous section, it was demonstrated that the optimum composition for the γ-$Al_2O_3$/P25 system included 70 wt% γ-$Al_2O_3$. Thus, this mixture was chosen to as a starting

material to prepare CaO containing ternary mixtures. Prepared CaO/γ-$Al_2O_3$/P25 ternary oxide samples were first tested under UV irradiation. As presented in Figure 44, addition of CaO to γ-$Al_2O_3$/P25 mixture improves the $NO_x$ storage selectivity. While 70 wt% γ-$Al_2O_3$/P25 sample has approximately 66% $NO_x$ storage selectivity; after CaO introduction, selectivity can go up to 80%. Besides; when 70 wt% γ-$Al_2O_3$/P25 + 25 CaO sample reveals comparable NO conversion as compared to 0.25 CaO/P25 sample. However, it should be noted that there is 22.5 wt% of $TiO_2$ in 70 wt% γ-$Al_2O_3$/P25+ 25 CaO whereas 0.25 CaO/P25 has 75 wt% $TiO_2$. Thus, 70 wt% γ-$Al_2O_3$/P25 + 25 CaO sample exhibits superior cost efficiency as compared to the 0.25 CaO/P25 catalyst.

Then, CaO/γ-$Al_2O_3$/P25 ternary oxide mixtures were photocatalytically tested under VIS light. These results are shown in Figure 45. Compared to UV case, selectivity can go above 90% in the VIS experiments. Moreover, NO conversion stays constant up to 10 wt% CaO. When CaO loading is increased to 25 wt%, a drastic decrease occurs in conversion parameter. Thus, for visible case experiments, 0.70 γ-$Al_2O_3$/P25 + 10 Ca sample can be considered as sample with optimum composition.

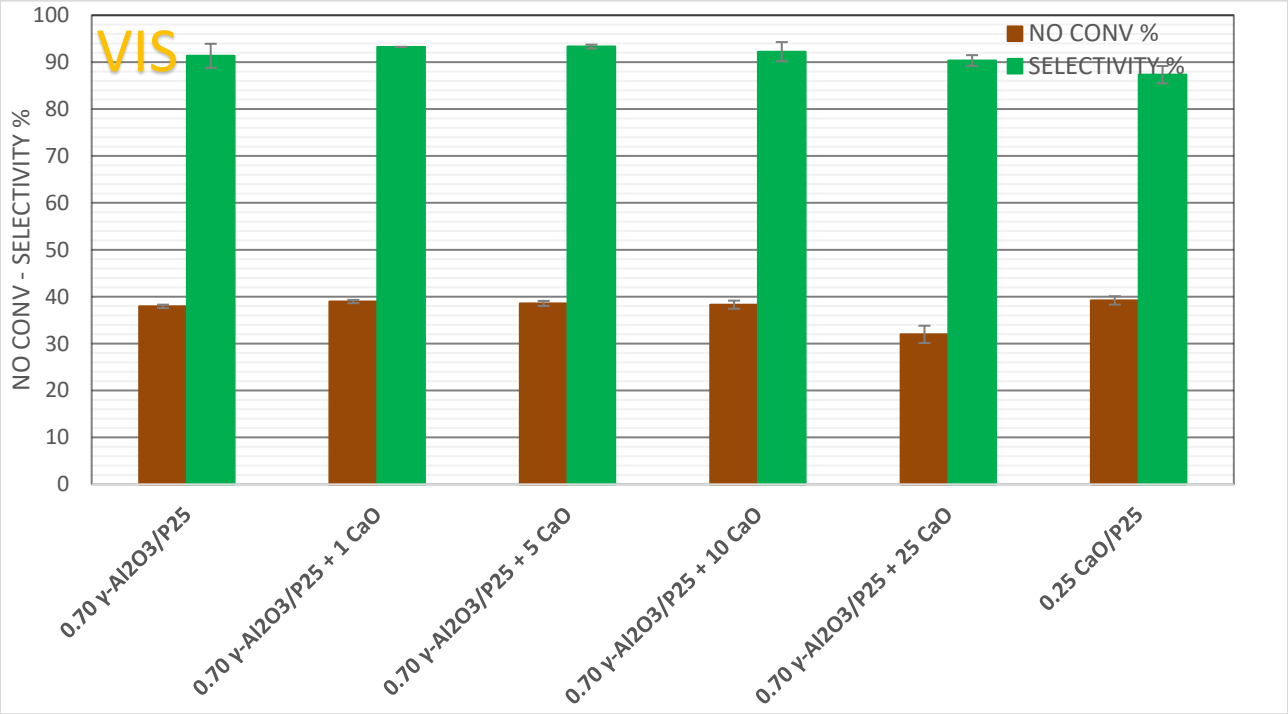


**Figure 45.** Performance plots of CaO/(70 wt% γ-$Al_2O_3$/P25) ternary mixed oxides as a physical mixture (Visible irradiation)

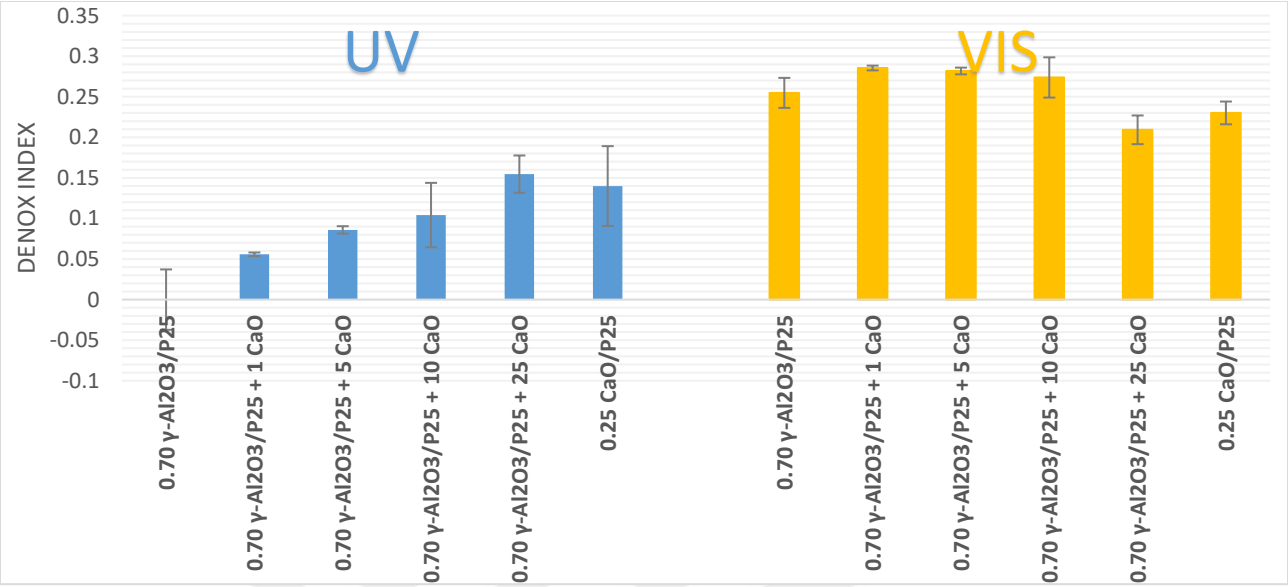


**Figure 46.** $DeNO_x$ index values of CaO containing CaO/(70 wt% γ-$Al_2O_3$/P25) ternary mixed oxides as a physical mixture

When $DeNO_x$ index values for CaO/(70 wt% γ-$Al_2O_3$/P25) samples are investigated (Figure 46), it is seen that these ternary mixtures are promising for both UV and VIS applications. Similar to the binary physical mixture cases, due to higher selectivity under VIS illumination, $DeNO_x$ index values are relatively higher in VIS experiments than that of the UV experiments.

### 3.2.5. LONG TERM PERFORMANCES

As mentioned in the experimental section; in the initial photocatalytic screening tests, UV or VIS light irradiation is applied for 1 h during photocatalytic performance tests. Therefore, all performance results presented in previous parts are based on 1 h long experiments. Considering these; following samples were tested for 5 h and 12 h:

- P25
- 0.25 CaO/P25
- 0.70 γ-$Al_2O_3$/P25

- 0.70 γ-$Al_2O_3$/P25 + 25 CaO

These samples were tested both under UV and VIS light illumination. Only the last one, (*i.e.* 0.70 γ-$Al_2O_3$/P25 + 25 CaO) could not be tested under VIS irradiation due to the instrumentational malfunctions occurred in the chemiluminescence $NO_x$ analyzer.

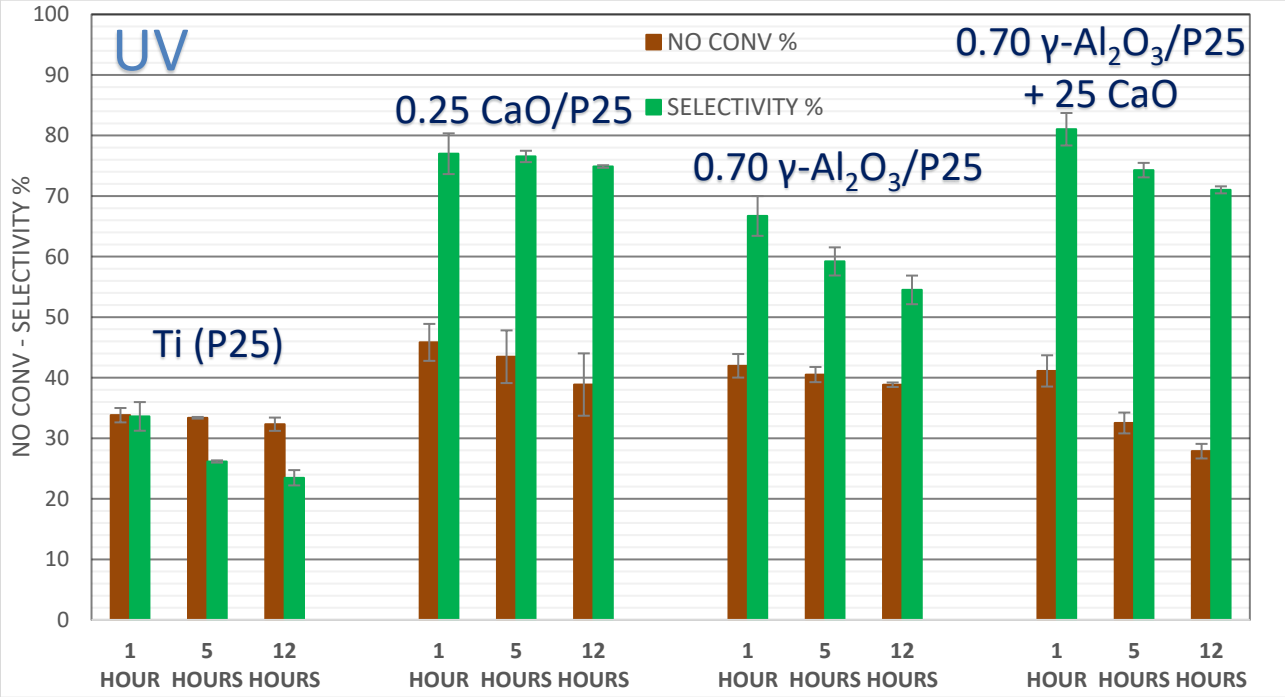


**Figure 47.** Long term photocatalytic performance results of selected samples under UV irradiation

When the data for pure P25 in Figure 47 is examined, it can be noticed that the NO conversion stays relatively invariant even after 12 h. On the other hand, $NO_x$ storage selectivity decreases with time due to the surface saturation with oxidation products. Another important point is that between 5 h and 12 h the decrease in $NO_x$ storage selectivity is negligibly small. This may indicate that selectivity of P25 converges to a steady state after an induction period of t *> 5h.*

Long term photocatalytic behavior of 0.25 CaO/P25 under UV irradiation is rather interesting. For the 0.25 CaO/P25 sample, it is not possible to claim a drastic decrease in $NO_x$ storage selectivity and the NO conversion decreases by a relatively small extent. Both parameters

stay significantly high even after 12 h. Therefore, it can be stated that deterioration and saturation of this sample is slow compared to others.

0.70 γ-$Al_2O_3$/P25 reveals similar trends to that of P25 in long term. While its overall NO conversion performance is stable, there is a considerable attenuation in the number of available storage sites decreasing the $NO_x$ storage selectivity over time. This reveals that CaO is more efficient in the storage of NO oxidation products (*e.g.* $NO_2$, nitrites, nitrates *etc.)* in long run than $TiO_2$ and $Al_2O_3$. Finally, although 0.70 γ-$Al_2O_3$/P25 + 25 CaO ternary mixture has high $NO_x$ storage selectivity after 12 h, deterioration of NO conversion is also apparent. It can be argued that due to having relatively smaller amounts of titania in the mixture, deterioration of the 0.70 γ-$Al_2O_3$/P25 + 25 CaO photocatalyst occurs faster than other samples containing higher amounts of titania.

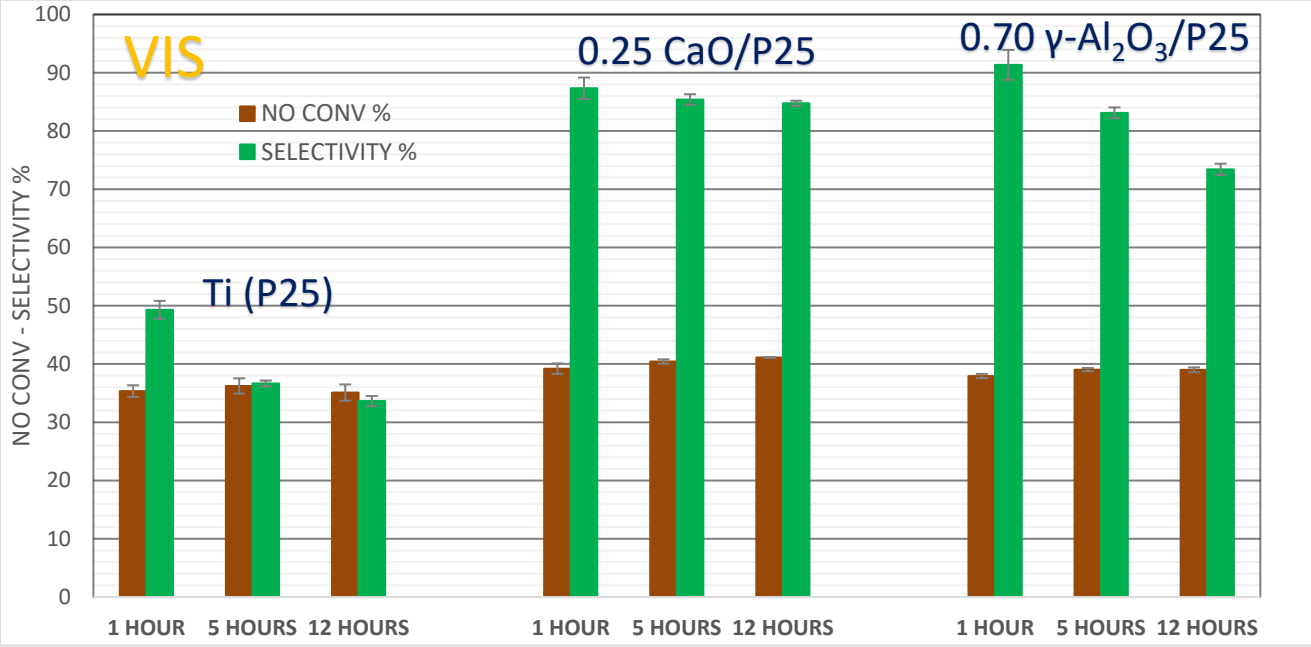


**Figure 48.** Long term performances of selected samples under visible irradiation

As expected; in the long run experiments under VIS light, $NO_x$ storage selectivity values are higher than the ones under UV light. However, the behavior with respect to time is very similar. While selectivity of 0.25 CaO/P25 sample does not change drastically, $NO_x$ storage selectivity values for P25 and 0.70 γ-$Al_2O_3$/P25 decreases after longer durations of operation. Moreover, for the latter ones, selectivity values after 12 hours become similar to the ones under

UV irradiation. On one hand, for all three samples, NO conversion does not change with the time. $DeNO_x$ Index values are given in Figure 49 and 50.

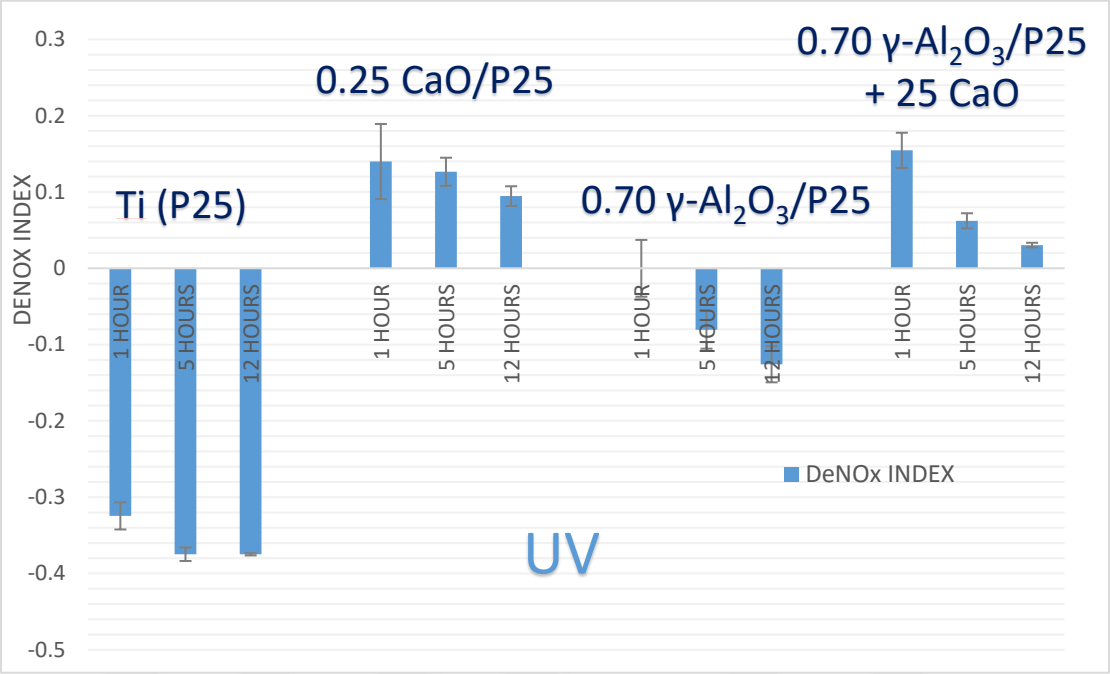


**Figure 49.** $DeNO_x$ index values of selected samples under UV irradiation in long term

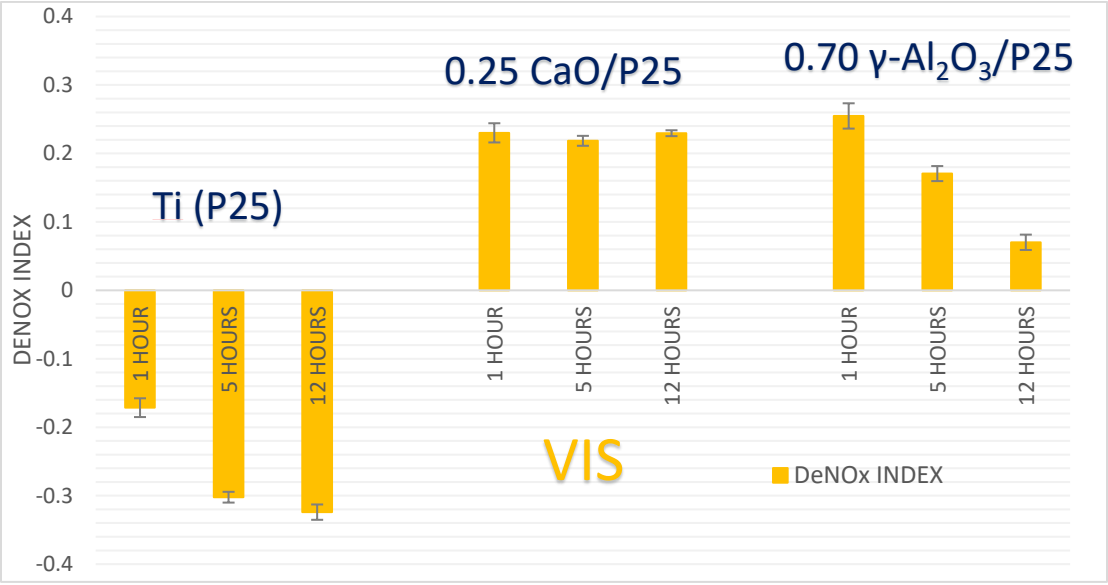


**Figure 50.** $DeNO_x$ index values of selected samples under visible irradiation in long term

Figure 47 and 48 suggest that in all cases except 0.25 CaO/P25 sample, it is seen that a noticeable decrease in $NO_x$ storage selectivity occurs after long durations of operation under UV or VIS illumination. Thus, one may question the operational lifetime of such materials under realistic applications. The answer lies within the concentration of $NO_x$. It should be noted that the inlet concentration in the current study is 1 ppm which is extremely higher as compared to the $NO_x$ concentration in the atmosphere. In atmosphere, $NO_x$ concentration is 10-20 times smaller than 1 ppm. Typical realistic atmospheric $NO_x$ concentration measurements of Ankara's selected neighborhoods for June 2017 are listed in Table 16. Note that values presented in Table 16 can change depending on the weather conditions, time of the day, season of the year and human activities. Besides, inlet concentration of $NO_x$ also plays an effective role on the photocatalytic activity of the sample. In a research study conducted by Yu *et al.*, various NO concentrations ranging from 0.1 ppm to 1.0 ppm was tested while keeping other conditions constant [77]. It was found that at lower NO concentrations higher conversion occurs. This finding was later confirmed by Husken *et al.* stating that increase in inlet concentrations result in lower degradation rates whereas lower pollutant concentrations enhance the performance [78].

**Table 16.** Typical realistic $NO_x$ concentrations in Ankara, measured and reported by the Turkish Ministry of Environment and Urbanization [79]

| **Date:** 03/06/2017 (4 pm) | **Bahçelievler** | **Cebeci** | **Demetevler** | **Dikmen** | **Kayaş** | **Keçiören** | **Sıhhıye** |
|---|---|---|---|---|---|---|---|
| **NO in µg/m$^3$ (ppm)** | 66 (0.049) | 7 (0.005) | 3 (0.002) | 6 (0.005) | 3 (0.002) | 5 (0.004) | 36 (0.027) |
| **$NO_2$ in µg/m$^3$ (ppm)** | 14 (0.007) | 32 (0.017) | 22 (0.012) | 32 (0.017) | 18 (0.010) | 20 (0.011) | 46 (0.025) |
| **Total $NO_X$ in µg/m$^3$ (ppm)** | 80 (0.056) | 39 (0.022) | 25 (0.014) | 38 (0.022) | 21 (0.012) | 25 (0.015) | 82 (0.052) |

### 3.2.6. EFFECT OF HUMIDITY ON PERFORMANCE

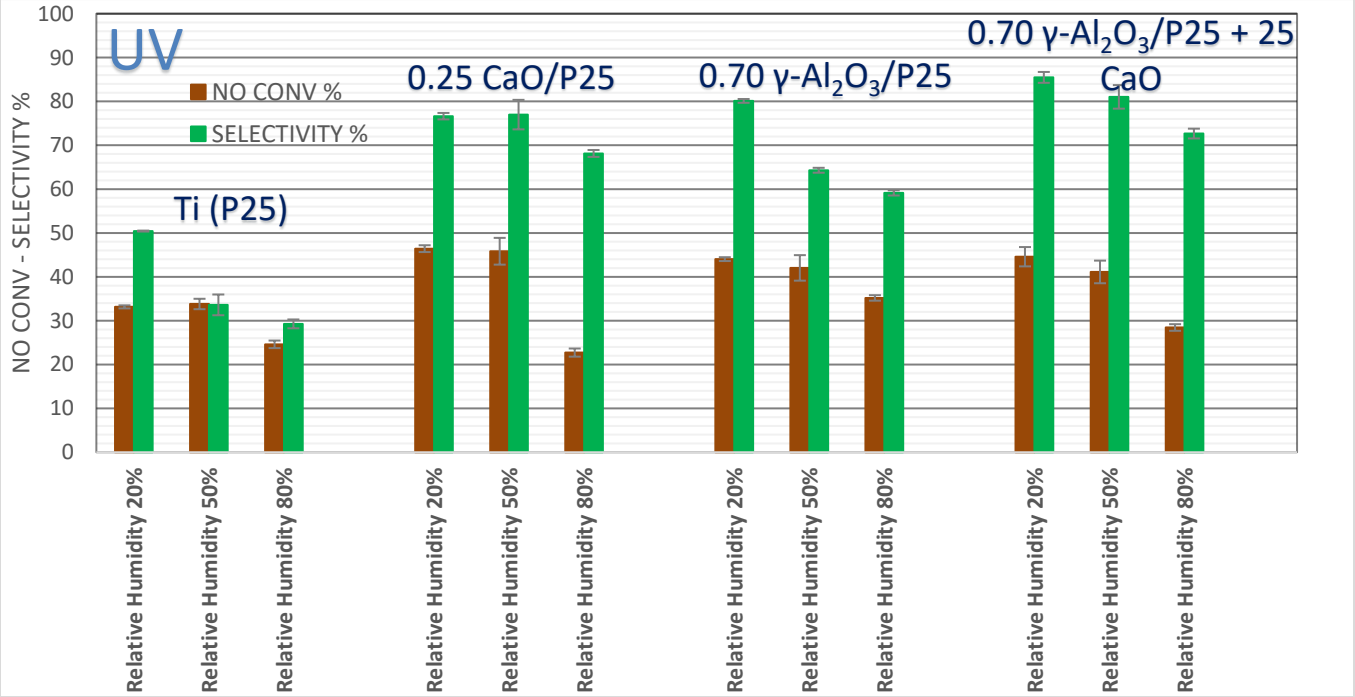


**Figure 51.** Humidity effect on photocatalytic performances under UV irradiation

The typical relative humidity (RH) level of the inlet gas mixtures in the experiments presented above was *ca.* 50% at 21-25 ˚C. To check the effect of water molecules, humidity was set to different values for four samples chosen in previous section. Tests were done under UV irradiation. The results collected are given in Figure 51.

As seen in Figure 51; between 20% and 50% RH, there is no significant difference in terms of overall NO conversion for all samples. Nevertheless; for P25 and 0.70 γ-$Al_2O_3$/P25 binary mixture, there occurs a substantial increase in $NO_x$ storage selectivity when relative humidity was decreased to 20%. This can be explained with strong interaction of water molecules and 0.70 γ-$Al_2O_3$/P25 binary oxide surfaces. Epling *et al.* examined the thermal $NO_x$ adsorption on Pt/K/γ-$Al_2O_3$ NSR catalysts in the presence of water and found out that the presence of $H_2O$ in the inlet reduces the $Al_2O_3$-based nitrates on the surface [66]. They suggested that water molecules compete with $NO_x$ for adsorption sites and saturate the surface sites by leaving fewer vacant sites for $NO_x$ to adsorb. This finding was also supported by Toops *et al.* and

Scholz *et al.* [68], [80]. When it comes to titania surface, it is reported that NO and $NO_2$ weakly adsorbs on $TiO_2$ while water can be dissociatively chemisorbed [31], [81]. Therefore, it can be argued that introducing extensive amounts of water result in a decrease in $NO_x$ storage on alumina and titania surfaces. When CaO containing binary and ternary mixtures are investigated, at 20% and 50% RH, it is seen that the selectivity results are very similar. This indicates that increasing RH from 20% to 50% has a smaller effect on the ability of the catalyst to store $NO_x$ on alkali-earth oxide adsorption sites. This idea was also supported by Epling *et al.* [66]. Figure 51 also shows that when RH was increased to 80% there is a decrease in photocatalytic oxidation of NO for all samples. This decrease can be explained with the photocatalyst poisoning with water. When water amount in the reactor is extremely high, probably titania sites for photocatalytic oxidation are oversaturated with water and not able to oxidize NO molecules. This decrease in conversion can lead to a decrease in selectivity even for CaO containing samples.

Effect of humidity on photocatalytic oxidation-storage of $NO_x$ was also addressed in various former reports. Although all of them confirmed the importance of water in the photocatalytic oxidation of water, their findings and conclusions differed sharply. The reason lies within the experimental setup and the particular operational reaction conditions used in the studies. Uner *et al.* reported that the NO conversion increases when relative humidity was increased from 0% to 93% [82]. Although their experimental setup is similar to the one used in the current study, their inlet NO concentration (5 ppm), sample preparation technique (doctor blade coating), catalyst loading (0.36 g $TiO_2$) and UV photon power density (18.8 $W/m^2$) are different from the ones used in this study. Additionally, using totally different reactor setup with 40 ppm inlet concentration, Devahasdin *et al.* stated that NO conversion increases from 0 to 50% relative humidity and becomes stable after 50% relative humidity [83]. Besides, Husken *et al.* usesd different sample preparation methods and a different gas feed rate of 3 L/min with 1 ppm NO concentration to the reactor investigated the influence of relative humidity on conversion. They found out that degradation of NO decreases with increasing relative humidity from 10% to 80% [78], [84]. Yu *et al.* having similar parameters with Husken *et al.*, investigated the humidity by feeding 0.5 ppm NO. Contrary to Husken *et al.*, it was found out that conversion increases with increasing relative humidity from 10% to 70% [77]. To sum up, conversion and storage performances of a photocatalytic material should be evaluated under comparable experimental conditions by considering the effects of following important parameters:

- Relative Humidity
- Flow Rate
- Composition of the Gas Introduced
- Experimental Setup Design
- Catalyst Loading
- Sample Preparation Technique
- Type of Light Source and Its Power
- Catalyst and Feed Gas Temperature

### 3.2.7. UV vs. VISIBLE

In previous sections, for most of the investigated samples, it was shown that that $NO_x$ storage selectivity values under VIS irradiation are typically higher than the values under UV irradiation while the NO conversion values are very similar. This interesting outcome deserves further discussion.

Firstly, the phase composition of content of P25 can be investigated. As it is known, P25 mainly consists of anatase and rutile polymorphs, and their band gaps are different. The band gaps of anatase and rutile are *ca.* 3.2 and 3.0 eV (387 and 413 nm), respectively [32]. On one hand, UV lamp (F8W/T5/BL350, Sylvania) used in experiments have emission wavelength centered around 350 nm, whereas HCI-TC 35 W/942 NDL PB lamp used for visible irradiation with UV filter have emission wavelength centered around 600 nm [34], [85]. Thus, it was questioned whether the different sites are excited under different light sources. Therefore; to understand the bandgap and irradiation relation, anatase dominant $TiO_2$ and rutile dominant $TiO_2$ were tested in the reactor setup. Under UV irradiation (Figure 52), it is seen that rutile sample obtained by the calcination has almost no activity in terms of NO conversion. Figure 52 also shows that although anatase has similar $NO_x$ storage selectivity to that of P25, its NO conversion is lower than P25. These selectivity values for anatase and P25, which are around 30-33% under UV irradiation, are consistent with previous results published by Bloh *et al.* [72]. Additionally, the VIS performances of these three samples are shown in Figure 53. Both polymorphs have almost negligible NO oxidation activities under visible irradiation. Based on the current results,

one cannot simply correlate the high $NO_x$ storage selectivity under VIS light source to crystal structures of titania and their bandgaps. As shown, while rutile has negligible NO conversion under both UV and VIS irradiation, reasonable anatase NO conversion under UV completely disappears under VIS illumination. Therefore, higher $NO_x$ storage selectivity is catalytically irrelevant for extremely low conversions. Furthermore, it should be noted that anatase and rutile used in these experiments might be different than anatase and rutile particles in P25. It is known that differences in the synthesis method of the commercial Degussa P25 can lead to differences in catalytic performance and behavior.

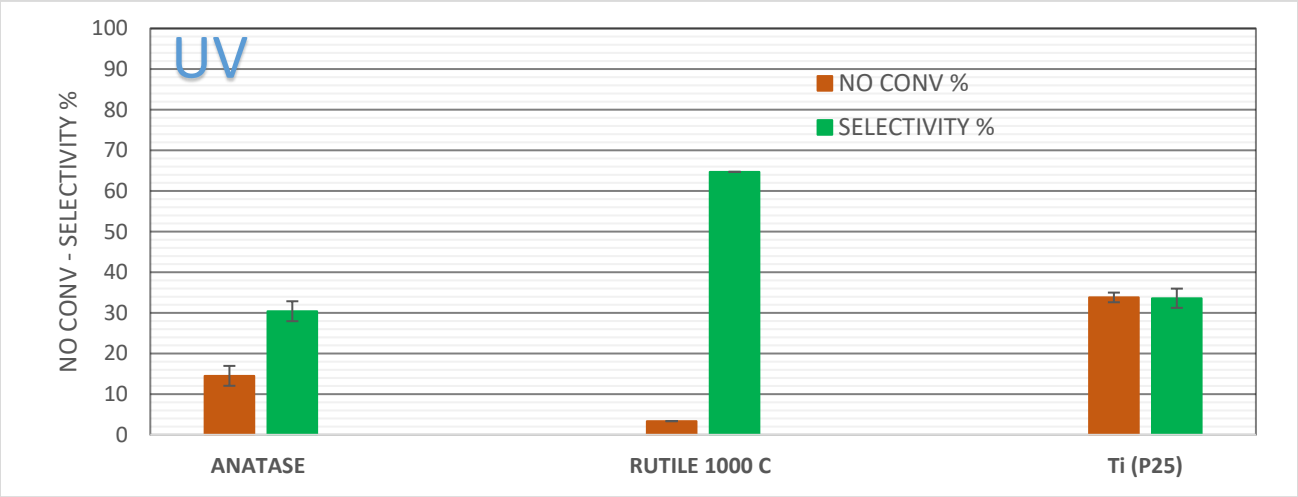


**Figure 52.** Performance plots of anatase and rutile in comparison with P25 titania (UV irradiation)

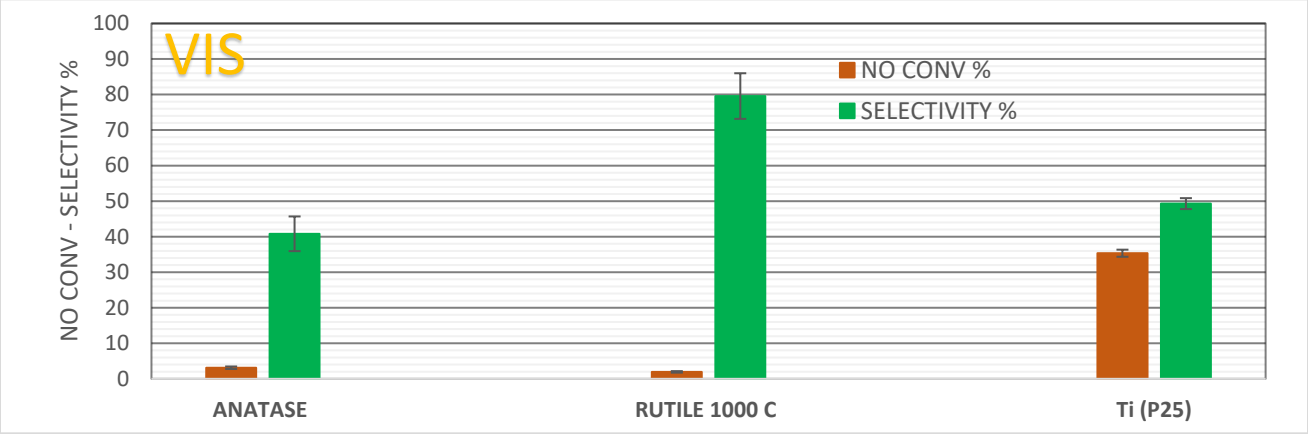


**Figure 53.** Performance plots of anatase and rutile in comparison with P25 titania (Visible irradiation)

Since the higher selectivity under VIS irradiation could not be related to the crystal phases, it was decided to check experimental conditions during the irradiation. During UV irradiation, heat released from the lamp (due to blackbody radiation and IR photons) was not high. Hence, catalyst temperature and relative humidity were not affected drastically and stayed almost invariant. Nevertheless, when 35 W VIS light source was utilized, it was noticed that heat released from the lamp increases the temperature within the reactor. With increasing temperature, relative humidity in the reactor decreases as well. Note that in both cases amount of water sent to the reactor is *identical* in terms of the number water molecules sweeping the reactor per time. On the other hand, it was measured that the temperature raised from 21-25 $^{o}$C to 36-43 $^{\circ}$C at the end of 1 h of VIS irradiation. This increase in temperature probably affects the photocatalytic processes in at least two different ways. Firstly, the heat provided to the photocatalyst may alter the number of electron-hole pairs generated as well as their (separation/recombination) mobilities on/inside the semiconductor. Eventually, an increase in the number of charge carriers may lead to an increase in the radical formation rate which may affect the surface nitrate formation favorably. Secondly, temperature rise in the reactor can influence the relative adsorption capabilities of $H_2O$ and $NO_x$ molecules. During the humidity experiments; it was found out that when water amount (*i.e.* relative humidity) was decreased, selectivity towards $NO_x$ storage increased (Figure 51). This result may indicate that $NO_x$ molecules are less strongly adsorbed onto the storage sites than water. Therefore; as temperature increases, if the adsorption energy of water decreases by a greater extent than $NO_x$, higher $NO_x$ storage selectivity can be observed under VIS light illumination. To confirm these proposed arguments, experiments under visible irradiation with varying temperatures were designed, but due to the instrumental problems related to the $NO_x$ analyzer these experiments could not be conducted. However, it was found out that Obee *et al*. and Fu *et al*. investigated effects of humidity and temperature on photocatalytic oxidation of ethylene [86], [87]. In these studies, the results revealed that water has poisoning effect on ethylene adsorption and with increasing temperature enhancement on photocatalytic oxidation can be observed. Both studies attributed this observation to the higher adsorption affinity of water molecules than ethylene.

### 3.3.SURFACE FUNCTIONAL GROUP ANALYSIS VIA FTIR

To understand the storage process on the surface, four samples (*i.e.* P25, 0.25 CaO/P25, 0.70 γ-$Al_2O_3$/P25, 0.70 γ-$Al_2O_3$/P25 + 25 CaO) were tested in the photocatalytic reactor under UV light for *ca.* 18 h and then examined *via* FTIR. During FTIR measurements, fresh samples which were not exposed to any NO*x* were used as the background.

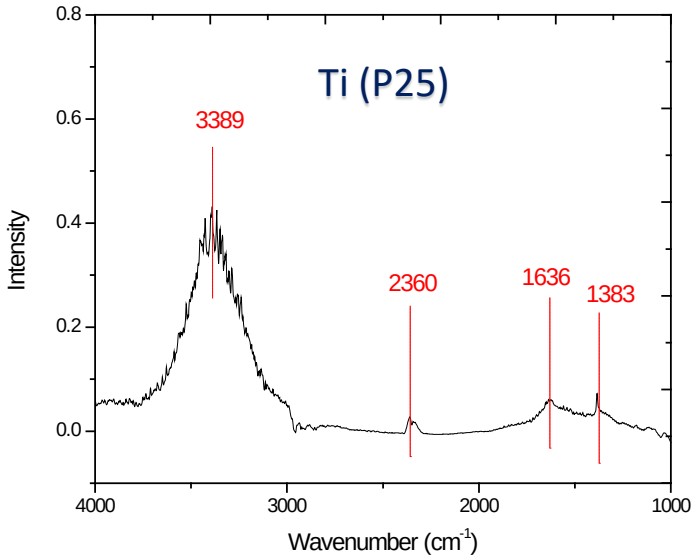


**Figure 54.** FTIR spectrum of P25 after photocatalytic test under UV irradiation

As seen from Figure 54, IR spectrum of P25 exhibits a strong absorption band at 1636 $cm^{-1}$, which is attributed to molecularly absorbed water. Furthermore, the broad band centered around 3389 $cm^{-1}$ can be identified to the hydroxyl groups revealing hydrogen bonding. The peak at 1383 $cm^{-1}$ is also identified as nitrate ions accumulated on the titania surface during photocatalytic oxidation of NO. Finally, the peak at 2360 $cm^{-1}$ is related to ambient $CO_2$(g). In general, this spectrum is consistent with previous results in the literature [88], [89].

FTIR spectrum of 0.70 γ-$Al_2O_3$/P25 sample after the photocatalytic tests (Figure 55) has also features resembling that of P25. IR absorption signal at 1384 $cm^{-1}$ can be identified as the nitrate ions on the sample surface. The small peak at 1510 $cm^{-1}$ might be attributed to $v_3$ vibration mode of bridging or monodentate nitrate groups, but low intensity and absence of other bands make

this interpretation debatable. Moreover, the bands related to water adsorption are also visible *ca.* at 1637 $cm^{-1}$ (due to the bending mode of adsorbed molecular $H_2O$) whereas the broad envelope centered around 3454 $cm^{-1}$ can be related to -OH stretchings on alumina and titania surfaces. In the literature; it is known that because of water adsorption on γ-$Al_2O_3$ a broad band occurs at 3444 $cm^{-1}$ with shoulders at 3188 and 3583 $cm^{-1}$ [90]. The shoulder at 2960 $cm^{-1}$ can be attributed to organic compound with C-H bond at 2800-3100 $cm^{-1}$ or overtone modes of surface nitrate species [88].

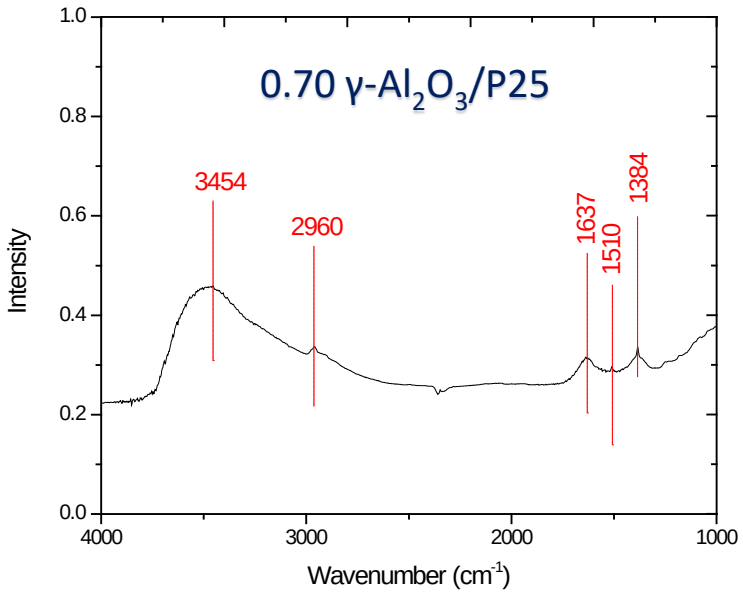


**Figure 55.** FTIR spectrum of 0.70 γ-$Al_2O_3$/P25 after photocatalytic test under UV irradiation

When results for CaO containing binary and ternary mixtures (Figure 56 and 57) were investigated it was seen that there is no peak related to $NO_x$ storage. This happened because of $Ca(OH)_2$ formed during the photocatalytic test. As CaO quickly reacts with water in the air, after 18 h in photocatalytic reactor most of the CaO in the mixture probably turned into $Ca(OH)_2$. The strong O-H stretching band at 3640 $cm^{-1}$ supports the calcium hydroxide formation [70]. Furthermore, in both cases a split absorption band in the range 1400–1500 $cm^{-1}$ was observed. This band is due to the chemisorption of $CO_2$ on calcium hydroxide during FTIR measurement in the form of monodentate carbonate. The splitting of the band (1479-1423 in Figure 56 and 1479-

1413 in Figure 57) shows the distortion of carbonate groups [70]. Due to the domination of these strong bands, nitrate related peaks are unobservable. Moreover, the bands in the range of 3000-3600 $cm^{-1}$ can be attributed to -OH groups on alumina and titania surfaces.

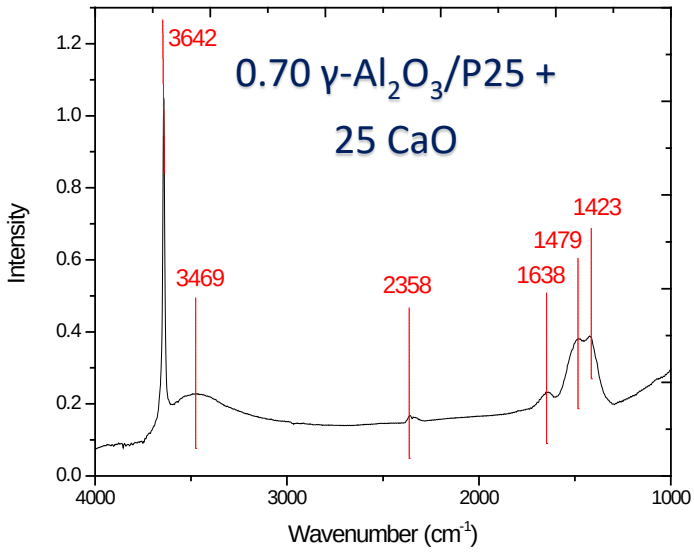


**Figure 56.** FTIR spectrum of 0.70 γ-$Al_2O_3$/P25 + 25 CaO after photocatalytic test under UV irradiation

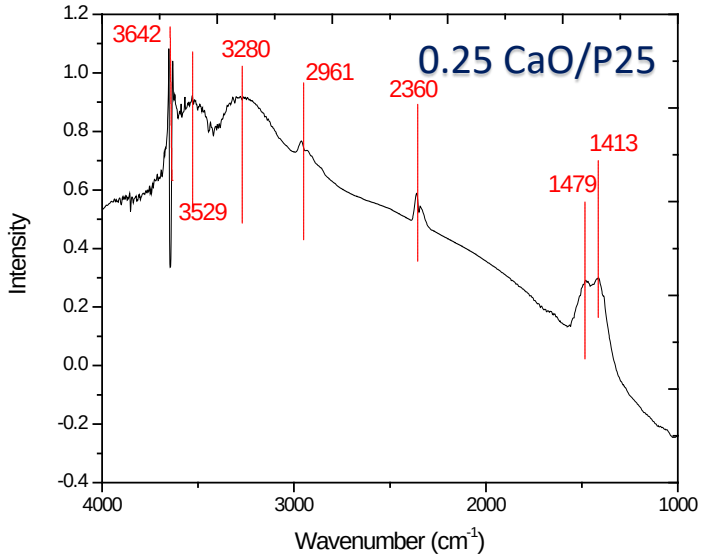


**Figure 57.** FTIR spectrum of 0.25 CaO/P25 after photocatalytic test under UV irradiation

To sum up, IR spectra obtained after post-photocatalytic tests were helpful only up to certain extent. In the absence of calcium oxide, nitrate formation on surface was detected; however, it was not possible to extract detailed information about the reaction mechanism using the ex-situ FTIR analysis. As mentioned; when CaO was introduced, none of nitrate (nor nitrite) vibration modes were observed in FTIR. Therefore, *in-situ* or *operando* FTIR measurements need to be carried out in order to understand the photocatalytic $NO_x$ oxidation-storage mechanisms on the relevant sample surfaces.

# Chapter 4

# Future Work

To gain a deeper understanding of photocatalytic $NO_x$ oxidation-storage, the following future experiments can be carried out:

- To understand the temperature effect on oxidation-storage performances, photocatalytic experiments with various temperatures must be conducted. These experiments can give better understanding on the difference between visible and UV experiments presented in this thesis.
- P25 can be separated into its crystal phases, and each phase can be tested in the photocatalytic reactor independently. This can also give more information about relation between bandgap and light irradiation.
- The samples used in photocatalytic tests should be regenerated with water or heat treatment, then re-tested. This provides information about the reusability of samples.
- To learn more about photocatalytic oxidation and storage mechanisms, *in-situ* or *operando* FTIR experiments with various water and $NO_x$ concentrations should be designed.
- Due to the malfunctioning of chemiluminescence $NO_x$ analyzer, long term performance of 0.70 $\gamma$-$Al_2O_3$/P25 + 25 CaO under VIS irradiation could not be studied. Thus, checking its performance during long run experiments would be informative.
- To decrease the bandgap of the photocatalyst and electron-hole recombination rate, new material synthesis protocols can be explored. Formation of heterojunctions or introduction of dopants into the structure could be promising.
- To optimize $NO_x$ and $H_2O$ adsorption affinities, surface properties (*i.e.* surface acidity) can be adjusted.

- Commercially available cements (or other construction materials) can be mixed with photocatalytically active other affordable semiconductors to analyze their influence on performance.
- (P2) 1.0 Ti/Al binary oxides synthesized via sol-gel co-precipitation can be prepared and tested using the currently demonstrated performance analysis methods.

# Chapter 5

# Conclusion

In this study, application of cost-effective physical mixtures for the effective photocatalytic oxidation and storage of gas phase $NO_x$ species was proposed and tested. In this regard, a new set of performance analysis parameters (%NO Conversion, %Selectivity, De$NO_x$ INDEX) were developed and adapted due to the lack of information provided by conventional photonic efficiencies. Then; previously tested and optimized, (P2) 0.5 Ti/Al binary oxides were re-synthesized and re-tested under UV irradiation based on new performance evaluation methods. Photocatalytic performances of (P2) 0.5 Ti/Al binary oxides were not satisfactory to be used as stand-alone catalytic systems. Inspired from $NO_x$ Storage Reduction systems (NSR) used in automotive emission control systems, (P2) 0.5 Ti/Al binary oxides were mixed with an abundant alkaline earth oxide, CaO, to increase $NO_x$ storage. It was observed that although selectivity towards $NO_x$ storage increased with CaO addition, total NO conversion of samples decreased. It was also found out that addition of CaO into commercially available Degussa P25 resulted in superior performances compared to (P2) 0.5 Ti/Al-900 $^oC$ + CaO samples.

CaO/P25 binary physical mixtures with four different compositions (1wt%, 5wt%, 10wt%, 25wt% CaO) were tested under both UV and VIS irradiation. As CaO amount increased, $NO_x$ storage selectivity increased up to a certain limit for both cases. However; while NO conversion values were similar under both UV and VIS irradiation, $NO_x$ storage selectivity values under VIS light were significantly higher. Then, $\gamma$-$Al_2O_3$/P25 were prepared with 10 wt%, 30 wt%, 50 wt%, 70 wt%, 90 wt% $\gamma$-$Al_2O_3$. These samples were also tested photocatalytically under UV and VIS illumination. Similarly, $NO_x$ storage selectivity performances in VIS experiments were higher compared to UV experiments but were not as good as CaO/P25 physical mixtures. 70 wt% $\gamma$-$Al_2O_3$/P25 physical mixture was chosen as the best sample based on

composition-performance analysis. Then, this alumina and titania containing 70 wt% γ-$Al_2O_3$/P25 binary mixture were mixed with 1 wt%, 5 wt%, 10 wt%, 25 wt% CaO. After photocatalytic tests, these ternary physical mixtures were found to perform comparable to the 0.25 CaO/P25 while containing a lower $TiO_2$ content and thus revealing a lower catalyst material cost for mass production.

Long term performances of chosen samples (*i.e.* P25, 0.25 CaO/P25, 0.70 γ-$Al_2O_3$/P25 and 0.70 γ-$Al_2O_3$/P25 + 25 CaO) were investigated. Except 0.25 CaO/P25 sample, decrease in selectivity was observed in all catalysts upon extended duration of operation. It was realized that NO conversion stays constant even after 12 h for all binary mixtures.

The effect of humidity on the photocatalytic oxidation-storage was also studied on P25, 0.25 CaO/P25, 0.70 γ-$Al_2O_3$/P25 and 0.70 γ-$Al_2O_3$/P25 + 25 CaO samples. It was revealed that although water is important to initiate photocatalytic reactions by possibly forming hydroxyl radicals, it has also a poisoning effect because of its competitive nature of adsorption.

The differences in terms of selectivity in UV and VIS experiments were discussed. Although it requires further work to understand, differences might be explained with the temperature rise due to heat released from VIS light sources. This temperature rise may affect the adsorption affinities of $H_2O$ and $NO_x$, which in turn, might enhance the $NO_x$ abatement performance. Besides, *via ex-situ* FTIR measurements, $NO_x$ storage on sample surfaces was studied. For CaO containing samples, no nitrate (or nitrite) related bands were observed due to the bands resulting from calcium carbonate; but nitrate bands were detected on P25 and 0.70 γ-$Al_2O_3$/P25 samples.

# Bibliography


[1] World Health Organization, “Ambient (outdoor) air quality and health,” *WHO*, 2016. [Online]. Available: http://www.who.int/mediacentre/factsheets/fs313/en/. [Accessed: 07-Jun-2016].

[2] E. Oner and B. Kaynak, “Evaluation of NOx emissions for Turkey using satellite and ground-based observations,” *Atmos. Pollut. Res.*, vol. 7, no. 3, pp. 419–430, 2016.

[3] Environmental Protection Agency (EPA), “Nitrogen Oxides ( NOx ), Why and How They Are Controlled,” *Epa-456/F-99-006R*, no. November, p. 48, 1999.

[4] “Sector share of nitrogen oxides emissions — European Environment Agency.” [Online]. Available: http://www.eea.europa.eu/data-and-maps/daviz/sector-share-of-nitrogen-oxides-emissions#tab-chart_1. [Accessed: 13-Apr-2017].

[5] OECD, *Environment at a Glance 2015*. Paris: OECD Publishing, 2015.

[6] R. C. Flagan and J. H. Seinfeld, “Pollutant formation and control in combustion,” *Fundam. air Pollut. Eng.*, p. 168, 1988.

[7] J. Lasek, Y. H. Yu, and J. C. S. Wu, “Removal of NOx by photocatalytic processes,” *J. Photochem. Photobiol. C Photochem. Rev.*, vol. 14, no. 1, pp. 29–52, 2013.

[8] B. V Novozhilov, “Zel’dovich’s accomplishments in combustion science,” *Prog. Astronaut. Aeronaut.*, pp. 3–18, 1997.

[9] G. A. Lavoie, J. B. Heywood, and J. C. Keck, “Experimental and Theoretical Study of Nitric Oxide Formation in Internal Combustion Engines,” *Combust. Sci. Technol.*, vol. 1, no. 4, pp. 313–326, Feb. 1970.

[10] P. C. Malte and D. T. Pratt, “The Role of Energy-Releasing Kinetics in NOx Formation: Fuel-Lean, Jet-Stirred CO-Air Combustion,” *Combust. Sci. Technol.*, vol. 9, no. 5–6, pp. 221–231, 1974.

[11] C. P. Fenimore, “Formation of nitric oxide in premixed hydrocarbon flames,” *Symp.*

*Combust.*, vol. 13, no. 1, pp. 373–380, 1971.

[12] J. W. Bozzelli and A. M. Dean, “O + NNH: A possible new route for NOX formation in flames,” *Int. J. Chem. Kinet.*, 1995.

[13] J. Tomeczek and B. Gradoń, “The role of N2O and NNH in the formation of NO via HCN in hydrocarbon flames,” *Combust. Flame*, vol. 133, no. 3, pp. 311–322, 2003.

[14] J. A. Sutton and J. W. Fleming, “Towards accurate kinetic modeling of prompt NO formation in hydrocarbon flames via the NCN pathway,” *Combust. Flame*, vol. 154, no. 3, pp. 630–636, 2008.

[15] J. A. Goodeve, C. F. ; Kitchener, “Photosensitisation by titanium dioxide,” *Trans. Faraday Soc.*, vol. 34, pp. 570–579, 1938.

[16] K. Hashimoto, H. Irie, and A. Fujishima, “TiO2 Photocatalysis: A Historical Overview and Future Prospects,” *AAPPS Bull.*, vol. 17, no. 6, pp. 12–28, 2007.

[17] A. Fujishima and K. Honda, “TiO2 photoelectrochemistry and photocatalysis,” *Nature*, vol. 238, no. 5358, pp. 37–38, 1972.

[18] H. Xu, S. Ouyang, L. Liu, P. Reunchan, N. Umezawa, and J. Ye, “Recent advances in TiO 2 -based photocatalysis,” *J. Mater. Chem. A*, vol. 2, no. 32, p. 12642, 2014.

[19] X. Chen, X. Chen, C. Burda, and C. Burda, “The Electronic Origin of the Visible-Light Absorption Properties of C-, N- and S-Doped TiO 2 Nanomaterials,” *J. Am. Chem. Soc.*, pp. 5018–5019, 2008.

[20] R. Long and N. J. English, “Band gap engineering of double-cation-impurity-doped anatase-titania for visible-light photocatalysts: a hybrid density functional theory approach.,” *Phys. Chem. Chem. Phys.*, vol. 13, no. 30, pp. 13698–13703, 2011.

[21] K. Nagaveni, M. S. Hegde, and G. Madras, “Structure and Photocatalytic Activity of Ti1-xMxO2±δ (M = W, V, Ce, Zr, Fe, and Cu) Synthesized by Solution Combustion Method,” *J. Phys. Chem. B*, vol. 108, no. 52. pp. 20204–20212, 2004.

[22] L. G. Devi and R. Kavitha, “A review on non metal ion doped titania for the photocatalytic degradation of organic pollutants under UV/solar light: Role of

photogenerated charge carrier dynamics in enhancing the activity," *Appl. Catal. B Environ.*, vol. 140–141, pp. 559–587, 2013.

[23] S. J. Tang, S. J. A. Moniz, S. A. Shevlin, D. J. Martin, Z.-X. Guo, and J. Tang, "Visible-light driven heterojunction photocatalysts for water splitting – a critical review," *Energy Environ. Sci.*, vol. 8, pp. 731–759, 2015.

[24] J. Low, J. Yu, M. Jaroniec, S. Wageh, and A. A. Al-Ghamdi, "Heterojunction Photocatalysts," *Adv. Mater.*, p. 1601694, 2017.

[25] M. Zhou, J. Yu, S. Liu, P. Zhai, and L. Jiang, "Effects of calcination temperatures on photocatalytic activity of SnO2/TiO2 composite films prepared by an EPD method," *J. Hazard. Mater.*, vol. 154, no. 1–3, pp. 1141–1148, 2008.

[26] J. Yu, W. Wang, and B. Cheng, "Synthesis and enhanced photocatalytic activity of a hierarchical porous flowerlike p-n junction NiO/TiO2 photocatalyst," *Chem. - An Asian J.*, vol. 5, no. 12, pp. 2499–2506, 2010.

[27] J. Yu, J. Low, W. Xiao, P. Zhou, and M. Jaroniec, "Enhanced Photocatalytic $CO_2$ - Reduction Activity of Anatase $TiO_2$ by Coexposed {001} and {101} Facets," *J. Am. Chem. Soc.*, vol. 136, no. 25, pp. 8839–8842, 2014.

[28] J. Yu, S. Wang, J. Low, and W. Xiao, "Enhanced photocatalytic performance of direct Z-scheme g-C3N4-TiO2 photocatalysts for the decomposition of formaldehyde in air," *Phys Chem Chem Phys*, vol. 15, no. 39, pp. 16883–16890, 2013.

[29] Q. Xiang, J. Yu, and M. Jaroniec, "Enhanced photocatalytic H(2)-production activity of graphene-modified titania nanosheets.," *Nanoscale*, vol. 3, no. 9, pp. 3670–3678, 2011.

[30] G. Liu, J. C. Yu, G. Q. M. Lu, and H.-M. Cheng, "Crystal facet engineering of semiconductor photocatalysts: motivations, advances and unique properties.," *Chem. Commun.*, vol. 47, no. 24, pp. 6763–83, 2011.

[31] A. L. Linsebigler, A. L. Linsebigler, J. T. Yates Jr, G. Lu, G. Lu, and J. T. Yates, "Photocatalysis on TiO2 Surfaces: Principles, Mechanisms, and Selected Results," *Chem. Rev.*, vol. 95, no. 3, pp. 735–758, 1995.

[32] D. A. H. Hanaor and C. C. Sorrell, “Review of the anatase to rutile phase transformation,” *J. Mater. Sci.*, vol. 46, no. 4, pp. 855–874, 2011.

[33] O. Carp, C. L. Huisman, and A. Reller, “Photoinduced reactivity of titanium dioxide,” *Prog. Solid State Chem.*, vol. 32, no. 1–2, pp. 33–177, 2004.

[34] A. M. Soylu, “Photocatalytic NOx Oxidation and Storage Under Ambient Conditions for Air Purification,” M.S. Thesis, Dept. Chemistry, Bilkent University, Turkey, 2012.

[35] A. Fujishima, X. Zhang, and D. A. Tryk, “TiO2 photocatalysis and related surface phenomena,” *Surf. Sci. Rep.*, vol. 63, no. 12, pp. 515–582, 2008.

[36] H. G. Yang *et al.*, “Anatase TiO2 single crystals with a large percentage of reactive facets,” *Nature*, vol. 453, no. 7195, pp. 638–641, 2008.

[37] C. Sun, L.-M. Liu, A. Selloni, G. Q. (Max) Lu, and S. C. Smith, “Titania-water interactions: a review of theoretical studies,” *J. Mater. Chem.*, vol. 20, no. 46, p. 10319, 2010.

[38] J. M. Coronado, F. Fresno, M. D. Hernández-Alonso, and R. Portela, *Design of Advanced Photocatalytic Materials for Energy and Environmental Applications*, 1st ed. Springer-Verlag London, 2013.

[39] R. Asahi, Y. Taga, W. Mannstadt, and A. Freeman, “Electronic and optical properties of anatase TiO2,” *Phys. Rev. B*, vol. 61, no. 11, pp. 7459–7465, 2000.

[40] H. Wang and J. P. Lewis, “Second-generation photocatalytic materials: anion-doped TiO 2,” *J. Phys. Condens. Matter*, vol. 18, no. 2, pp. 421–434, 2006.

[41] B. Ohtani, O. O. Prieto-Mahaney, D. Li, and R. Abe, “What is Degussa (Evonic) P25? Crystalline composition analysis, reconstruction from isolated pure particles and photocatalytic activity test,” *J. Photochem. Photobiol. A Chem.*, vol. 216, no. 2–3, pp. 179–182, 2010.

[42] “Titanium(IV) oxide nanopowder, 21 nm primary particle size (TEM), ≥99.5% trace metals basis | Sigma-Aldrich.” [Online]. Available: http://www.sigmaaldrich.com/catalog/product/aldrich/718467?lang=en&region=TR.

[Accessed: 18-May-2017].

[43] Z. Rui, S. Wu, C. Peng, and H. Ji, “Comparison of TiO2 Degussa P25 with anatase and rutile crystalline phases for methane combustion,” *Chem. Eng. J.*, vol. 243, no. May 2014, pp. 254–264, 2014.

[44] B. Viswanathan and K. J. A. Raj, “Effect of surface area, pore volume and particle size of P25 titania on the phase transformation of anatase to rutile,” *Indian J. Chem. - Sect. A Inorganic, Phys. Theor. Anal. Chem.*, vol. 48, no. 10, pp. 1378–1382, 2009.

[45] G. Wang, L. Xu, J. Zhang, T. Yin, and D. Han, “Enhanced photocatalytic activity of TiO 2 powders (P25) via calcination treatment,” *Int. J. Photoenergy*, vol. 2012, 2012.

[46] F. Normann, K. Andersson, B. Leckner, and F. Johnsson, “Emission control of nitrogen oxides in the oxy-fuel process,” *Prog. Energy Combust. Sci.*, vol. 35, no. 5, pp. 385–397, 2009.

[47] N. Bowering, G. S. Walker, and P. G. Harrison, “Photocatalytic decomposition and reduction reactions of nitric oxide over Degussa P25,” *Appl. Catal. B Environ.*, vol. 62, no. 3–4, pp. 208–216, 2006.

[48] H. Courbon and P. PICHAT, “Room-temperature Interaction of N180 with Ultraviolet-illuminated Titanium Dioxide,” pp. 3175–3185, 1984.

[49] M. Anpo, T. H. Kim, and M. Matsuoka, “The design of Ti-, V-, Cr-oxide single-site catalysts within zeolite frameworks and their photocatalytic reactivity for the decomposition of undesirable molecules-The role of their excited states and reaction mechanisms,” *Catal. Today*, vol. 142, no. 3–4, pp. 114–124, 2009.

[50] M. Anpo and M. Takeuchi, “The design and development of highly reactive titanium oxide photocatalysts operating under visible light irradiation,” *J. Catal.*, vol. 216, no. 1–2, pp. 505–516, 2003.

[51] I.-H. Su and J. C. S. Wu, “Photo selective catalytic reduction of nitric oxide with propane at room temperature,” *Catal. Commun.*, vol. 10, no. 11, pp. 1534–1537, 2009.

[52] M. Matsuoka, S. Higashimoto, H. Yamashita, and M. Anpo, “In-situ investigations of the

photocatalytic reaction of no with propane on the vanadium silicalite-1 catalyst," *Res. Chem. Intermed.*, vol. 26, no. 1, pp. 85–92, 2000.

[53] K. Teramura, T. Tanaka, S. Yamazoe, K. Arakaki, and T. Funabiki, "Kinetic study of photo-SCR with NH3 over TiO2," *Appl. Catal. B Environ.*, vol. 53, no. 1, pp. 29–36, 2004.

[54] J. C. Colmenares and R. Luque, "Heterogeneous photocatalytic nanomaterials: prospects and challenges in selective transformations of biomass-derived compounds.," *Chem. Soc. Rev.*, vol. 43, no. 3, pp. 765–78, 2014.

[55] C. T. Dinh, S. Hoogland, and E. H. Sargent, "Spontaneous and Light-Driven Conversion of NOx on Oxide-Modified TiO2 Surfaces," *Ind. Eng. Chem. Res.*, vol. 54, no. 51, pp. 12750–12756, 2015.

[56] J. S. Dalton, P. A. Janes, N. G. Jones, J. A. Nicholson, K. R. Hallam, and G. C. Allen, "Photocatalytic oxidation of NOx gases using TiO2: A surface spectroscopic approach," *Environ. Pollut.*, vol. 120, no. 2, pp. 415–422, 2002.

[57] J. C. S. Wu and Y. T. Cheng, "In situ FTIR study of photocatalytic NO reaction on photocatalysts under UV irradiation," *J. Catal.*, vol. 237, no. 2, pp. 393–404, 2006.

[58] A. M. Soylu *et al.*, "TiO2-Al2O3 binary mixed oxide surfaces for photocatalytic NOx abatement," *Appl. Surf. Sci.*, vol. 318, no. x, pp. 142–149, 2014.

[59] M. Polat, A. M. Soylu, D. A. Erdogan, H. Erguven, E. I. Vovk, and E. Ozensoy, "Influence of the sol-gel preparation method on the photocatalytic NO oxidation performance of TiO2/Al2O3 binary oxides," *Catal. Today*, vol. 241, no. PA, pp. 25–32, 2015.

[60] B. Ohtani, "Hidden but Possibly Fatal Misconceptions in Photocatalysis Studies: A Short Critical Review," *Catalysts*, vol. 6, no. 12, p. 192, 2016.

[61] P. C. Hewlett, *Lea's Chemistry of Cement and Concrete*, 4th editio. Oxford: Butterworth-Heinemann, 2003.

[62] M. M. Oymak, "Photocatalytic Activity in Nano Sized Titanium Dioxide Structures,"

Ph.D. Thesis, Dept. Chem. Eng., Middle East Technical University, Turkey, 2012.

[63] M. Trueba and S. P. Trasatti, "γ-alumina as a support for catalysts: A review of fundamental aspects," *Eur. J. Inorg. Chem.*, no. 17, pp. 3393–3403, 2005.

[64] J. Szanyi, J. H. Kwak, R. J. Chimentao, and C. H. F. Peden, "Effect of H2O on the adsorption of NO2 on γ-Al2O3: An in situ FTIR/MS study," *Journal of Physical Chemistry C*, vol. 111, no. 6. pp. 2661–2669, 2007.

[65] L. Olsson, P. Jozsa, M. Nilsson, and E. Jobson, "Fundamental studies of NOx storage at low temperatures," *Top. Catal.*, vol. 42–43, no. 1–4, pp. 95–98, 2007.

[66] W. S. Epling, J. E. Parks, G. C. Campbell, A. Yezerets, N. W. Currier, and L. E. Campbell, "Further evidence of multiple NO x sorption sites on NO x storage/reduction catalysts," *Catal. Today*, vol. 96, no. 1–2, pp. 21–30, 2004.

[67] C. Verrier, J. H. Kwak, D. H. Kim, C. H. F. Peden, and J. Szanyi, "NOx uptake on alkaline earth oxides (BaO, MgO, CaO and SrO) supported on γ-Al2O3," *Catalysis Today*, vol. 136, no. 1–2. pp. 121–127, 2008.

[68] T. J. Toops, D. B. Smith, W. S. Epling, J. E. Parks, and W. P. Partridge, "Quantified NOx adsorption on Pt/K/gamma-Al2O 3 and the effects of CO2 and H2O," *Appl. Catal. B Environ.*, vol. 58, no. 3–4, pp. 255–264, 2005.

[69] S. Sasol, "PURALOX®/CATALOX® High purity activated aluminas." [Online]. Available: http://www.sasolnorthamerica.com/Images/Interior/products/sasol-inorganics_puralox_catalox (2).pdf. [Accessed: 02-Jun-2017].

[70] A. M. Kalinkin, E. V Kalinkina, O. A. Zalkind, and T. I. Makarova, "Chemical Interaction of Calcium Oxide and Calcium Hydroxide with CO2 during Mechanical Activation," *Inorg. Mater.*, vol. 41, no. 10, pp. 1073–1079, 2005.

[71] "PermSelect® Silicone Membrane Modules | PermSelect-MedArray." [Online]. Available: https://www.permselect.com/products. [Accessed: 26-May-2017].

[72] J. Z. Bloh, A. Folli, and D. E. Macphee, "Photocatalytic NOx abatement: Why the selectivity matters," *RSC Adv.*, vol. 4, no. 86, pp. 45726–45734, 2014.

[73] R. A. Spurr and H. Myers, “Quantitative Analysis of Anatase-Rutile Mixtures with an X-Ray Diffractometer,” *Anal. Chem.*, vol. 29, no. 5, pp. 760–762, 1957.

[74] Z. Wang and X. Deng, “Al2O3 composite agent effects on phase transformation of nanometer TiO2 powder,” *Mater. Sci. Eng. B Solid-State Mater. Adv. Technol.*, vol. 140, no. 1–2, pp. 109–113, 2007.

[75] E. C. Corbos, X. Courtois, N. Bion, P. Marecot, and D. Duprez, “Impact of the support oxide and Ba loading on the sulfur resistance and regeneration of Pt/Ba/support catalysts,” *Appl. Catal. B Environ.*, vol. 80, no. 1–2, pp. 62–71, 2008.

[76] N. W. Cant and M. J. Patterson, “The storage of nitrogen oxides on alumina-supported barium oxide,” *Catal. Today*, vol. 73, no. 3–4, pp. 271–278, 2002.

[77] Q. L. Yu and H. J. H. Brouwers, “Indoor air purification using heterogeneous photocatalytic oxidation. Part I: Experimental study,” *Appl. Catal. B Environ.*, vol. 92, no. 3–4, pp. 454–461, 2009.

[78] G. Hüsken, M. Hunger, and H. J. H. Brouwers, “Experimental study of photocatalytic concrete products for air purification,” *Build. Environ.*, vol. 44, no. 12, pp. 2463–2474, 2009.

[79] TC Cevre ve Sehircilik Bakanligi, “Hava Kalitesi Izleme Istasyonlari Web Sitesi.” [Online]. Available: http://www.havaizleme.gov.tr/Default.ltr.aspx. [Accessed: 03-Jun-2017].

[80] C. M. L. Scholz, V. R. Gangwal, M. H. J. M. de Croon, and J. C. Schouten, “Influence of CO2 and H2O on NOx storage and reduction on a Pt-Ba/??-Al2O3 catalyst,” *Applied Catalysis B: Environmental*, vol. 71, no. 3–4. pp. 143–150, 2007.

[81] D. Sorescu, C. Rusu, and J. Y. Jr, “Adsorption of NO on the TiO2 (110) Surface: An Experimental and Theoretical Study,” *The Journal of Physical …*, vol. 2, no. 110. pp. 4408–4417, 2000.

[82] D. Uner, I. Bayar, and T. Tabari, “The influence of relative humidity on photocatalytic oxidation of nitric oxide (NO) over TiO2,” *Appl. Surf. Sci.*, vol. 354, pp. 260–266, 2015.

[83] S. Devahasdin, C. Fan, K. Li, and D. H. Chen, “TiO2 photocatalytic oxidation of nitric oxide: Transient behavior and reaction kinetics,” *J. Photochem. Photobiol. A Chem.*, vol. 156, no. 1–3, pp. 161–170, 2003.

[84] M. Hunger, G. Hüsken, and H. J. H. Brouwers, “Photocatalytic degradation of air pollutants - From modeling to large scale application,” *Cem. Concr. Res.*, vol. 40, no. 2, pp. 313–320, 2010.

[85] P. Hci-t, “HCI-T 35 W / 942 NDL PB POWERBALL HCI-T | Metal halide lamps with ceramic technology for enclosed luminaires,” pp. 1–7.

[86] T. N. Obee and S. O. Hay, “Effects of moisture and temperature on the photo- oxidation of ethylene on titania,” *Environ. Sci. Technol.*, vol. 31, no. 7, pp. 2034–2038, 1997.

[87] X. Fu, L. A. Clark, W. A. Zeltner, and M. A. Anderson, “Effects of reaction temperature and water vapor content on the heterogeneous photocatalytic oxidation of ethylene,” *J. Photochem. Photobiol. A Chem.*, vol. 97, no. 3, pp. 181–186, 1996.

[88] K. Hashimoto, K. Wasada, N. Toukai, H. Kominami, and Y. Kera, “Photocatalytic oxidation of nitrogen monoxide over titanium(IV) oxide nanocrystals large size areas,” *J. Photochem. Photobiol. A Chem.*, vol. 136, no. 1–2, pp. 103–109, 2000.

[89] H. Wang, Z. Wu, W. Zhao, and B. Guan, “Photocatalytic oxidation of nitrogen oxides using TiO2 loading on woven glass fabric,” *Chemosphere*, vol. 66, no. 1, pp. 185–190, 2007.

[90] H. A. Al-Abadleh and V. H. Grassian, “FT-IR study of water adsorption on aluminum oxide surfaces,” *Langmuir*, vol. 19, no. 2, pp. 341–347, 2003.